SPECTROSCOPIC AND COMPUTATIONAL INVESTIGATIONS OF MOLECULAR INTERACTIONS IN GAS-EXPANDED LIQUIDS

A Thesis
Presented to
The Academic Faculty

by

John Linton Gohres III

In Partial Fulfillment
of the Requirements for the Degree
Doctor of Philosophy in the
School of Chemical and Biomolecular Engineering

Georgia Institute of Technology
August 2008

SPECTROSCOPIC AND COMPUTATIONAL INVESTIGATIONS OF MOLECULAR INTERACTIONS IN GAS-EXPANDED LIQUIDS

Approved by:

Dr. Charles Eckert, Advisor
School of Chemical and Biomolecular Engineering
Georgia Institute of Technology

Dr. Charles Liotta, Advisor
School of Chemistry and Biochemistry
Georgia Institute of Technology

Dr. Rigoberto Hernandez
School of Chemistry and Biochemistry
Georgia Institute of Technology

Dr. William Koros
School of Chemical and Biomolecular Engineering
Georgia Institute of Technology

Dr. Carson Meredith
School of Chemical and Biomolecular Engineering
Georgia Institute of Technology

Date Approved: June 23, 2008

For my wife Amy
The greatest thing to ever happen to me.

Also for my parents
For their love and support

ACKNOWLEDGEMENTS

I would like to thank my advisors, Professors Charles Eckert and Charles Liotta who are two of the greatest advisors a graduate student could have. Their contributions to my development were invaluable and any success that I have had as a graduate student is a result of their direction. I also extend a very special thank you to my co-advisor Professor Rigoberto Hernandez for his guidance on the computational aspects of my thesis. I am very appreciative for the resources he provided during my tenure, but am most appreciative for motivating me to succeed and pushing me forward when things seemed to stall. I also thank my remaining committee members Professors William Koros and Carson Meredith for their assistance with my thesis work and other aspects of my graduate career.

I would like to personally thank all of the members of the Eckert-Liotta group—both past and present, for their assistance and friendship. The unique group environment was the perfect fit for me and helped me grow as a researcher. I would like to single out a few group members for their individual contributions: Dr. Chris Kitchens, Dr. Jason Hallett, and Dr. David Bush for helping me get my feet wet in the lab and keeping a straight face while listening to my half-baked research ideas. Thank you to Dr. Elizabeth Hill and Ph. D. candidate Kristen Kitagawa for being the best office mates ever and putting up with my shenanigans and unique brand of humor. Dr. Laura Draucker, Ryan Hart for listening to my complaints and hanging out with me outside of school, Dr. Charu Shukla for assisting me with simulations and programming, Dr. Jie Lu for valuable insight into the world of spectroscopy, and Hillary (Trudy) Huttenhower for her Lost

discussions and always choosing me to move cylinders. Thank you to my undergraduate researchers Nathan Porter and Candice Castellino for all their contributions to my research. A very special thank you to the best undergraduate researcher of all times, Andrew Marin for his remarkable contributions to several of my projects. I wish him the best and know he will succeed in anything he does. Special thanks to the Hernandez group for their insight into computational chemistry, particularly Drs. Alexander Popov and Jeremy Moix, I would have been lost without them.

I would like to thank my family, especially my parents John Jr. and Mary for always encouraging me to succeed in whatever avenue I wanted to pursue, swimming, school, work, marriage…

Lastly I would like to thank my wife Amy Attardo Gohres. I could never have finished graduate school or my undergraduate education without her love. She made sacrifice after sacrifice for me and I am forever indebted, but I still don't want to do the laundry.

TABLE OF CONTENTS

LIST OF TABLES

LIST OF FIGURES

LIST OF SYMBOLS

S_0	ground state
S_1	first excited state
E_i	energy of event *i*
pK_a	acid dissociation constant
U_{ij}	potential energy between two bodies
ε_{ij}	Lennard-Jones energy parameter
σ_{ij}	Lennard-Jones distance parameter
r	distance
q_i	charge of species *i*
F	force
v	velocity
m	mass
t	time
T	temperature
N	number of particles
k_B	Boltzmann's constant
ε_i	dielectric constant of species *i*
n_i	refractive index of species *i*
υ	wavenumber
ρ_i	density of species *i*
λ	wavelength

Φ_i	volume fraction of species *i*
V	volume
R_{LL}	refractivity coefficient
g(x,y,z)	axial distribution function
g(r)	radial distribution function
n(x)	number of atoms at position *x*
τ_i	time constant
a_i	exponential decay pre-factor
$\vec{n}$	directional unit vector
S(t)	solvent response function of species *i*
$C_i(t)$	rotational correlation function of species *i*
$\varepsilon(\lambda)$	molar absorptivity
c	concentration
l	pathlength
K_i	equilibrium constant
m_i	molal concentration of species *i*
$\gamma_{\pm}$	ionic species activity coefficient
A_i	absorption of species *i*
I	ionization strength
f_i	fugacity of species *i*
ϕ_i	fugacity coefficient of species *i*
P	pressure

LIST OF ABBREVIATIONS

GXL	gas-expanded liquid
CO_2	carbon dioxide
SCF	supercritical fluid
GAS	gas-antisolvent
MD	molecular dynamics
C153	Coumarin 153
MeOH	methanol (methyl alcohol)
EtOH	ethanol (ethyl alcohol)
BzOH	benzyl alcohol
ACA	alkylcarbonic acid
UV	ultraviolet
Vis	visible
IR	infrared
DENAB	4-(diethylamino)-4’-nitroazobenzene
fs	femtosecond
RDF	radial distribution function
ADF	axial distribution function
MC	Monte Carlo
LJ	Lennard-Jones
ORFT	Onsager reaction field theory
3D	three dimensional

1D	one dimensional
SRF	solvent response function
RCF	rotational correlation function
DNP	2,6 dinitrophenol
Me	methyl
PBC	periodic boundary conditions
TraPPE	transferable potentials for phase equilibria
OPLS	optimized potential for liquid systems
HIPPO	high intensity pulsed preferred orientation
LANSCE	Los Alamos Neutron Science Center
GLAD	Gases Liquids and Amorphous Diffractometer
IPNS	Intense Pulsed Neutron Source
BZA	Benzoylacetone
ACN	acetonitrile
TA	Taylor-Aris
DES	Deep eutectic solvent
LDAF	Local density autocorrelation function

SUMMARY

Gas-expanded liquids (GXLs) are a unique class of tunable solvents with unlimited potential. A wide range of solvent properties and solvent interactions and complexes are possible by adjusting the amount of the gas component (*in situ*) or changing the organic liquid. Aside from solvent tunability, there are environmental and processing benefits to using GXLs. Organic solvent use is decreased, the gas component can be vented off facile separations, and the gas can act as an antisolvent for selective solute precipitation. As a result there are numerous reaction and extraction schemes and materials processing applications that could benefit from GXL use. Unfortunately, important molecular-level details that can drive a chemical process are largely unknown and limit GXL use in industrial and specialty applications. The work presented in this uses a synergistic study of experiments and computer simulations to explore solvation processes and molecular interactions in GXLs and the effects on macroscopic observables like spectroscopy, transport, and reactions.

Steady-state solvation of a laser dye is studied with spectroscopy (UV/vis and fluorescence) and molecular dynamics simulations (MD). Both experiment and theory show that organic enrichment occurs in the vicinity of the solute called the cybotactic region. Subsequently, the solvent dynamics arising by electronically perturbing the solute are studied with MD simulation. Unexpected dynamics are observed and are dependent on the organic component and gas composition. The diffusion of heterocyclic compounds is studied with MD simulations and compared to the Taylor-Aris diffusion study of former group members. The experiments and simulations do not agree, but solvent

structures obtained by simulation are shown to provide valuable insight into solvent-dependent absorption spectroscopy, or solvatochromism. Finally, dissociation constants of alkylcarbonic acids that form *in situ* in CO_2/alcohol mixtures are presented from spectroscopic measurements. Spectroscopic techniques to measure dissociation constants are well known; however, the high-pressure and multiple equilibria associated with alkylcarbonic acids hinder straight-forward measurement and analysis.

CHAPTER 1: INTRODUCTION

Gas-expanded liquids (GXLs) are a class of tunable solvents that possess the solvent strength of organic liquids and transport capabilities of supercritical fluids (SCFs). GXLs are formed by the dissolution of a gas into an organic liquid at mild temperatures and pressures (20-40°C and <60bar) to yield a volume-expanded liquid phase with properties that can be adjusted between the pure liquid and pure gas by adding or venting the gas. Consequently, GXLs are an attractive medium for reactions and separations because less organic solvent is needed and once the process is complete, the gas can be vented for facile separation. A major application that takes advantage of pressure-tunable solvent strength of GXLs is gas-antisolvent (GAS) crystallization. Solute molecules (catalysts, reactants, products, nanoparticles) can be precipitated selectively by varying the solvent composition for facile separation. A driving force of GAS and other separations and reactions is the difference in intermolecular interactions between the solvent and solute, which can affect solubility, reaction rate, and selectivity. Designing a process and selecting the appropriate solvent(s) and operating conditions requires an understanding of molecular interactions to achieve the optimal performance with the easiest separation scheme. The work presented in this thesis is a synergistic study of spectroscopic experiments and computer simulations to explore molecular interactions in GXLs. High-pressure spectroscopy and molecular dynamics (MD) simulations were used to study steady-state and dynamic solvation processes and their effects on transport properties, light absorption, and acid-catalyzed reactions.

Chapter 2 provides an in-depth background to GXLs, molecular interactions, and the spectroscopic and simulation techniques used in this study.

Chapter 3 explores steady-state solvation of a probe molecule, Coumarin 153 (C153), in CO_2-expanded methanol (MeOH) and CO_2-expanded acetone are investigated using simulation and spectroscopy. UV/vis and fluorescence spectroscopy are used to explore solvation of C153's ground and first excited-state, respectively. Specifically, the solvatochromic shift (solvent-dependent absorption or emission spectra) is measured as a function of CO_2 composition, and a simple model was developed to determine the local composition around C153. The results show that the local composition is different than the bulk composition. MD simulations also provided the local composition around C153, but also yield atomic-scale details, i.e. solvent maps around C153, that are unobtainable by experimental techniques. There is excellent agreement between the local compositions from UV/vis results and the ground state MD simulations; however, the fluorescence results and excited-state simulations disagree. Reasons for this disagreement are discussed.

Solvation dynamics are explored in Chapter 4 via MD simulations. This study explores solvent reorganization dynamics following the excitation of C153 and links the ground and excited-state solvent structures that were presented in Chapter 3. Unexpected solvation behavior is seen and is a strong function of bulk CO_2 composition, and the organic solvent. CO_2-expanded MeOH solvation timescales are similar to the neat MeOH timescale at CO_2 compositions up to 80% because of preferential organic solvation. Beyond this composition, solvation is markedly slower and sensitive to bulk composition. CO_2-expanded acetone has a maximum solvation rate at 60% CO_2, which is unexpected,

because of decreased solvent polarity. This behavior suggests that solvation in GXLs depends on two solvent properties: polarity and viscosity.

Solvent rotational dynamics provide insight into solvation mechanisms and the molecular interactions that influence solvation. MeOH's hydrogen-bonded structure slows rotation. The addition of CO_2 decreases the solvent viscosity, breaks up the hydrogen bond network, and facilitates reorganization. On the other hand, acetone and CO_2 molecules become more mobile with CO_2 addition from decreased viscosity. This study applies the local organic enhancements that were calculated in Chapter 3 and applies the tunable solvent properties of GXLs to solvation dynamics.

Chapter 5 examines the solvatochromic behavior of five heterocyclic compounds in CO_2-epanded MeOH and solvent clustering behavior with MD simulations. The solutes were chosen because their structures are similar, but the placement of nitrogen atoms on the aromatic ring gives different dipole moments which alter solvent clustering behavior and ultimately impacts spectroscopy. Solvent structures are a basis to rationalize the solvatochromic behavior and demonstrate the sensitivity of solvation patterns to solute changes.

Chapter 6 presents a novel technique to measure the acid dissociation constant (pK_a) of alkylcarbonic acids (ACAs). ACAs form *in situ* from the equilibrium reaction between CO_2 and alcohols in CO_2-expanded alcohols. This group has used these acids as acid catalysts and polarity switches in reversible ionic liquid solvents, but the strengths, or pK_a, are not known. UV/vis spectroscopy was used to study ACA equilibria. Past investigations of ACA ionization constants encountered analysis complications due to multiple equilibrium reactions and high-pressure nature of the solvents. These problems

were overcome by a careful degree-of-freedom analysis that will be detailed in the chapter.

Appendices A and B are figures and tables that were not included in Chapters 3 and 4. Appendix C explores diffusion of the heterocyclic solutes from Chapter 5 in CO_2-expanded MeOH with MD simulations. The results in neat MeOH are in good agreement with experimental data taken by former group members, but the simulations predict faster diffusion in the GXLs. The same trend of faster diffusion with more CO_2 that was seen in the experiments was also predicted by the simulations; however, MD simulations did not predict the actual diffusion coefficients in GXL conditions.

Appendix D describes a computational investigation of solvent effects on tautomeric equilibrium. The purpose of this project was to use the tunable properties of several different GXLs (MeOH, acetonitrile, and cyclohexane) to change the isomeric distribution of the keto and enol forms of the tautomerizing molecule benzoylacetone. The goal was to measure tautomeric equilibrium constants in the different GXLs with infrared (IR) spectroscopy and explore solvent-solute interactions with MD simulations. Unfortunately the high-pressure IR cell had too large a pathlength and the ZnSe windows absorbed most of the incident light. The MD simulations predicted Gibbs free energies of the tautomeric equilibrium process and the results and procedure are discussed.

Appendix E discusses solvent effects on the *cis/trans* isomerization reaction rate of N,N diethylnitroazobenzene (DENAB) in GXLs. The isomerization rate was observable by our detection method in non-polar GXLs and showed little dependency on CO_2 composition. The reaction was too fast in polar GXLs, like CO_2-expanded acetone,

to measure with our instrumentation. A detector with fs resolution is required to monitor this reaction in polar solvents.

Appendix F presents fluorescence and UV/vis spectroscopic results of the fluorophore ellipticine to measure the pK_a of ACAs. This project paved the way for the ACA study described in Chapter 6, but itself had problems with the spectral analysis and sensitivity to water.

Appendix G summarizes neutron scattering experiments in GXLs performed at Los Alamos and Argonne National Laboratories. CO_2-expanded MeOH and acetone were investigated to compare to MD simulation results. Neutron scattering was stopped due to equipment failure.

Appendix H discusses MD simulations in a deep eutectic formed by urea and fructose at 65°C. Solvent structures of two compositions were explored with radial distribution functions (RDFs) and indicate that hydrogen bonding between the two components is important in forming the eutectic. Solvent dynamics were studied with local density autocorrelation functions to highlight strong and persistent urea-fructose solvent complexes.

CHAPTER 2: BACKGROUND ON GAS-EXPANDED LIQUIDS, SPECTROSCOPY, AND MOLECULAR DYNAMICS SIMULATIONS

Gas-Expanded Liquids

Solvents have a huge impact on chemical processing.[1] They can enhance or hinder reaction rates, dictate a separation process, and impact the environment and human health. Unfortunately the perfect solvent does not exist. For example a solvent that could enhance catalyst solubility may be difficult to remove in a downstream separation process. Tunable solvents add versatility and flexibility to the solvent properties. The best known tunable solvents are supercritical fluids (SCFs) which consist of a fluid that has been heated and pressurized above the critical point—the thermodynamic point where the liquid and gas densities merge and the liquid phase ceases to exist. SCFs have both liquid and gas like properties, but most importantly the density and consequently solvent properties can be tuned by adjusting pressure, and venting removes the solvent system. SCFs have tunable solvation solvent strength, a built in separation mechanism, negligible surface tension, and gas-like transport properties; however, the operating conditions, particularly pressure, are extreme and escalate capital equipment costs. Additionally the solvent strengths are significantly weaker than organic solvents. Solvent strength can be increased by adding cosolvent amounts (<10%) of an organic solvent, but the high pressures limit SCF use in industry.

Gas-expanded liquids (GXLs) are the next generation of tunable solvents that combine the benefits of SCFs and organic liquids.[2, 3] These solvents are formed by the

dissolution of a gas, most often CO_2, into an organic solvent to form a volume-expanded liquid phase with pressure-tunable properties that can be reversed by venting. Figure 2.1 illustrates these GXL operating principles. GXLs operate at lower pressures the SCFs, <60bar versus hundreds of bars, and the large organic composition increases the solvent strength. The drawbacks are decreased fluidity and residual organic solvent that preclude a completely facile separation. As a result SCFs and GXLs are suited for different applications. SCFs are attractive as extraction and reaction media for mass-transfer limited processes because the gas-like viscosity can effectively penetrate porous and solid matrices. The strong and tunable solvation power makes GXLs attractive for antisolvent and catalysis applications.

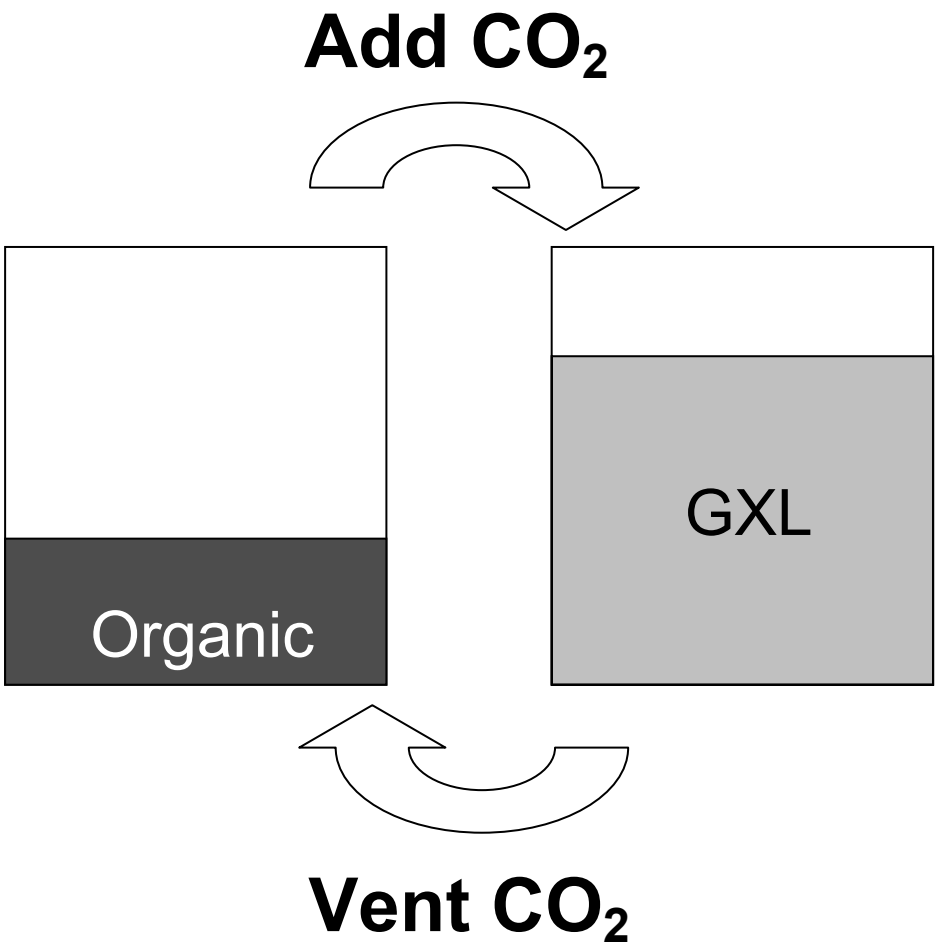

Figure 2.1: GXL operating procedures

The most well-known GXL application is gas-antisolvent (GAS) crystallization which utilizes the poor solvent strength of the gaseous species to precipitate solute molecules. This has been demonstrated in the size-selective precipitation of nanoparticles[4-6] and reaction products, but could also be used to separate catalysts from solution. Catalytic reactions like hydroformylations and oxidations capitalize on increased gas solubility (O_2, H_2) in GXLs, which leads to faster reaction rates relative to the neat organic liquid.[7-9] Acid catalyzed reactions are possible with self-neutralizing

alkylcarbonic acids[10-13] that form in CO_2-expanded alcohols. These applications reflect the versatility of GXLs and GXLs can be chosen for a particular process if molecular interactions are known. Solvent interactions with a solute molecule can greatly impact macroscopic observables like phase behavior, solubility, reaction rate and selectivity; therefore, this thesis studies molecular-scale phenomena in GXLs to exploit them in chemical reactions and separations.

The Cybotactic Region

The dissolution of a solute molecule can disrupt the bulk solvent landscape because different intermolecular interactions are introduced.[14] Solute-induced disruptions are termed the cybotactic region, defined as the solvent region(s) impacted by the presence of a solute molecule. A schematic representation of the cybotactic region is shown in Figure 2.2. The cybotactic region is represented by the circle surrounding the large gray solute molecule and solvent molecules. This figure highlights the effects of solute-solvent interactions, showing that the composition and/or density in the cybotactic region can deviate significantly from the bulk composition or density. This local solvent composition can impact reaction rates, solubility, and spectroscopy. As a result the local composition in the cybotactic region has been the focus of much research and is a central theme to this thesis.

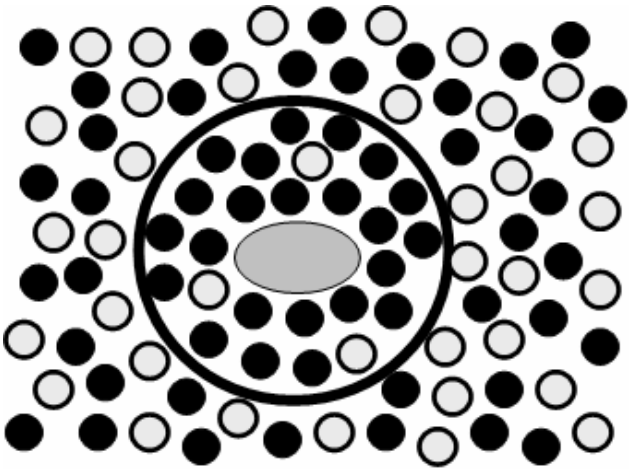

Figure 2.2: Schematic view of cybotactic region.

This thesis extends the work of computational and spectroscopic studies performed in other tunable solvents, particularly SC-CO_2. Many studies have used solvatochromic dyes to probe the cybotactic region in SCFs[15-18] and co-solvent modified (<10% organic) SCFs.[19-22] These studies used similar analytical techniques to those presented in this thesis to study local solvent composition or local density enhancements in SCFs. Pioneering work by Kim and Johnston[15] explored local density clustering around the dye phenol blue with spectroscopy. They developed a simple modeling technique to extract local densities from absorbance spectra. Rice et al[16] developed a spectroscopy model based on solvent properties to obtain better estimates for local density. Several research groups[21, 22] extended these modeling techniques to co-solvent modified SCFs. In these studies the focus shifted to local composition enhancements because they are mixed solvents. More recently, MD simulations have been used to study local solvent behavior in SCFs.[23] Using MD simulations to create solvent maps has been performed in SCFs with different solutes and is central to this study of the cybotactic region.[24, 25] Maroncelli et al used MD simulations to study density enhancements around

stilbene molecules.[24] In addition to solvent maps, they explored the effect of local viscosity on rotations and local density effects on spectroscopy. Favero and Skaf explored local solvation patterns of CO_2 around alkaloids, including caffeine. This study links local solvation with the most well known application of CO_2 natural product extraction. The previous work on local solvation in SCFs sets the tone for this thesis. Many of the concepts from these SCF studies form the foundation for this work in GXLs; however, GXLs present different challenges than those faced in SCFs.

Spectroscopy & Solvatochromism

The absorption reorganizes a chromophore's electronic structure and typically results in a charge-separated excited state. The relative ease of charge separation is related to the energy of transition required to excite the molecule. This determines which wavelength(s) of light the chromophore absorbs. Any variable that can assist or hinder charge separation alters the energy of transition and will ultimately affect the absorption spectra. One such variable is the solvent. Solvent-solute interactions impact the electronic reorganization process. This solvent-dependent absorption (or emission) phenomenon is called solvatochromism and is a common technique to probe molecular interactions. If the dipole moment increases upon excitation, increasingly polar solvents increase the absorption wavelengths (i.e. lower energy of transition). This is called positive solvatochromism and is the typical solvent-facilitated absorption process. Conversely, negative solvatochromism occurs if the dipole moment decreases following excitation, in which case increasingly non-polar solvents lead to absorption at higher wavelengths. These general solvatochromic principles apply to emission or fluorescence spectroscopy described next.

Once a chromophore becomes electronically excited, it must return to the ground state. In this work two mechanisms are applicable: 1) radiative decay where the chromophore emits light, or fluoresces and 2) non-radiative decay where the chromophore relaxes through molecular vibrations. A typical absorption/emission energy diagram is provided in Figure 2.3. Light absorption rearranges the chromophore's dipole moment; absorption maximum is related to the transition energy. Solvent molecules around the solute (in the cybotactic region) are initially perturbed and realign their dipoles with the excited state chromophore dipole. This process is called solvent reorganization or solvation dynamics and is the focus of Chapter 4. The excited-state is solvated by an equilibrium solvent configuration and the chromophore emits light to decay back to the ground state. The emitted wavelength provides information about excited-state solvent structure and is dependent on the solvent composition—specifically the local composition. After emission, solvent molecules reorganize again to re-solvate the ground-state dipole.

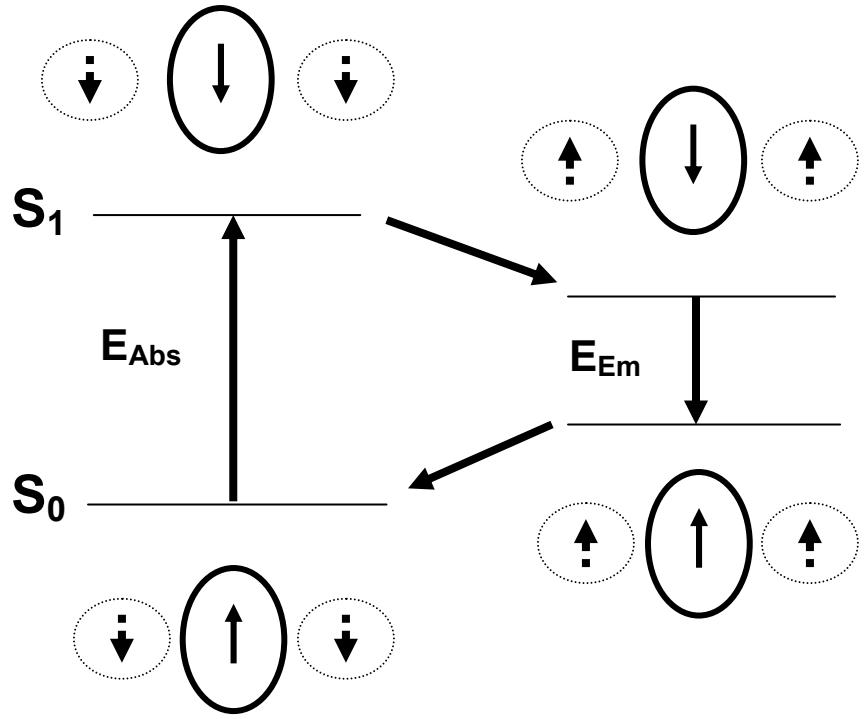

Figure 2.3: Absorption and emission energy diagram and solvation processes.

Molecular Dynamics Simulations

Simulation is a valuable tool that provides researchers with atomic-scale information that is otherwise unobtainable with experimental techniques. Simulations can also serve as a direct comparison to experimental results. Classical molecular systems are often simulated using Monte Carlo (MC) and Molecular Dynamics (MD). Quantum chemical simulations and hybrid classical/quantum mechanical simulations are advantageous for some applications and provide valuable insight into electronic structure; however, they are not computationally feasible for large systems and are not considered in this study. MC simulations are useful to study fluid structure and phase behavior and have been applied to CO_2-expanded systems;[26-28] however, solvent dynamics are a key component to this work and thus MC simulations are not well suited to this study. MD

simulations are well suited for exploring equilibrium structures and non-equilibrium dynamics and the basic principles will be discussed in detail to provide readers with sufficient background.

MD simulations integrate the equations of motion on atoms or molecules and the positions, velocities, and forces of each species are updated at each timestep.[29] Atoms are modeled as infinitesimal points with a potential function that describes interactions between other molecules. Potential functions, or force fields, contain non-bonded, bond stretch, angle bend, and dihedral terms to describe the electrostatic and intramolecular energy associated with molecular motion. Simple molecules and geometrically constrained species sometimes ignore intramolecular potentials and treat the molecules as rigid bodies with non-bonded interactions. Larger and flexible molecules like proteins and polymers must take intramolecular interactions into account. A common non-bonded force field and the one used in this work is the Lennard-Jones plus Coulombic potential:

$$U_{ij} = 4\varepsilon_{ij}\left\{\left(\frac{\sigma_{ij}}{r_{ij}}\right)^{12} - \left(\frac{\sigma_{ij}}{r_{ij}}\right)^{6}\right\} + \frac{q_i q_j}{r_{ij}} \qquad \text{Equation 2.1}$$

where U is the potential energy, ε is the Lennard-Jones well-depth or energy parameter, σ is the Lennard-Jones distance parameter or atomic radius, r is the interatomic distance, and q is the partial charge of an atom. The subscripts i and j denote different atoms. An ensemble must be defined that specifies which simulation variables remain fixed. The three most common ensembles are the microcanonical (NVE, where N is the number of atoms, V is volume, and E is energy), canonical (NVT, where T is temperature), and grand canonical (NPT, where P is pressure) ensembles. The first two use periodic boundary conditions to fix the volume and the last uses a barostat, i.e. a movable piston,

to regulate pressure. Temperature is regulated by a thermostat. Barostats and thermostats require a time constant parameter that reflects how strongly the pressure or temperature regulator is coupled to the system.

A MD code integrates the equations of motion numerically by finite-difference methods, usually the forward Euler method. The most common integration algorithm for MD simulations is the Verlet algorithm. The software package used in this work, DL_POLY,[30] calculates the positions and forces at each timestep with a half-step lag in the velocities to decrease compounded error associated with property (i.e. energy, temperature) drift. The Verlet integration algorithm is a multi-step process that begins by calculating the forces from the potential function:

$$F_i(t) = \frac{dU}{dr_i} \qquad \text{Equation 2.2}$$

where the subscript *i* denotes the Cartesian component of the force (*F*) or position (*r*). Velocities (*v*) are updated by a half timestep:

$$v(t + \tfrac{1}{2}\Delta t) = v(t - \tfrac{1}{2}\Delta t) + \tfrac{1}{2}\Delta t \frac{F(t)}{m} \qquad \text{Equation 2.3}$$

where *t* is time, Δt is the timestep typically ~1fs, and *m* is the mass of the site. Atomic positions are then updated with the new half-step velocities:

$$r(t + \Delta t) = r(t) + \Delta t \cdot v(t + \tfrac{1}{2}\Delta t) \qquad \text{Equation 2.4}$$

Properties are calculated at the same timestep as the positions instead of a half-step behind. DL_POLY averages the velocities at t ± ½Δt to calculate observables like temperature:

$$T = \frac{\sum_{i=1}^{N} m v_i^2}{N k_B}$$ Equation 2.5

where N is the number of atoms and k_B is Boltzmann's constant. The integration procedure is repeated at each timestep. An initial configuration of atomic positions is required to start a simulation and usually includes an equilibrium period where velocities are rescaled to prevent instability. Equilibrations are typically several hundred picoseconds and ensure that a stable initial configuration is generated for statistical sampling simulations. Dynamic and structural data require statistical averaging because one simulation is a small representation of an actual system. The more samples used to calculate a property by more particles, more trajectories, or higher sampling frequency increases the accuracy of a calculated property. Consequently, properties calculated in this work represent the ensemble average of many trajectories.

References

1. Reichardt, C., *Solvents and Solvent Effects in Organic Chemistry*. 2nd ed.; VCH: Weinheim, Germany, 1988.

2. Hallett, J. P.; Kitchens, C. L.; Hernandez, R.; Liotta, C. L.; Eckert, C. A., Probing the cybotactic region in gas-expanded liquids (GXLs). *Acc. Chem. Res.* **2006,** 39, (8), 531-538.

3. Jessop, P. G.; Subramaniam, B., Gas-expanded liquids. *Chem. Rev.* **2007,** 107, (6), 2666-2694.

4. McLeod, M. C.; Anand, M.; Kitchens, C. L.; Roberts, C. B., Precise and rapid size selection and targeted deposition of nanoparticle populations using CO2 gas-expanded liquids. *Nano Lett.* **2005,** 5, (3), 461-465.

5. Kitchens, C. L.; Roberts, C. B., Copper nanoparticle synthesis in compressed liquid and supercritical fluid reverse micelle systems. *Ind. Eng. Chem. Res.* **2006,** 45, (4), 1550-1550.

6. Anand, M.; You, S. S.; Hurst, K. M.; Saunders, S. R.; Kitchens, C. L.; Ashurst, W. R.; Roberts, C. B., Thermodynamic analysis of nanoparticle size selective fractionation using gas-expanded liquids. *Ind. Eng. Chem. Res.* **2008,** 47, (3), 553-559.

7. Musie, G.; Wei, M.; Subramaniam, B.; Busch, D. H., Catalytic oxidations in carbon dioxide-based reaction media, including novel CO2-expanded phases. *Coord. Chem. Rev.* **2001,** 219, 789-820.

8. Wei, M.; Musie, G. T.; Busch, D. H.; Subramaniam, B., CO2-expanded solvents: Unique and versatile media for performing homogeneous catalytic oxidations. *J. Am. Chem. Soc.* **2002,** 124, (11), 2513-2517.

9. Jin, H.; Subramaniam, B.; Ghosh, A.; Tunge, J., Intensification of catalytic olefin hydroformylation in CO2-expanded media. *Aiche J.* **2006,** 52, (7), 2575-2581.

10. West, K. N.; Wheeler, C.; McCarney, J. P.; Griffith, K. N.; Bush, D.; Liotta, C. L.; Eckert, C. A., In situ formation of alkylcarbonic acids with CO2. *J. Phys. Chem. A* **2001,** 105, (16), 3947-3948.

11. Chamblee, T. S.; Weikel, R. R.; Nolen, S. A.; Liotta, C. L.; Eckert, C. A., Reversible in situ acid formation for beta-pinene hydrolysis using CO2 expanded liquid and hot water. *Green Chem.* **2004,** 6, (8), 382-386.

12. Weikel, R. R.; Hallett, J. P.; Liotta, C. L.; Eckert, C. A., Self-neutralizing in situ acid catalysts from CO2. *Topics in Catalysis* **2006,** 37, (2-4), 75-80.

13. Weikel, R. R.; Hallett, J. P.; Liotta, C. L.; Eckert, C. A., Self-neutralizing in situ acid catalysis for single-pot synthesis of iodobenzene and methyl yellow in CO2-Expanded methanol. *Ind. Eng. Chem. Res.* **2007,** 46, (16), 5252-5257.

14. Eckert, C. A.; Ziger, D. H.; Johnston, K. P.; Kim, S., Solute partial molal volumes in supercritical fluids. *J. Phys. Chem.* **1986,** 90, (12), 2738-2746.

15. Kim, S.; Johnston, K. P., Clustering in supercritical fluid mixtures. *AIChE J.* **1987,** 33, (10), 1603-1611.

16. Rice, J. K.; Niemeyer, E. D.; Dunbar, R. A.; Bright, F. V., State-Dependent Solvation of Pyrene in Supercritical CO2. *J. Am. Chem. Soc.* **1995,** 117, (21), 5832-5839.

17. R., B.; Lewis, J. E.; Maroncelli, M., Electronic spectral shifts, reorganization energies, and local density augmentation of Coumarin 153 in supercritical solvents. *Chem. Phys. Lett.* **1999,** 310, 485-494.

18. Lewis, J. E.; Biswas, R.; Robinson, A. G.; Maroncelli, M., Local density augmentation in supercritical solvents: electronic shifts of Anthracene derivatives. *J. Phys. Chem B* **2001,** 105, 3306-3318.

19. Yonker, C. R.; Smith, R. D., Solvatochromic behavior of binary supercritical fluids: the carbon dioxide/2-propanol system. *J. Phys. Chem* **1988,** 92, 2374-2378.

20. Tomasko, D. L.; Knutson, B. L.; Pouillot, F.; Liotta, C. L.; Eckert, C. A., Spectroscopic study of structure and interactions in cosolvent modified supercritical fluids. *J. Phys. Chem* **1993,** 97, 11823-11834.

21. Schulte, R. D.; Kauffman, J. F., Solvation in mixed supercritical fluids: TICT spectra of bis(4,4'-aminophenyl) sulfone in ethanol/CO2. *J. Phys. Chem* **1994,** 98, 8793-8800.

22. Kelley, S. P.; Lemert, R. M., Solvatochromic characterization of the liquid phase in liquid-supercritical CO2 mixtures. *Aiche J.* **1996,** 42, (7), 2047-2056.

23. Tucker, S. C., Solvent density inhomogeneities in supercritical fluids. *Chem. Rev.* **1999,** 99, 391-418.

24. Patel, N.; Biswas, R.; Maroncelli, M., Solvation and Friction in Supercritical Fluids: Simulation-Experiment Comparisons in Diphenyl Polyene/CO2 Systems. *J. Phys. Chem. B* **2002,** 106, 7096-7114.

25. Favero, F. W.; Skaf, M. S., Solvation of purine alkaloids in supercritical CO2 by molecular dynamics simulations. *J. Supercrit. Fluids* **2005,** 34, 237-241.

26. Moon, S. D., Monte Carlo simulation for vapor-liquid equilibrium of binary mixtures CO2/CH3OH, CO2/C2H5OH, and CO2/CH3CH2CH2OH. *Bull. Korean Chem. Soc.* **2002,** 23, (6), 811-816.

27. Stubbs, J. M.; Siepmann, J. I., Binary phase behavior and aggregation-of dilute methanol in supercritical carbon dioxide: A Monte Carlo simulation study. *J. Chem. Phys.* **2004,** 121, (3), 1525-1534.

28. Houndonougbo, Y.; Jin, H.; Rajagopalan, B.; Wong, K.; Kuczera, K.; Laird, B. B., *J. Phys. Chem. B* **2006,** 110, (26), 13195-13202.

29. Allen, M. P.; Tildesley, D. J., Computer Simulations of Liquids. In Oxford University Press: Oxford, 1987.

30. Smith, W.; Forester, T. R., DL_POLY_2.0: A general-purpose parallel molecular dynamics simulation package. *J. Molecular Graphics* **1996,** 14, (3), 136-141.

CHAPTER 3: LOCAL COMPOSITION ENHANCEMENTS IN GAS-EXPANDED LIQUIDS: A SYNERGISTIC STUDY OF EXPERIMENTS AND THEORY

Introduction

Solvent interactions with a solute molecule—an extractant, reactant/product, or catalyst – can change the solution chemistry and ultimately affect macroscopic observables. Examples include solubility, kinetics, reaction selectivity, and spectroscopy. As a result solute-solvent interactions should be understood and considered when selecting a solvent or designing a chemical process. GXLs offer a wide range of solvent interactions that can be adjusted by changing the gaseous species concentration. This provides advantages over traditional organic liquids because solvent characteristics can be manipulated *in situ*. The work presented in this chapter uses a combination of spectroscopy and MD simulation to explore solvation in two GXLs: MeOH/CO_2 and acetone/CO_2. The synergistic approach is advantageous over the independent methods because the simulations provide atomic-level detail and experiments verify the simulation results and indicate which GXLs to simulate.

Combined computational and experimental studies have become a common practice to study solvent systems like organic liquids,[1, 2] SCFs,[3, 4] and ionic liquids. This work is among the first to use MD simulations and spectroscopy to study GXLs.[5-7] Previous MD simulations by this group and others showed that GXLs are heterogeneous solvents composed of organic clusters that vary in size and persistence with composition.[8, 9] This unique solvent structure demonstrates the versatility of these solvents and the ability to change the microscopic solvent landscape by altering the bulk composition. The addition of a solute molecule to the system further impacts the solvent

landscape and gives rise to the cybotactic region;[10] defined as the area of solvent impacted by the solute. The solvent composition in the cybotactic region can be very different from the bulk composition because of solvent-solute interactions and this composition affects the solution chemistry as previously noted. Consequently, this work uses experiments and simple solvation models to predict this local composition and MD simulations to create solvent maps around the solute and serve as a comparison to experimental local compositions.

Background and Methods

The solvatochromic absorption and emission behavior of C153 were investigated over a range of CO_2 compositions. The structure of C153 and the charge distribution of the ground and first excited state are shown in Figure 3.1. The absorption maximum (λ_{max}) is related to the transition energy required to promote an electron from the HOMO to LUMO. This energy is affected by relatively short-ranged solvent-solute interactions and thus λ_{max} provides insight into the solvent composition surrounding C153. It was assumed that solvent molecules that are affected by the solute molecule, i.e. in the cybotactic region, contribute to the solvatochromic behavior. Similarly, emission maxima are affected by the solvent composition around the excited-state C153. If the effects of solvent composition on λ_{max} can be modeled, then local composition in the cybotactic region can be inferred. Onsager's Reaction Field Theory[11] (ORFT) relates solvatochromic shift relative to the maxima in vacuum to solvent polarity.

$$\Delta\upsilon = A\left(\frac{\varepsilon-1}{\varepsilon+2}-\frac{n^2-1}{n^2+2}\right)+B\left(\frac{n^2-1}{2n^2+1}\right) \qquad \text{Equation 3.1}$$

where $\Delta\nu$ is the solvatochromic shift relative to the value in vacuum (ν_0), in cm^{-1}, ε and n are the solvent dielectric constant and refractive index respectively. The parameters A and B are solute-dependent constants that were treated as adjustable parameters in this work, but fell within the range provided by Maroncelli et al.[3] Values for A, B, and ν_0 used in this work are presented in Table 3.1.

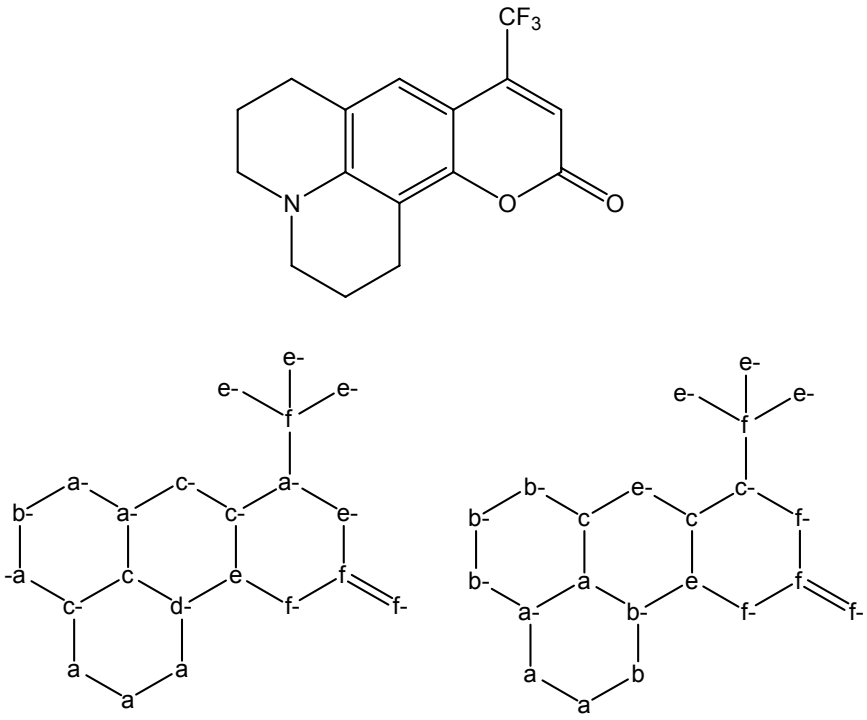

Figure 3.1: Molecular structure of C153 (top) and charge distribution of the ground (bottom left) and first excited state (bottom right). Lettering scale is used to illustrate partial charge distribution: a: |q| < 0.1, b: 0.1 < |q| < 0.2, c: 0.2 < |q| < 0.3, d: 0.3 < |q| < 0.4, e: 0.4 < |q| < 0.5, f: |q| > 0.5.

Table 3.1: Parameters used in Equation 3.1 and parameters from Reference 3.3 for comparison.

Co-solvent	Spectroscopy	A	B	υ_0 (10^{-3} cm^{-1})
Acetone	Absorption	-1.6	-11.8	27.1
Methanol	Absorption	-1.9	-11.8	27.1
Ref. 3.3	Absorption	-2.1 to -2.8	-8.0 to -10.0	25.3 to 27.9
Acetone	Emission	-1.0	-8.1	21.6
Methanol	Emission	-2.2	-7.9	21.6
Ref. 3.3	Emission	-3.8 to -5.2	-6.0 to -10.0	20.8 to 23.3

The two parts of the Equation 3.1 describe two solvent-induced events that occur upon chromophore excitation. The first term is the solvent's orientation polarization, found by subtracting inductive polarization effects (refractive index term) from electrostatic effects (the dielectric constant term). This describes the solvent's ability to realign its dipole moment with the newly created excited-state dipole moment and is applicable only in polar solvents. This term is zero in cases where $\varepsilon = n^2$ — i.e. non-polar solvents – because non-polar solvents have no net dipole to realign with the chromophore's dipole. All solvatochromic effects are due to induced dipole effects, which are described by the second term in Equation 3.1. The fastest step of the excitation process is electron polarization from induced dipole effects. This is a strict function of refractive index, which describes light interaction with the medium. By inspection, non-polar solvation typically has a smaller effect on solvatochromic shift than polar solvation.

ORFT requires the refractive indices and dielectric constant in each GXL considered, which is challenging to obtain in mixed solvents. Data exist for MeOH/CO_2

at 35C, but are unavailable at the conditions used in this work. Data are not available in acetone/CO_2 GXLs. Mixing rules provide a reasonable estimate in the absence of data and can be applied to any other GXL or solvent mixture in the technique described in the proceeding sections.

The Lorenz-Lorentz mixing rule[12] (Equation 3.2) is a widely used method for estimating refractive indices of mixtures and has been applied to liquids[13] and SCFs.[14, 15]

$$\frac{(n_{mix}-1)^2}{(n_{mix}+2)^2} = \sum_{i=1}^{N} \Phi_i \frac{(n_i-1)^2}{(n_i+2)^2} \qquad \text{Equation 3.2}$$

where Φ is the volume fraction, N is the number of components in the mixture, and the subscript i denotes the species. The refractive index of pure CO_2 at each operating density were found by the Buckingham and Pople formulation[16] (Equation 3.3) with virial refractivity coefficients from Besserer and Robinson[17] (Equation 3.4). Refractive indices of MeOH and acetone were obtained from the literature.[18]

$$R_{LL} = R_{LL}^0 + B\rho + C\rho^2 \qquad \text{Equation 3.3}$$

$$R_{LL} = \frac{1}{\rho}\frac{n^2-1}{n^2+2} \qquad \text{Equation 3.4}$$

where R_{LL} is the refractivity coefficient, the superscript "0" denotes the refractivity at zero density (extrapolated), coefficients B and C are the respective second and third virial coefficients of CO_2, and ρ is the density of CO_2 at the operating temperature and pressure.

A number of mixing rules are available to estimate dielectric constants in mixtures. GXLs require extra consideration because heterogeneous solvent clusters disrupt linear dielectric behavior. This is especially true in self-associating solvents like alcohols,[19] where hydrogen bonding leads to heterogeneous solvent clusters, amplified

when the GXL is formed. Bruggeman developed a mixing rule (Equation 3.5) for heterogeneous mixtures by differentially increasing the concentration of a dispersed species to gradually change the dielectric constant.[20] Consequently his equation is an asymmetric mixing rule that depends on which component is chosen as the dispersed species.

$$\frac{\varepsilon_{mix} - \varepsilon_d}{\varepsilon_c - \varepsilon_d}\left(\frac{\varepsilon_c}{\varepsilon_{mix}}\right)^{1/3} = 1 - \Phi_d \qquad \text{Equation 3.5}$$

where ε is the dielectric constant and Φ is the volumetric fraction. The subscript *c* refers to the continuous species and *d* the dispersed species. In this work the organic species was chosen as the dispersed species because this led to the best agreement with available MeOH/CO_2 dielectric data,[21, 22] particularly in the low-organic concentration regime where organic clustering is more prevalent.

Materials

C153 and HPLC grade solvents were used as received from Sigma-Aldrich. Carbon Dioxide was obtained from Airgas and dried over molecular sieves prior to use.

Equipment and Methods

Absorption spectra were recorded using a Hewlett-Packard 1050 Series UV detector. Emission spectra were recorded using an Ocean Optics USB2000 fiber optic detection system. The incident light source was a Kratos LH151 N/2 short arc lamp with 1000Watt power controlled with a monochrometer. All spectra were analyzed via Origin v7.5 software from Origin Labs. All samples were loaded into a high-pressure optical cell with sapphire windows and a cooling jacket connected to an external ethylene glycol chiller. Temperature was monitored by contacting the liquid phase with an Omega J-type thermocouple with ±0.1°C precision. Pressure was monitored with a Druck pressure

transducer with ±1psi precision calibrated with a hydraulic counterweight apparatus from Ruska. Carbon dioxide was introduced into the cell with an Isco syringe pump.

1mL of mM C153 in MeOH was introduced to the cell (regardless of co-solvent) and dried under vacuum for several hours. Fresh solvent was added and to the cell as needed and sealed. CO_2 was then introduced to the cell and thermostated at 298K for several hours before recording spectra, to ensure that equilibrium was achieved. The samples were stirred throughout the experiment with a magnetic stir bar to maintain uniform conditions. For the fluorescence experiment, the emitted light was detected perpendicular to the incident beam.

Computational Models and Methods

All molecules were treated as rigid bodies with Lennard-Jones (LJ) (6-12) plus Coulombic potential given by Equation 3.6.

$$U_{ij} = 4\varepsilon_{ij}\left\{\left(\frac{\sigma_{ij}}{r_{ij}}\right)^{12} - \left(\frac{\sigma_{ij}}{r_{ij}}\right)^{6}\right\} + \frac{q_i q_j}{r_{ij}} \qquad \text{Equation 3.6}$$

where i and j are interaction sites on two separate molecules, r_{ij} is the distance between the two sites, and q is the partial charge. LJ parameters ε and σ are the well-depth and atomic radius site-site interaction terms obtained by the Lorentz-Berthelot combining rules: $\varepsilon_{ij}(\varepsilon_{ii}\,\varepsilon_{jj})^{1/2}$ and $\sigma_{ij} = ½(\sigma_{ii} + \sigma_{jj})$. CO_2 pair interactions were modeled with the TrAPPE[23] (Transferable Potentials for Phase Equilibrium) potential. MeOH and acetone were modeled with the J2[24] and OPLS[25] (Optimized Potential for Liquid Systems) derived potentials respectively. C153 LJ parameters were obtained from the OPLS model[26] and were assumed to be the same in ground (S_0) and excited states (S_1). C153 partial charges (S_0 and S_1) were obtained from Maroncelli et al.[2]

Simulations were performed in the DL_POLY package (V2)[27] with added subroutines developed in-house. The equations of motion were integrated with the Verlet leapfrog algorithm with a timestep of 3fs. Coulombic interactions were handled internally by DL_POLY with the Ewald summation method with a specified tolerance of 1.0×10^{-5}. Rigid bodies were also handled by DL_POLY with the SHAKE algorithm. The system consisted of a single C153 molecule in 500 total solvent molecules (CO_2 and organic) for 20% and 5% organic GXLs and 1000 total solvent molecules for 2% organic GXLs. Initial configurations were generated by randomly orienting solvent molecules around C153 in a simulation box whose size was determined via the Patel-Teja equation of state.[28] The equilibrium solvent structures were investigated in the canonical (NVT) ensemble, meaning the number of molecules, volume, and temperature were held fixed. Temperature was regulated with a Nose-Hoover thermostat with relaxation time of 5ps.[29] Each initial configuration was equilibrated (velocity rescaling every step) for 400ps under NVT conditions before a 500ps NVT simulation in which configurations were saved every 1.5ps to compute the average local composition around C153. Statistics were taken every 30fs to compute the structural function $g(x,y,z)$ at the simulation's end.

Solvent maps represent the average distribution of different solvent molecules around a solute probe. Molecules fluctuate around an average energy in equilibrium MD simulations and therefore statistics must be taken to obtain the average value of observables like structural distribution functions. Typically, fluid structure is investigated with 1-dimensional radial distribution functions (RDFs), which show the most probable distance between two types of atoms. The addition of large solute molecules complicates the structural investigation because spatial resolution is lost in a single dimension, i.e.

average distances do not include effects from nearby atoms on the solute molecule. Consequently higher dimension distribution functions were used to investigate the solvent structure around C153. The trade-off for better resolution is longer simulations to obtain adequate statistics.

A 3-dimensional (3D) distribution function was calculated for each solvent species relative to the C153 center-of-mass. Cartesian coordinates were used to calculate the 3D axial distribution function[6] (ADF) instead of radial coordinates to simplify the analysis and better capture the resolution around the C153 functionality. The ADF or *g(x,y,z)* can be determined via Equation 3.7:

$$g(x,y,z) = \frac{\langle n_i(x,y,z) \rangle}{\rho_i dV} \qquad \text{Equation 3.7}$$

where $\langle n_i(x,y,z) \rangle$ is the average number of particles of atom *i* in a finite element of volume *V* and coordinates x, y, and z relative to the C153 center-of-mass. The ADF is the ratio of number density of species *i* in a finite element to the bulk number density in the simulation box, ρ_i. The statistical acquisition method first normalizes the atomic coordinates to a new periodic coordinate system with C153 center-of-mass as the origin and two relative vectors from the center of mass to define the *x* and *y* axes. The z-axis is the cross-product of these two vectors. The new simulation box is divided into 10^6 finite elements and the number of each type of solvent atom in each finite element is recorded as a histogram every 10 steps.

Results and Discussion

UV/Vis Spectroscopy

Normalized UV/vis spectra for CO_2-expanded MeOH and CO_2-expanded acetone are shown in Figure 3.2 and Figure 3.3 respectively. The neat organic spectra are shown in the respective Figures and the neat CO_2 absorption spectrum is included in both. As the CO_2 concentration increases there is a blue (hypsochromic) shift to higher wavenumber, indicating a decrease in solvent polarity around C153. The important value for each spectrum is the peak maximum, υ_{max} (λ_{max}). As previously mentioned, υ_{max} is related to the transition energy and ultimately local solvent polarity by Equation 3.1 The maxima in both GXLs (MeOH and acetone) are plotted versus CO_2 composition in Figure 3.4 to demonstrate the effects of solvent composition on absorption spectra. The absorption maximum in vacuum, υ_0, has been subtracted to highlight solvation effects on absorption. The maxima in GXLs with less than 80% CO_2 resemble the maxima in neat organic solvents. This implies that C153 is in a polar environment, suggesting preferential organic solvation. Beyond 80% CO_2 there is a sharp decline which indicates increasing CO_2 solvation. Another important feature of Figure 3.4 is the merger of MeOH and acetone maxima at high CO_2 composition.

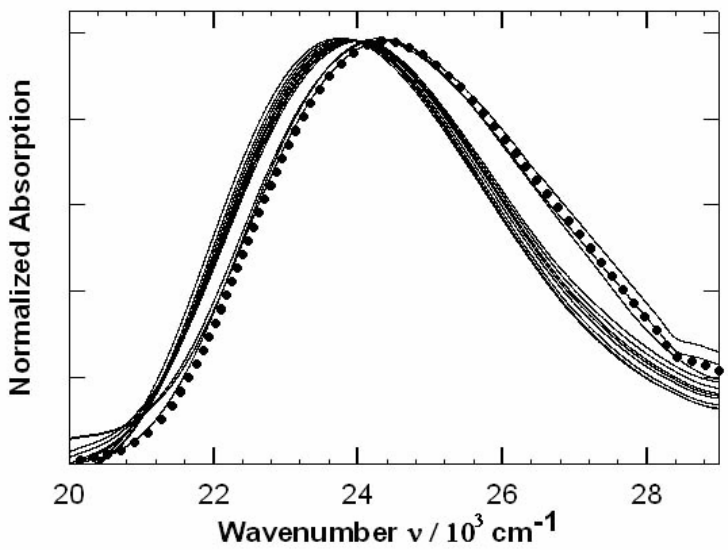

Figure 3.2: C153 absorption spectra in CO_2-expanded MeOH. Left-most spectrum is absorption in neat MeOH, CO_2 concentration increases as the pure CO_2 value is approached (circles).

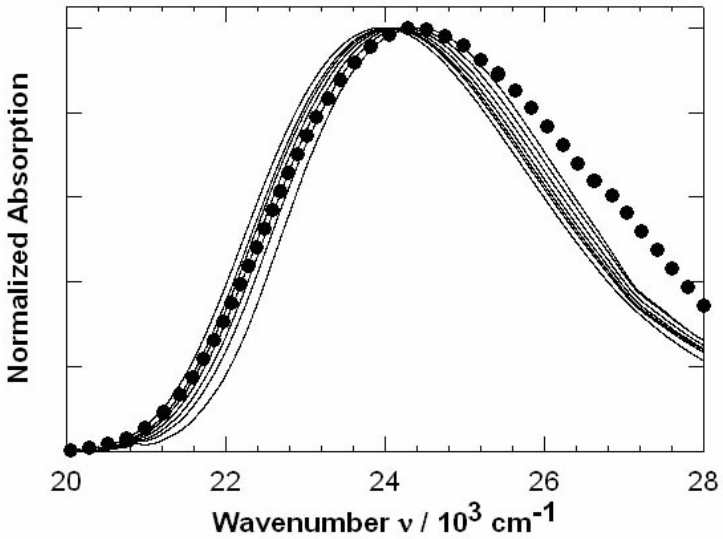

Figure 3.3: C153 absorption spectra in CO_2-expanded acetone.

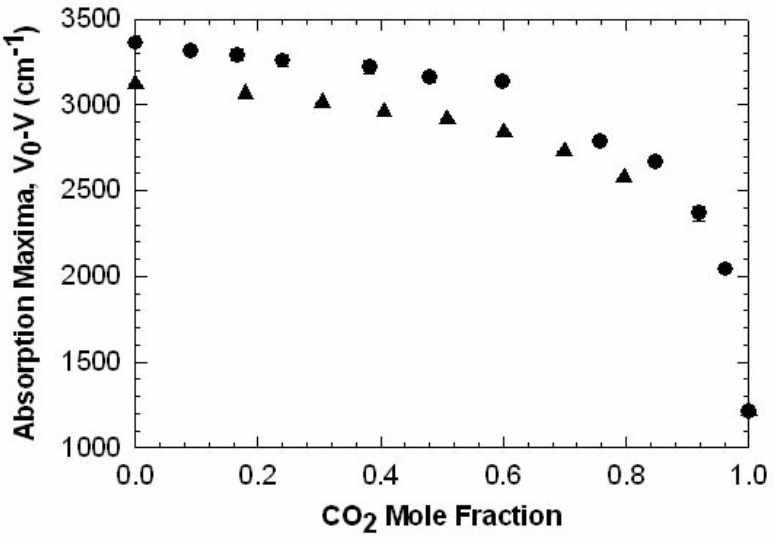

Figure 3.4: Positions of C153 absorption maxima at varying CO_2 concentrations. Wavenumbers have been subtracted from gas-phase absorption values. Circles are CO_2-expanded MeOH maxima, triangles are CO_2-expanded acetone maxima. Error bars are within the size of the data point.

Fluorescence Spectroscopy

Normalized emission spectra in MeOH and acetone GXLs are shown in Figure 3.5 and

Figure 3.6 respectively. Both figures show a large difference between the GXLs and pure CO_2 emission indicating a highly polar solvation mechanism. A plot of the maxima (Figure 3.7) illustrates this point better. The maxima in GXLs are nearly identical to the emission in neat organics, even in GXLs with 97% CO_2 composition! Polar solvents solvate the excited state better, but this observed effect at such low organic concentration is astounding. Also important is the large transition energy difference between MeOH and acetone GXLs, further indicating that polarity is an important criterion in the excited-state solvation process.

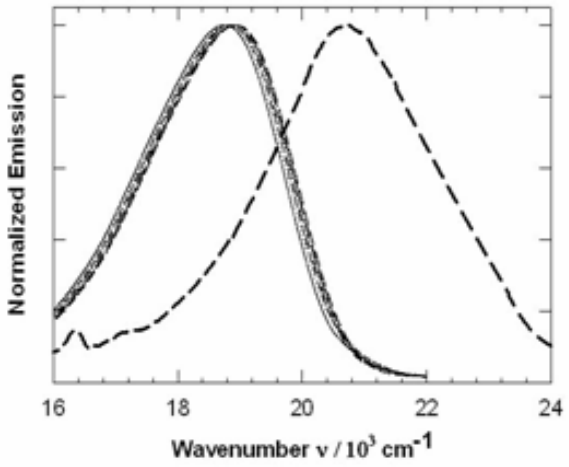

Figure 3.5: C153 emission spectra in CO_2-expanded MeOH. Dashed line is emission in neat CO_2.

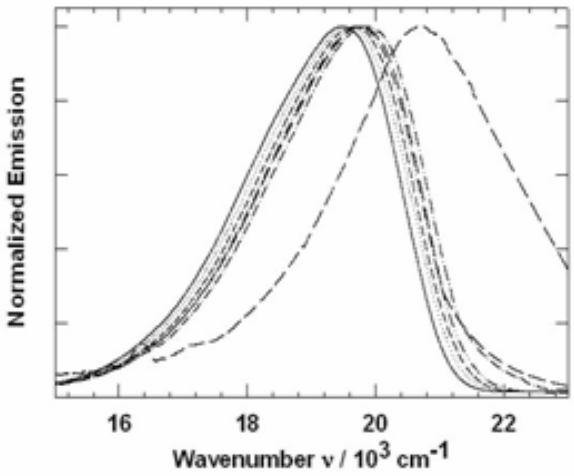

Figure 3.6: Normalized C153 emission spectra in CO_2-expanded acetone.

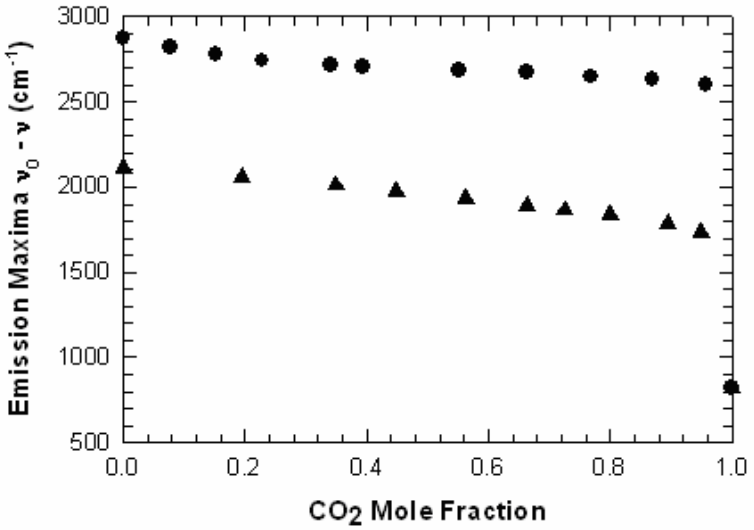

Figure 3.7: C153 emission maxima at varying CO_2 concentrations. Wavenumbers have been subtracted from gas-phase absorption values. Circles represent CO_2-expanded MeOH emission and triangles represent CO_2-expanded acetone emission. Error bars are within size of data points.

MD Simulations

Solvent maps were created from the statistical histograms and the ADF expression of Equation 3.7. C153 has a planar structure that is advantageous for solvent maps because solvation can be explored around the molecule from different 2D perspectives without losing information. Solvent maps for a 5% acetone + CO_2 GXL around the ground-state (S_0) C153 are shown in Figure 3.8 from two different perspectives: a bird's-eye-view to demonstrate solvent accumulation around the C153 perimeter and an in-plane view to highlight solvation above and below the C153 plane. Figure 3.8a and 3.8b are acetone maps while Figure 3.8c and 3.8d are CO_2 maps. Organic and CO_2 maps for all three MeOH GXLs (20%, 5%, and 2% MeOH), and the other two acetone GXLs around both the ground and excited states of C153 are provided in

Appendix A. The scale for the different gray shades represents the magnitude of the ADF. The darker areas of the maps are regions of higher solvent enrichment.

Acetone is more prevalent around the C153 than CO_2, which is consistent with the absorption spectroscopy results; however, MD simulations provide extra details about the solvation mechanisms. Acetone molecules partition near the ester functionality, which is expected because this part of the solute is electron withdrawing and has a large partial charge. There is significant acetone enrichment along the entire perimeter of the solute with some increased enrichment near the nitrogen atom—the electron donating side of C153. On the other hand, CO_2 forms a uniform solvent shell around the probe; but there are enrichments between the carbonyl and trifluoro groups and near the nitrogen, suggesting CO_2 interaction with these functionalities. CO_2 is non-polar, but does have a quadrupolar moment and can interact with free electrons on oxygen and nitrogen atoms and is a known fluorophore. The in-plane views (Figure 3.8b and 3.8d) better highlight the two different solvation mechanisms. Acetone clusters near the electron withdrawing end while CO_2 clusters around the π-cloud above and below C153.

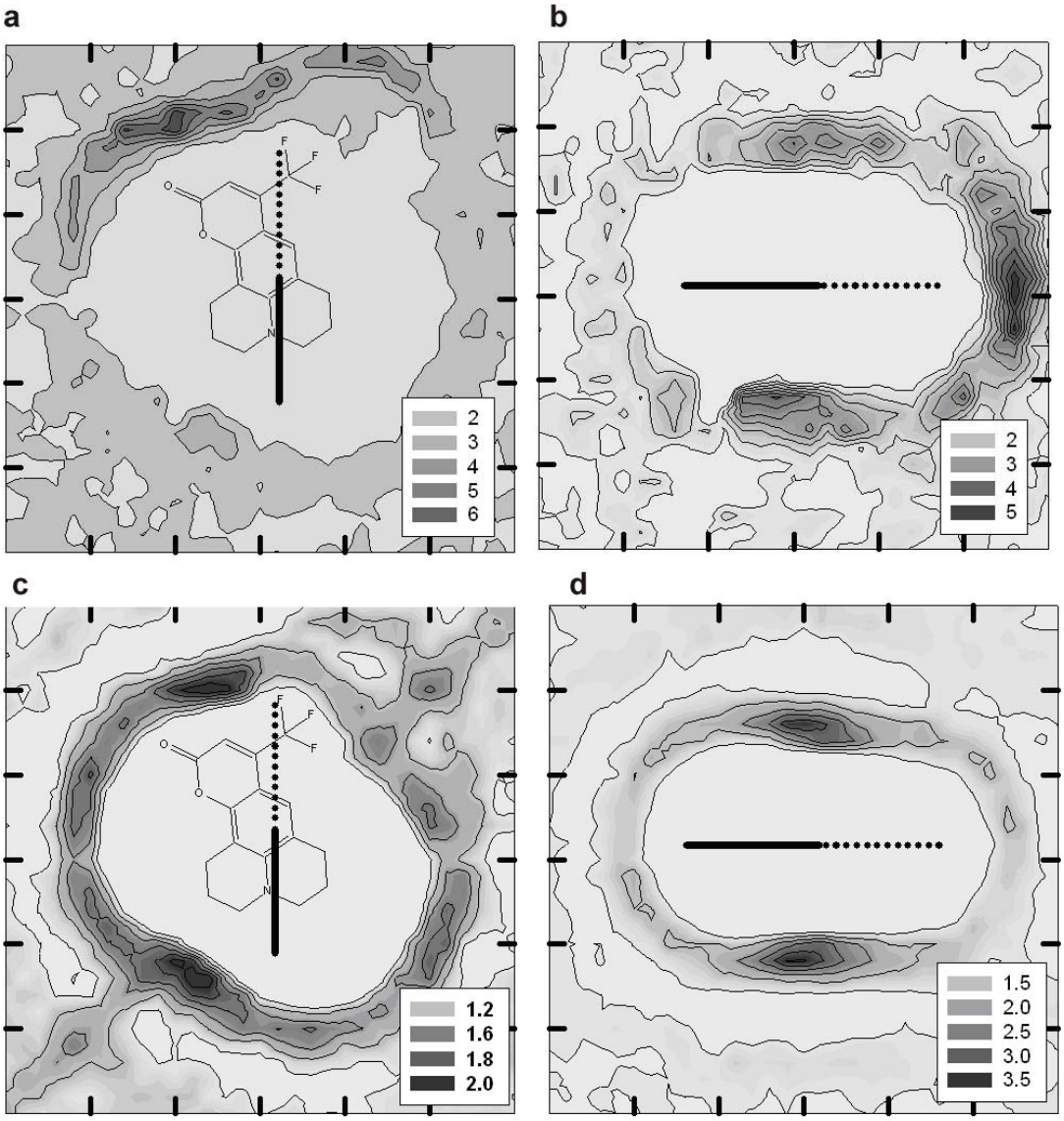

Figure 3.8: Axial distribution functions at two different vantage points around ground-state C153 in a 5% acetone GXL. Scale represents values of the ADF for (a&b) Acetone and (c&d) CO_2 clustering around C153. Depicted plane is coplanar to the C153 molecule (a&c). Vertical line through the probe molecule represents the sample plane used to show solvent accumulation above and below the C153 plane (b&d). The solid and dotted parts of this line are used to differentiate between the two poles of the C153 molecule as the vantage point is rotated. Tick marks are spaced ~3Å.

Ground-state solvation patterns in the other acetone GXLs have similar patterns: acetone favors the electron-withdrawing end of C153 and CO_2 the carbonyl, trifluoro, and amine functional groups. However, the ADF magnitudes of both solvent species increase with added CO_2 because ADF magnitudes are relative to the bulk density, which decreases and thus amplifies the magnitude. Excited-state solvation has two distinct differences from ground-state solvation: The magnitudes of both acetone and CO_2 are much higher and the organic solvation pattern is slightly different. The organic ADFs increase by up to an order of magnitude in a 2% acetone GXL because the C153 dipole moment increases from 7D to 15D and polar solvent better solvate polar solutes. Acetone molecules are in closer proximity to the electron-withdrawing side and greatly increase along the excited dipole moment which is directed from the nitrogen atom to the oxygen atoms.

MeOH has many of the same solvation features as acetone with some exceptions. MeOH accumulates near the electron withdrawing side of C153, but also accumulates along the C153 dipole moment. The solvation pattern near the trifluoro group and carbonyl are similar, but there is little MeOH near the nitrogen atom. CO_2 solvation patterns are essentially the same in acetone and MeOH GXLs, but are of lower magnitude in MeOH GXLs. The increased magnitudes at high bulk CO_2 composition are still seen. C153 excitation effects are more dramatic in MeOH GXLs, where MeOH and CO_2 drastically increase their presence and MeOH changes its solvation pattern, particularly around the trifluoro group and nitrogen atom. MD simulations provide important atomic-level information that is not obtainable by spectroscopic means, and are a direct comparison to spectroscopic experiments in this study. Local compositions were

calculated from solvent accumulation statistics. This serves as a direct comparison to the spectroscopic experiments and shows the effects of solvation on solvatochromic behavior.

Local Compositions from Experiments and Theory

Local compositions were estimated from solvatochromic behavior through a technique developed in this work. ORFT (Equation 3.1) relates local solvent polarity to solvatochromic shift and was used to calculate the expected solvatochromic shift for each bulk CO_2 composition considered in this work. Dielectric constants and refractive indices of each GXL were estimated with Equation 3.2 to Equation 3.5 and parameters A and B in Equation 3.1 were adjusted to match the neat CO_2 and organic experimental maxima. Calculated and experimental solvatochromic shifts in MeOH GXLs are shown in Figure 3.9. For each case the calculated maximum does not match the experimental maximum and is of lower wavenumber. ORFT assumes that the local composition equals the bulk composition; however, spectroscopic responses are based on the solvent environment around the probe. If the probe is in an organic-enriched environment, then the maximum wavenumber will be lower than the bulk wavenumber. The effective micro-environment around C153 is estimated from the differences between experimental and calculated maxima. The solvent composition that gives a calculated maximum equal to the experimental maximum is taken as the local composition in the cybotactic region. The arrows in Figure 3.9 demonstrate this estimation technique.

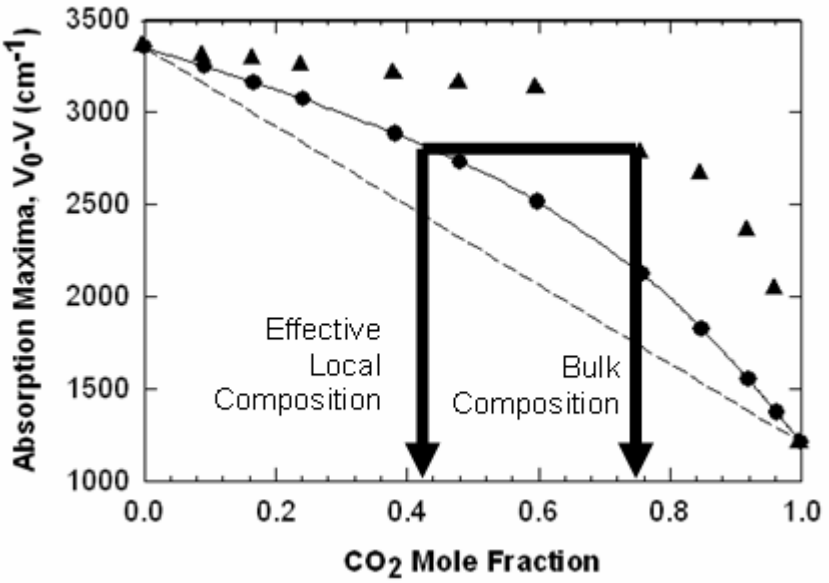

Figure 3.9: Experimental solvatochromic shifts for C153 absorption in CO_2-expanded MeOH (triangles) and calculated solvatochromic shifts from ORFT (circles). Linear local composition approximation (dashed line) is shown for comparison. At identical spectral shift values, the experimental composition is the bulk CO_2 composition while the composition corresponding to calculated shift represents the local or "effective" CO_2 composition in the cybotactic region.

Estimating local compositions from MD simulations depends on the definition of the cybotactic region. The simplest model is a sphere from the C153 center-of-mass that encompasses solvent-enriched areas. Although C153 is a non-spherical molecule, a sphere accounts most of the organic and CO_2 enrichments around the probe. Areas of bulk composition that are encompassed in the sphere do not contribute to the overall cybotactic enrichment. A radius of 7Å surrounded most of the organic and CO_2 enrichments in all GXLs and was used in all cases. The amounts of organic and CO_2 encompassed by the 7Å sphere were recorded and the composition of averaged for 4000 samples per GXL and C153 electronic state. Local compositions for MeOH and acetone

from experiments and simulations are presented in Table 3.2 and Table 3.3. Experimental estimates were interpolated from the actual spectra to match the simulated GXLs.

Table 3.2: Local compositions determined from spectroscopic experiments (interpolated) and MD simulations at each simulated bulk-fluid methanol concentration.

Percent Methanol	State	Experiment	Simulation
20%	S_0	59.5	57.6
5%	S_0	20.4	30.5
2%	S_0	12.0	18.0
20%	S_1	73.7	32.9
5%	S_1	69.8	13.6
2%	S_1	20.0	11.0

Table 3.3: Local compositions determined from spectroscopic experiments (interpolated) and MD simulations at each simulated bulk-fluid acetone concentration.

Percent Acetone	State	Experiment	Simulation
20%	S_0	40.3	36.0
5%	S_0	10.9	5.6
2%	S_0	4.4	2.6
20%	S_1	71.3	26.0
5%	S_1	63.0	10.0
2%	S_1	20.0	8.3

Ground-state experimental and computational local compositions agree very well, particularly at the 20% organic compositions. Excited-state simulations underestimate the experimental values from fluorescence spectroscopy, but do indicate preferential organic solvation in each case. There are several explanations that may cause this phenomenon. The first is CO_2 enhancement around excited-state C153. The solvent maps indicate a substantial increase in organic presence upon excitation, but closer inspection reveals that

the enhancements occur in localized areas around certain functional groups. Another consequence is increased CO_2 presence around the probe. The ADF magnitude is lower than the organic, but is more uniform around the probe. This could dilute the local composition because the estimation technique is based on statistical sampling. Fluorescence is an electronic phenomenon that could be affected by the more polar organic despite local CO_2 enrichment. Another possibility is a shortcoming in the LJ potentials, which were assumed the same in the excited and ground-state simulations. This was suggested by a literature source[30] as a potential problem, and given the short range nature of dipolar interactions could cause erroneous results. Strong specific interactions such as hydrogen bonding between MeOH and C153 that are not explicitly captured in the simulations seem to have little effect the spectroscopy since the simulation/experiment disagreement exists in acetone GXLs, which do not form specific interactions.

Conclusions

Solvation is an important concept for the chemical industry--particularly in solvent and chemical process design. The work presented in this chapter provides an in-depth look into solvation in two GXL systems: MeOH and acetone, and is unique because a combination of spectroscopic experiments and computer simulations was used. This synergistic technique is advantageous over either independent method alone because it provides an atomic-scale look into solvent structure and probes solvent-solute interactions with spectroscopy. Spectroscopy was used to estimate the local solvent composition in the cybotactic region with a simple modeling technique that is versatile and applicable to other solvent systems. Spectroscopic results were used to select which

compositions to simulate. MD simulations served two purposes: 1) to compare directly to local compositions determined from experiment and 2) to provide solvent structures, or solvent maps, around a solute molecule to explore solvation from a molecular scale. The results were very encouraging and suggest that combined computational and experimental studies are a powerful method to study solvation.

UV/Vis and fluorescence spectroscopy predicted reliable local compositions with minimal data and simple modeling techniques. The local compositions around the ground (S_0) state of C153, predicted from UV/vis results, were in good agreement with the MD simulations. Solvation patterns are similar regardless of bulk composition. This result is very promising for future MD studies to explore molecular interactions that are important for studying structure-property relationships for molecular design and solvent selection. Excited-state (S_1) simulations disagreed with fluorescence experiments, but did provide insight into solvation mechanisms and intermolecular interactions that are important in excited-state dynamics, a topic discussed in a subsequent chapter. This study of the cybotactic region and solute-solvent interactions in GXLs provides future researchers with fundamental information for studying and designing complex systems like separation schemes, nanomaterials processing, and homogeneous catalyst recycle and reaction selectivity.

References

1. Horng, M. L.; Gardecki, J. A.; Papazyan, A.; Maroncelli, M., Subpicosecond measurements of polar solvation dynamics: Coumarin 153 revisited. *J. Phys. Chem.* **1995,** 99, (48), 17311-17337.

2. Kumar, P. V.; Maroncelli, M., Polar solvation of polyatomic solutes: Simulation studies in acetonitrile and methanol. *J. Chem. Phys.* **1995,** 103, (8), 3038-3060.

3. Song, W.; Biswas, R.; Maroncelli, M., Intermolecular Interactions and Local Density Augmentation in Supercritical Solvation: A Survey of Simulation and Experimental Results. *J. Phys. Chem. A* **2000,** 104, 6924-6939.

4. Patel, N.; Biswas, R.; Maroncelli, M., Solvation and Friction in Supercritical Fluids: Simulation-Experiment Comparisons in Diphenyl Polyene/CO2 Systems. *J. Phys. Chem. B* **2002,** 106, 7096-7114.

5. Li, H. P.; Arzhantsev, S.; Maroncelli, M., Solvation and solvatochromism in CO2-expanded liquids. 2. Experiment-simulation comparisons of preferential solvation in three prototypical mixtures. *J. Phys. Chem. B* **2007,** 111, (12), 3208-3221.

6. Gohres, J.; Kitchens, C.; Hallett, J.; Popov, A.; Hernandez, R.; Liotta, C.; Eckert, C., A spectroscopic and computational exploration of the cybotactic region of gas-expanded liquids: methanol and acetone. *J. Phys. Chem B* **2008,** 112, 4666-4673.

7. Gohres, J. L.; Hernandez, R.; Liotta, C. L.; Eckert, C. A., Viewing the cybotactic structure of gas-expanded liquids. In *Green Chemistry and Engineering with Gas Expanded Liquids and Near-critical Media. ACS Symposium Series Volume;*, Hutchenson, K. W.; Scurto, A. M.; Subramaniam, B., Eds. Oxford University Press: Oxford, 2008 (In Press).

8. Shukla, C. L.; Hallett, J. P.; Popov, A. V.; Hernandez, R.; Liotta, C. L.; Eckert, C. A., Molecular dynamics simulation of the cybotactic region in gas-expanded methanol- carbon dioxide and acetone-carbon dioxide mixtures. *J. Phys. Chem. B* **2006,** 110, (47), 24101-24111.

9. Li, H. P.; Maroncelli, M., Solvation and solvatochromism in CO2-expanded liquids. 1. Simulations of the solvent systems CO2+cyclohexane, acetonitrile, and methanol. *J. Phys. Chem. B* **2006,** 110, (42), 21189-21197.

10. Eckert, C. A.; Ziger, D. H.; Johnston, K. P.; Kim, S., Solute partial molal volumes in supercritical fluids. *J. Phys. Chem.* **1986,** 90, (12), 2738-2746.

11. Onsager, L., Electric Moments of Molecules in Liquids. *J. Am. Chem. Soc.* **1936,** 58, 1486-1493.

12. Hadrich, J., Lorentz-Lorenz Function of 5 Gaseous and Liquid Saturated-Hydrocarbons. *Appl. Phys.* **1975,** 7, 209-213.

13. Tasic, A. Z.; Djordjevic, B. D.; Grozdanic, D. K.; Radojkovic, N., Use of Mixing Rules in Predicting Refractive-Indexes and Specific Refractivities for Some Binary-Liquid Mixtures. *J. Chem. Eng. Data* **1992,** 37, (3), 310-313.

14. Sun, Y. D.; Shekunov, B. Y.; York, P., Refractive index of supercritical CO2-ethanol solvents. *Chem. Eng. Comm.* **2003,** 190, (1), 1-14.

15. Kitchens, C. L.; Roberts, C. B., Copper nanoparticle synthesis in compressed liquid and supercritical fluid reverse micelle systems. *Ind. Eng. Chem. Res.* **2004,** 43, (19), 6070-6081.

16. Buckingham, A. D.; Pople, J. A., A Theory of Magnetic Double Refration. *Proceedings of the Physical Society of London Section B* **1956,** 69, (11), 1133-1138.

17. Besserer, G. J.; Robinson, D. B., Refractive Indices of Ethane, Carbon-Dioxide, and Isobutane. *J. Chem. Eng. Data* **1973,** 18, (2), 137-140.

18. Lide, D. R., *Handbook of Organic Solvents*. CRC: Boca Raton, FL, 1995.

19. Lou, J. F.; Paravastu, A. K.; Laibinis, P. E.; Hatton, T. A., Effect of temperature on the dielectric relaxation in solvent mixtures at microwave frequencies. *J. Phys. Chem. A* **1997,** 101, (51), 9892-9899.

20. Bruggeman, D. A. G., *Ann. Phys.* **1935,** 24, (636-644), 636.

21. Roskar, V.; Dombro, R. A.; Prentice, G. A.; Westgate, C. R.; McHugh, M. A., Comparison of the dielectric behavior of mixtures of methanol with CO2 and ethane in the mixture-critical and liquid regions. *Fluid Phase Equilib.* **1991,** 77, 241-259.

22. Weikel, R. R.; Hallett, J. P.; Liotta, C. L.; Eckert, C. A., Self-neutralizing in situ acid catalysts from CO2. *Topics in Catalysis* **2006,** 37, (2-4), 75-80.

23. Potoff, J. J.; Siepmann, J. I., Vapor-liquid equilibria of mixtures containing alkanes, carbon dioxide, and nitrogen. *Aiche J.* **2001,** 47, (7), 1676-1682.

24. Jorgensen, W. L., Optimized intermolecular potential functions for liquid alcohols. *J. Phys. Chem.* **1986,** 90, (7), 1276-1284.

25. Jorgensen, W. L.; Briggs, J. M.; Contreras, M. L., Relative partition-coefficients for organic solutes from fluid simulations. *J. Phys. Chem.* **1990,** 94, (4), 1683-1686.

26. Pranata, J.; Wierschke, S. G.; Jorgensen, W. L., OPLS potential functions for nucleotide bases - relative association constants of hydrogen-bonded base-pairs in chloroform. *J. Am. Chem. Soc.* **1991,** 113, (8), 2810-2819.

27. Smith, W.; Forester, T. R., DL_POLY_2.0: A general-purpose parallel molecular dynamics simulation package. *J. Molecular Graphics* **1996,** 14, (3), 136-141.

28. Patel, N. C.; Teja, A. S., A new cubic equation of state for fluids and fluid mixtures. *Chem. Eng. Sci.* **1982,** 37, (3), 463-473.

29. Allen, M. P.; Tildesley, D. J., Computer Simulations of Liquids. In Oxford University Press: Oxford, 1987.

30. Cichos, F.; Brown, R.; Bopp, P. A., Coupled molecular dynamics/semiempirical simulation of organic solutes in polar liquids. II. Coumarin 153 in methanol and acetonitrile. *J. Chem. Phys.* **2001,** 114, (15), 6834-6842.

CHAPTER 4: SOLVENT AND SOLVATION DYNAMICS IN GAS-EXPANDED LIQUIDS

Introduction

The solvent maps presented in Chapter 3 and Appendix A reveal different solvation patterns between the ground and excited states of C153. Excited states have organic and CO_2 density enhancements in the cybotactic region relative to the ground state that indicate a solvent response upon C153 excitation. The excited-state organic and CO_2 solvation patterns are also different than their respective ground-state patterns. Electronic reorganization of C153 takes ~1fs; however, the solvent response is much slower (several ps). The speed and duration of the solvent reorganization depends on solvent properties. Knowledge of solvent reorganization behavior in various GXLs provides insight into solvation mechanisms and the ability to tune the solvent response to electronic perturbations. In this chapter MD simulations were used to determine solvation response times in MeOH and acetone GXLs and explore how solvent rotations contribute to the solvent response time. This project is an extension to the steady-state solvation work presented in Chapter 3 and adds a dynamic perspective to the behavior reported therein.

Solvation dynamics affect ultrafast chemical processes like electron transfer reactions and free radical chemistries.[1, 2] Consequently, many spectroscopic,[3] computational,[4] and theoretical studies[5] have been performed in a variety of media, including tunable solvents like SCFs.[6-9] Solvent selection is an important consideration in these processes because solvation of a newly formed radical or electronically perturbed

species may impact or facilitate a process. This effect has been demonstrated in free radical polymerizations[10] where polar solvents solvate a free radical species and allow the reaction to proceed, whereas non-polar solvents lead to precipitation of the free radical species. Another application is molecular wire design and application that involve electron tunneling through a donor-bridge-acceptor dyad upon exposure to stimuli like light or an electric field. Electron transfer through the dyad is strongly coupled to the solvent environment and its ability to reorganize around the dyad. Solvents impact electron tunneling and ultimately affect device performance and optical properties.[11-13]

Solvation timescales in SCFs are often long compared to organic solvents, and solvation cannot respond to electronic perturbations within a reasonable time for many charge-transfer processes. Despite their versatile tunable properties, SCFs respond too slowly for the aforementioned applications. GXLs are attractive for these applications because they combine the tunable solvation properties of SCFs with the fast solvation dynamics of liquid organics. This allows *in situ* control over device performance, reaction rates, and selectivity at competitive solvation rates. Their use as solvents in these processes requires knowledge of solvation timescales and the solvent motions that make up the response.

Computational Methods

All simulations were run in DL_POLY v2.0[14] with a Verlet leapfrog algorithm to integrate the equations of motion. All molecules were treated as rigid bodies with a Lennard-Jones plus Coulombic interactions force field. C153 was modeled with an OPLS-AA force field[15] and partial charges taken from Kumar and Maroncelli.[4] MeOH and acetone used J2[16] and OPLS[17] force fields respectively and CO_2 the TraPPE

potential.[18] Site-site interactions are determined by the Lorentz-Berthelot combining rules: $\sigma_{12} = 0.5(\sigma_1 + \sigma_2)$ and $\varepsilon_{12} = (\varepsilon_1\varepsilon_2)^{0.5}$. Simulations are of the liquid phases at the bubble point, which eliminates interfacial effects on the solvent dynamics. Initial configurations for the solvation dynamics simulations were set up by running a 200ps equilibrium simulation in the NVT ensemble with a relaxation time of 1ps. The timestep was 3fs and the temperature 300K with Nose-Hoover thermostat. The initial configuration was a randomly-distributed periodic box of 500 solvent molecules (600 for 98% CO_2 GXLs) and a single C153 in the ground state. The box size was scaled to match the liquid-phase volumes as predicted by the Patel-Teja equation of state.[19] Long NVT simulations were run with coordinates saved every 6ps for solvation dynamics inputs. Solvation dynamics were run in the NVE ensemble after changing the C153 partial charges to the S_1 excited-state. Simulations were ~5ps due to the relatively short reorganization timescales. Coordinates were saved every 45fs and analyzed in an external FORTRAN program.

Solvation dynamics are quantified by the solvent response function (SRF) shown in Equation 4.1. The SRF is a normalized function of the energy gap between the C153 electronic states and is a measure of total solvent-solute interaction energy between the electronic states.

$$S(t) = \frac{\Delta E(t) - \Delta E(\infty)}{\Delta E(0) - \Delta E(\infty)} \qquad \text{Equation 4.1}$$

where ΔE(t) is the energy gap between the C153 electronic states and S(t) is the SRF. For simplicity the C153 Lennard-Jones parameters were the same in the ground and excited

states. Therefore, electrostatic differences between the solvent and solute compose the energy gap as described in Equation 4.2

$$\Delta E = \frac{1}{4\pi\varepsilon_0}\sum_{i}^{N}\sum_{\alpha}\sum_{\beta}\frac{\Delta q_\alpha q_{i\beta}}{r_{\alpha,i\beta}} \qquad \text{Equation 4.2}$$

where ε_0 is the relative permittivity in vacuum, N is the number if solvent molecules, α denotes a solute atom, β denotes a solvent atom on molecule i. Terms $q_{i\beta}$ and Δq_α are respectively the partial charge on solvent atom β and difference in partial charge between ground and excited state on C153 atom α. Equation 4.1 is cumbersome and requires many trajectories to obtain a representative sample. A convenient substitution for Equation 4.1 is to use a time correlation function to approximate the solvent response:

$$C(t) \sim S(t) = \frac{\langle \delta\Delta E(0)\delta\Delta E(t)\rangle}{\langle (\delta\Delta E)^2\rangle} \qquad \text{Equation 4.3}$$

This linear response approximation assumes that the non-linear response is described by fluctuation around the average energy, i.e. $\delta E(t) = \Delta E(t) - \langle \Delta E \rangle$. If this is reasonable, then equilibrium simulations can be run instead of non-equilibrium simulations. Equation 4.3 describes neat liquid systems adequately, but breaks down in systems like SCFs and GXLs where preferential solvation and/or local density enhancements occur. C153 excitation increases organic and CO_2 density around the probe (relative to the ground-state), which breaks down the linear response assumption since solvation changes are no longer described by normal fluctuations. Although this increases the computational demand, it allows computation of solvent rotational correlation functions that can dominate the solvation process.

Solvation is a complex process involving both electronic and nuclear rearrangements; each has a unique solvent-dependent timescale. Electronic reorganizations, from solvent polarization, are very fast (fs timescale) and were not considered in this work to save on computational time. Polarization slows down the response in neat MeOH,[20] but becomes less significant as the medium becomes non-polar. Solvent rotations and translation occur on ps timescales and have the largest impact on the response time. Rotations were studied in great detail, although results presented in Chapter 3 suggest that solvent diffusion into the cybotactic region contributes to the solvent response. Previous investigations[21] of MeOH and acetone diffusion in their respective GXLs showed that diffusion is dependent on CO_2 composition, and acetone diffusion is faster then MeOH diffusion at all identical CO_2 mole fractions. MeOH was expected to diffuse faster because the molecules are smaller and lighter than acetone, but strong MeOH-MeOH interactions inhibit rapid diffusion. C153 motions are slow compared to solvent molecules because of the large size and thus do not contribute to solvation.

Results and Discussion

Solvation Dynamics

SRFs of acetone GXLs and MeOH GXLs (including neat organics) are presented in Figure 4.1 and Figure 4.2 respectively. The results represent averages of over 1000 trajectories per CO_2 composition calculated via Equation 4.1 and fitted with exponential decay functions of the following form:

$$S(t) = \sum_{i=1}^{k} a_i \exp(-t/\tau_i) \qquad \text{Equation 4.4}$$

where k is the number of exponential decay terms considered, a_i is a pre-exponential fitting parameters, and τ_i and is a characteristic timescale that indicates the duration of a solvation event. Pre-exponential factors indicate the relative contribution of the different solvation events to the overall solvation process. All SRFs were fit with a bi-exponential decay function with a standard error less than 4% and fitting parameters for MeOH and acetone GXLs are shown in Table 4.1. An interesting feature in both neat solvents is the rapid initial response that composes ~70-90% of the solvation process. The initial decay lasts only ~100fs and is followed by a slow relaxation to equilibrium that lasts up to 13ps in the slowest case. In both classes of GXLs, the initial decay in the neat organic liquid is the fastest; however, the long term relaxation is faster in the 60% and 80% CO_2 GXLs. This behavior suggests that two competing solvent characteristics determine solvation timescales: polarity and viscosity. Polar solvents respond to electronic perturbation and can rearrange dipoles with a solute's dipole to solvate the molecule. Complete solvation is determined by transport of additional solvent molecules into the cybotactic region to stabilize the highly charge separated excited state. This was seen in Chapter 3 where the organic and CO_2 density around the C153 excited state increased relative to the ground state. Consequently decreased solvent viscosity facilitates solvent enrichment and can increase solvation response if the appropriate solvent polarity is present.

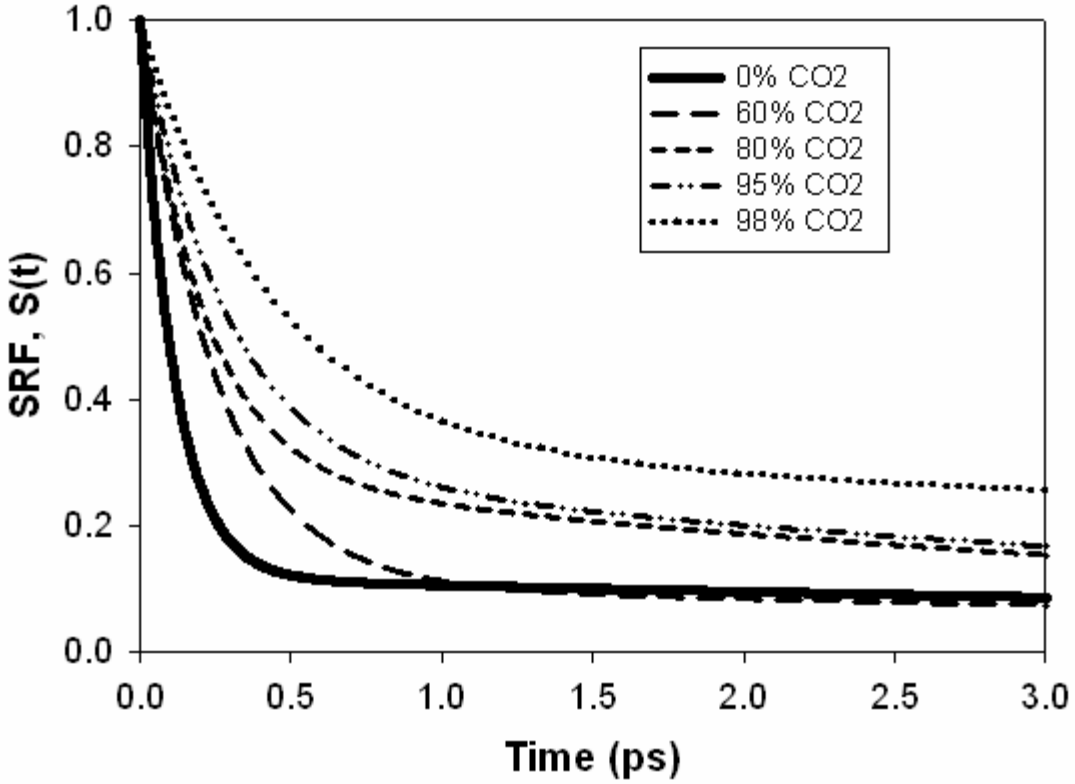

Figure 4.1: Acetone and CO_2-expanded acetone SRFs at varying CO_2 composition.

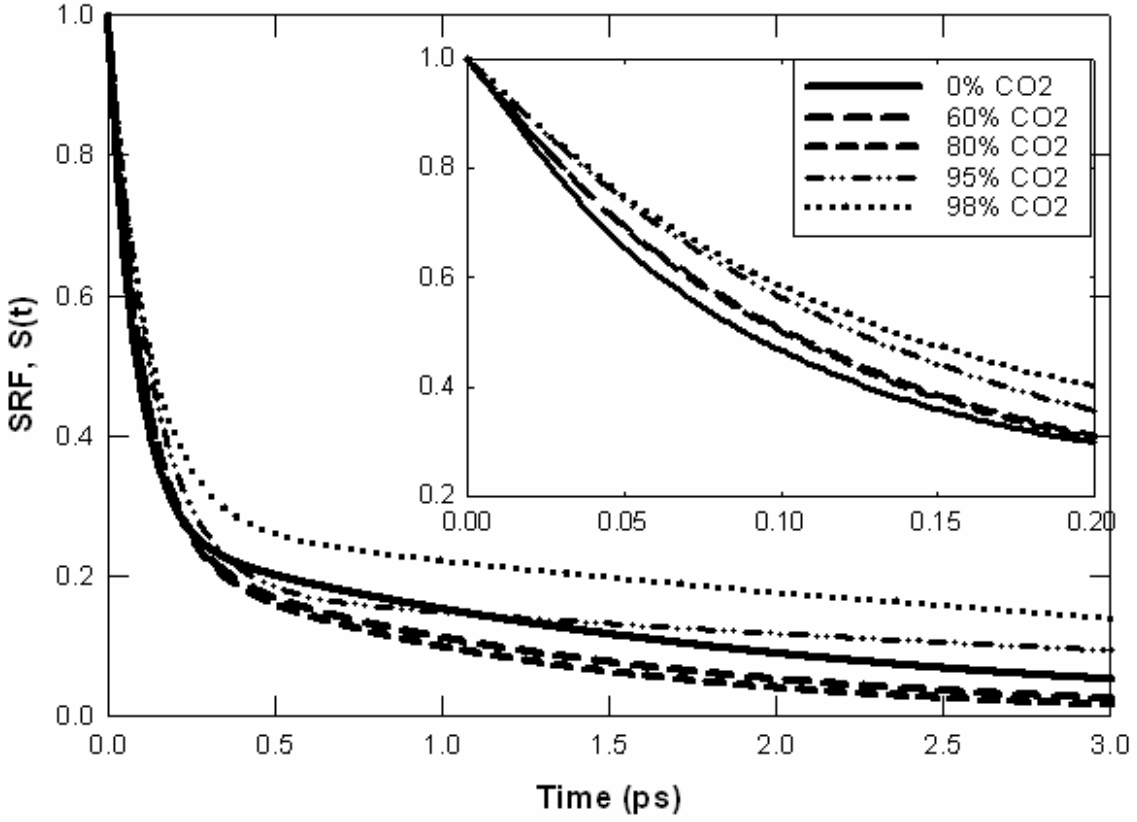

Figure 4.2: MeOH & CO_2-expanded MeOH SRFs at different CO_2 compositions. Inset is an expanded view of the initial solvation responses.

Table 4.1: Parameters used to fit Equation 4.4 to SRF data.

% CO_2	**a_1**	**τ_1 (ps)**	**a_2**	**τ_2(ps)**
Neat Acetone	0.883	0.112	0.117	10.0
60%	0.892	0.253	0.108	8.147
80%	0.722	0.216	0.278	5.074
95%	0.715	0.288	0.285	5.66
98%	0.681	0.44	0.319	13.77
% CO_2	**a_1**	**τ_1 (ps)**	**a_2**	**τ_2(ps)**
Neat MeOH	0.739	0.082	0.261	1.874
60%	0.763	0.102	0.237	1.338
80%	0.759	0.10	0.241	1.126
95%	0.815	0.132	0.185	4.443
98%	0.72	0.119	0.28	4.358

Solvation times quantify the total solvent response time and provide a comparison between the different solvents. These are found by integrating the solvation response function:

$$\langle \tau_S \rangle = \int_0^\infty S(t)dt \qquad \text{Equation 4.5}$$

where τ_s is the solvation time and the brackets denote that it is an average value. Solvation times in both types of GXLs are shown in Figure 4.3 as a function of CO_2 composition. Both acetone and MeOH GXLs have a minimum solvation time under GXL conditions (instead of the neat organic liquid) because there are two competing mechanisms: polarity and viscosity effects. The maximum rate in acetone is much more significant than the maximum rate in MeOH; however, other important features are apparent and unique to the co-solvent. Solvation times vary little between neat organic liquids and 80% CO_2 GXLs. Most of the tunability occurs at high CO_2 composition. Similar behavior was seen in Chapter 3 where the absorption maxima closely resemble the maxima in neat acetone or MeOH at compositions up to 80% CO_2. After this composition there is a sharp decrease to the absorbance maximum in liquid CO_2. The absorption spectra and solvation rates are the result of preferential organic solvation. Beyond 80% CO_2 the local solvent environment becomes significantly less polar, and the absorbance maxima approach the pure CO_2 maximum. In solvation dynamics, the transport rates are much higher in this composition range, but the polar molecules are dispersed in the bulk fluid and require more time to diffuse into the cybotactic region. GXLs with very high CO_2 concentration have an insufficient amount of the polar species and must rely on local CO_2 density enhancements to solvate the excited C153 molecule.

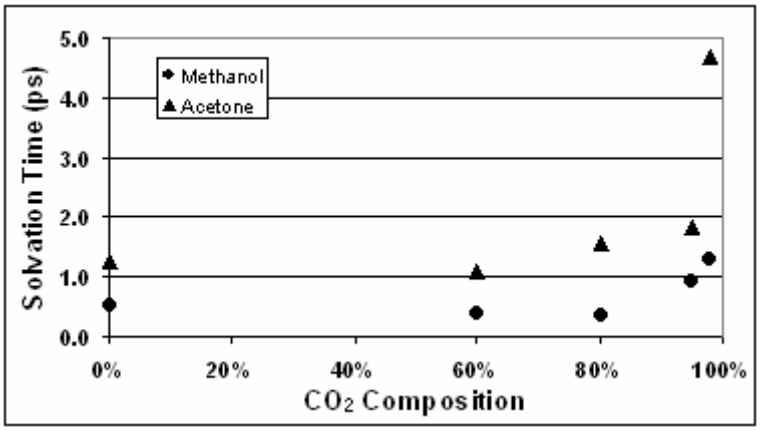

Figure 4.3: Solvation times in CO_2-expanded MeOH and Acetone.

The neat MeOH solvation time is much faster than experimental results,[22] but it agrees reasonably well with MD simulation results from other researchers,[4, 20] although these studies used different cases of MD simulations. Kumar and Maroncelli[4] used a fixed C153 molecule and the linear time-correlation approximation of Equation 4.3 in their analysis. Cichos et al[20] used a similar approach, but added a non-equilibrium case with polarizability. Polarizable force fields slow down the solvent response and provide better agreement with the experimental findings. SRFs in neat acetone are in better agreement with experimental data[22] than those in neat MeOH, but this result is slightly slower than the experimental data.

Solvent Rotations

Rotational dynamics were investigated with first and second order rotational correlation functions (RCFs) shown in Equation 4.6 and Equation 4.7 respectively:

$$C_1(t) = \langle \vec{n}(t) \cdot \vec{n}(0) \rangle \qquad \text{Equation 4.6}$$

$$C_2(t) = \frac{\left\langle 3[\vec{n}(t)\cdot\vec{n}(0)]^2 - 1 \right\rangle}{2}$$ Equation 4.7

where $C_i(t)$ is the RCF of rank *i*, and $\vec{n}$ is a characteristic molecular vector. CO_2 is a linear molecule with one characteristic vector from the carbon atom to one of the oxygen atoms. MeOH is a small molecule so one axis of rotation is sufficient to describe rotation--the bond vector directed from the MeOH oxygen and protic hydrogen. This rotation is more likely to contribute to the solvation response than the oxygen methyl vector since the polar hydroxyl group contributes more to the dipole moment and thus the rotations. Two bond vectors were used for acetone because it is a bulky molecule with at least two axes of rotation. One vector extends along the carbonyl group from the carbon to the oxygen and the other is directed from the carbonyl carbon to a methyl group. First-order RCFs indicate the time a molecule takes to lose its orientation while second-order RCFs indicate the timescale to lose the molecule's alignment. First-order RCFs are 2-3 times slower than second-order RCFs. Molecules in this system range from very fast rotors like CO_2 to relatively slow rotors like MeOH.

RCFs of solvent molecules are considered in three classifications: 1) those that take place immediately after C153 excitation 2) solvent molecules that are in the cybotactic region of C153 and 3) solvent rotations that occur in the bulk fluid, i.e. no C153. The three cases will be referred to as SRF, Cybo, and Bulk respectively. This distinguishes bulk solvent rotations that occur from normal fluctuations from solvent rotations affected by C153 excitation. The cybotactic region is a dynamic area that constantly changes location as the solute and solvent molecules diffuse, so assumptions were made to study this transient region. The same definition was used as was described

in Chapter 3. Briefly, a sphere of 7A was drawn outwards from the C153 center of mass. Any solvent molecules that were initially in this sphere were considered part of the cybotactic region throughout the entire simulation. C153 diffusion is very slow and most solvent rotations occur before diffusive escape from the region. Solvent molecules that entered the sphere mid-simulation were not considered a part of the cybotactic region for simplification purposes.

Second-order RCFs for acetone (along the C-O bond) and MeOH GXLs, SRF case, are shown in Figure 4.4 and Figure 4.5. These figures illustrate the faster rotations from CO_2 addition which gives the solvent gas-like properties and thus facilitates rotation. There are several apparent features in these figures that are common throughout all cases considered: 1) multiple timescales, a rapid initial decay followed by a long-term decay 2) a large rate increase between 80% CO_2 and 95% CO_2. In addition there are two distinguishing features between acetone and MeOH RCFs: 1) initial acetone rotations are nearly identical between all GXLs and neat acetone. This is seen by the overlap of RCFs until 0.3ps when divergence begins. 2) Acetone rotations are faster than MeOH. All acetone RCFs are uncorrelated within 2ps while MeOH RCFs range from 2ps to 9ps. CO_2 RCFs (SRF case) in acetone and MeOH GXLs are shown in Figure 4.6 and Figure 4.7 respectively. CO_2 molecules rotate faster than both organic species in the same solvent and are less sensitive to bulk composition, although rotations are faster when more CO_2 is present. CO_2 has an initial lag period during the first 0.1ps that is not present in the organic RCFs. CO_2 could be initially unresponsive because weak intermolecular interactions prevent an initial thrust to start rotation.

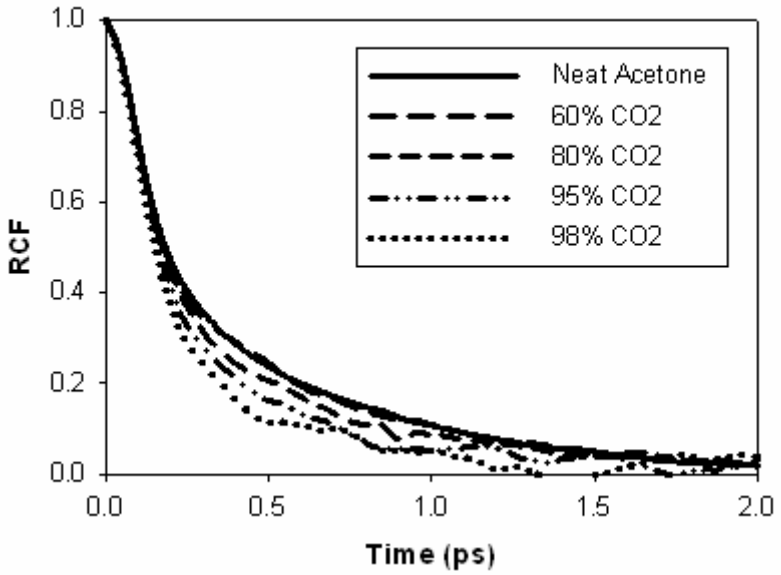

Figure 4.4: Second-order acetone rotational correlation functions in acetone and acetone GXLs after C153 excitation.

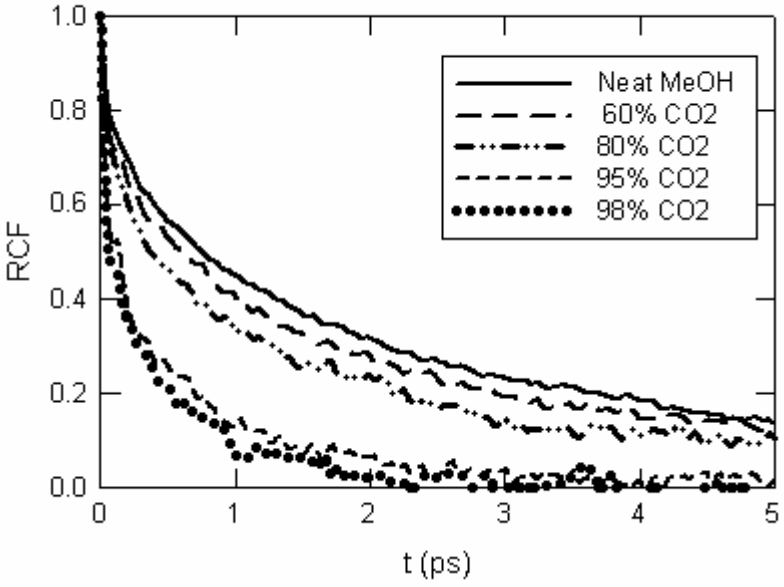

Figure 4.5: Second-order MeOH rotational correlation functions in different MeOH GXLs after C153 excitation.

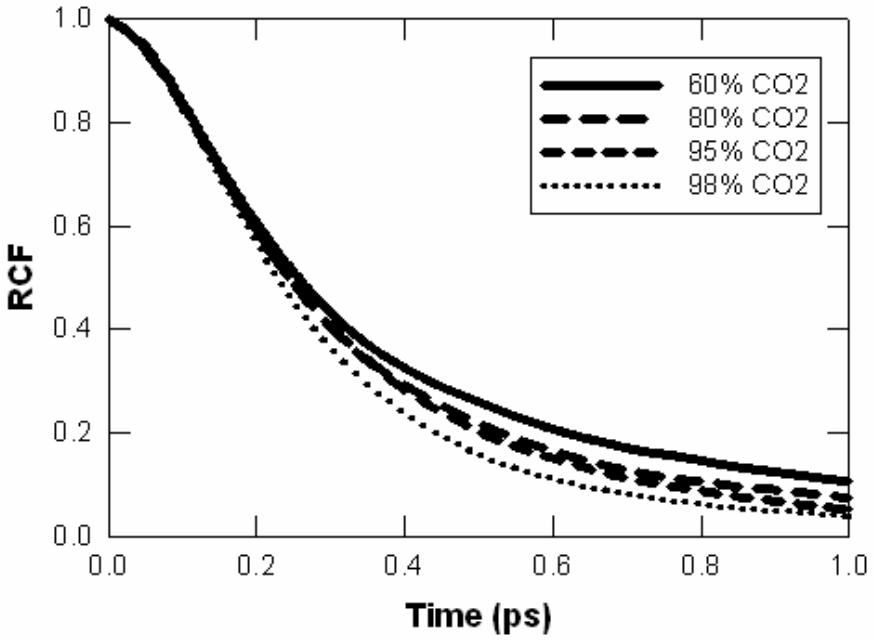

Figure 4.6: Second-order CO_2 rotational correlation functions in several acetone GXLs for the SRF case.

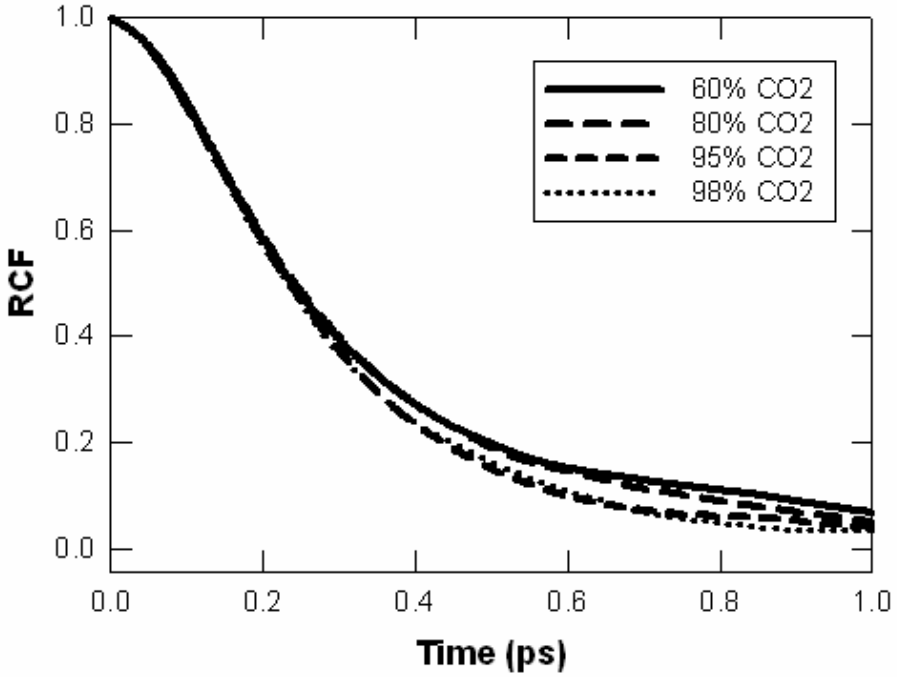

Figure 4.7: Second-order CO_2 rotational correlation functions in several MeOH GXLs for the SRF case.

RCFs were fit with exponential decay functions of Equation 4.4. Most organic RCFs were fit with bi-exponential decay functions, although second-order MeOH RCFs were fit with tri-exponential decay functions, and all CO_2 RCFs were with exponential decay functions. All fits had a standard error less than 2%, but most were less than 1%. RCF fitting parameters for bulk, SRF, and cybo cases for CO_2 and organic RCFs in are presented in Appendix B. The general trend for solvation times for GXLs with the same bulk solvent composition is: Bulk < SRF < Cybo. This trend shows that C153 effects solvent rotation. Two possible scenarios account for this behavior:

1) Charge redistribution on C153 increases electrostatic interactions with nearby solvent molecules and hinders their ability to rotate.
2) Solvent molecules become aligned with C153 and thus trapped in a minimum energy state.

Solute-solvent interactions are different than solvent-solvent interactions and can change solvent dynamics. Strong electrostatic and dipolar interactions with C153 disrupt bulk-like rotations. Solvation occurs as molecules realign with the newly formed C153 dipole moment, and molecules within the cybotactic region will align with nearby functional groups on C153. If a molecule becomes perfectly aligned with a bond vector of the solute, its rotations will be halted. Both arguments fit; however, the first could accelerate rotations if solute-solvent forces are repulsive instead of attractive. Examination of the fitting parameters in Appendix B shows that the initial rotations are similar in all three cases and most discrepancy occurs at longer timescales. This could indicate that a solvent molecule has become trapped in a stable alignment with C153.

Acetone rotation along the C-O bond vector is initially independent of composition, although the relative contributions (denoted by the pre-factor) change significantly with CO_2 composition. This is evident in Figure 4.4 where the initial rate of decay is identical in each GXL, and most variations occurred after 0.5ps. Acetone rotation along the C-Me vector has initial timescales that are an order-of-magnitude faster than initial rotations along the C-O vector. Longer timescales are faster than the C-O case, and the fitting parameters exhibit less variation between GXLs. This behavior shows the heterogeneous nature of acetone rotations, suggesting that the C-Me axes are the preferred axes of rotation.

First-order MeOH RCFs behave similarly to the acetone RCFs where the initial timescales vary little between GXLs and the pre-factors increase with CO_2 composition. The longer timescales become significantly shorter with more CO_2, but contribute less to the overall rotation timescale. Second-order RCFs were fit with a tri-exponential decay function because there is a very fast initial response followed by two distinct and significant rotational times. The initial response time and contribution is very composition-dependent and most significant at higher CO_2 compositions. Long timescales decrease with increased CO_2 composition over the entire range, which indicates that MeOH-MeOH interactions do not inhibit MeOH rotation at first, but become significant and hinder rotation after this brief first period. As more CO_2 is added, MeOH-MeOH hydrogen bonds are less prevalent and MeOH rotates more freely.

Solvent rotations give additional insights into the solvation behavior in GXLs and the underlying molecular interactions that affect solvation. MeOH rotations are slower than the solvation timescales in neat MeOH and 60% and 80% GXLs because of strong

MeOH-MeOH hydrogen bonds. Solvation in these solvents is a function of MeOH diffusion into the cybotactic region. At very high CO_2 compositions (>95%) the rotational rates become comparable to solvation rates. In this regime the hydrogen bonding is less pronounced and solvation is due primarily to solvent rotation and diffusion in the cybotactic region. CO_2 rotations are comparable to solvation timescales, but the non-polar properties of CO_2 limit its contribution to solvation. Acetone rotations are less affected by composition and rotations around both axes in neat organic and low-pressure GXLs are comparable to the solvation timescale. Rotations are much faster in high-CO_2 GXLs, so acetone diffusion into the cybotactic region determines the solvation time. The different rotational speeds about both acetone rotational axes indicate that the C-Me bond are the preferred axes rotation.

Conclusion

A solvent's response to electronic perturbations like ion or radical formation and electronic restructuring impacts ultrafast processes like electron transfer reactions, radical polymerizations, and ligand coordination for homogenous catalysis. GXLs are a versatile medium for these types of processes because the response time can be altered by changing the co-solvent or manipulating the composition *in situ*. The solvation dynamics in CO_2-expanded MeOH and acetone exhibit behaviors that are consistent with the steady-state solvation study presented in Chapter 3. A key finding from that study was preferential organic solvation at CO_2 compositions up to 80%. The dynamic solvent behavior shows similar trends where the solvation timescale is nearly the same as the neat organic timescale. Solvation is a multi-step process that is affected by preferential

solvation. The first step is rotation by polar solvent molecules to realign their dipole moments with the excited-state solute dipole moment. Rotations are responsible for the rapid initial decay while bulk transport into the cybotactic region dictates the long-time decay. Rotations were considered in great detail with correlation functions; however, bulk diffusion was not, as it is well-known in GXLs.[21]

Organic and CO_2 rotations are dependent on the bulk composition and organic rotations behave like the neat liquid system up to 80% CO_2. This behavior is due to strong solvent-solvent interactions that hinder rotation. Beyond this composition, intermolecular interactions are weakened and the organic molecules can rotate faster. Solvent rotations within the cybotactic region are slower than bulk rotations, indicating that rotation, and ultimately the solvation timescale are dependent upon solvent polarity, molecular interactions, and viscosity. This study of solvent and solvation dynamics demonstrates the tunable properties of GXLs and links molecular scale properties like solvation timescales, molecular motion, and interactions to bulk solvent composition. With this information, electron transfer reactions, nanowire performance, and polymerizations can be tuned to fit the needs of the application.

References

1. Maroncelli, M.; Macinnis, J.; Fleming, G. R., Polar-solvent dynamics and electron-transfer reactions. *Science* **1989,** 243, (4899), 1674-1681.

2. Rossky, P. J.; Simon, J. D., Dynamics of Chemical Processes in Polar-Solvents. *Nature* **1994,** 370, (6487), 263-269.

3. Carter, E. A.; Hynes, J. T., Solvation Dynamics For An Ion-Pair In A Polar-Solvent - Time-Dependent Fluorescence And Photochemical Charge-Transfer. *J. Chem. Phys.* **1991,** 94, (9), 5961-5979.

4. Kumar, P. V.; Maroncelli, M., Polar solvation of polyatomic solutes: Simulation studies in acetonitrile and methanol. *J. Chem. Phys.* **1995,** 103, (8), 3038-3060.

5. Agmon, N., The dynamics of preferential solvation. *J. Phys. Chem. A* **2002,** 106, (32), 7256-7260.

6. Ladanyi, B. M.; Nugent, S., The effects of solute-solvent electrostatic interactions on solvation dynamics in supercritical CO2. *J. Chem. Phys.* **2006,** 124, (4).

7. Egorov, S. A., Ion solvation dynamics in supercritical fluids. *Phys. Rev. Lett.* **2004,** 93, (2).

8. Egorov, S. A., Solvation dynamics in supercritical fluids: Equilibrium versus nonequilibrium solvent response functions. *J. Chem. Phys.* **2004,** 121, (14), 6948-6955.

9. Kometani, N.; Arzhantsev, S.; Maroncelli, M., Polar solvation and solvation dynamics in supercritical CHF3: Results from experiment and simulation. *J. Phys. Chem. A* **2006,** 110, (10), 3405-3413.

10. Braunecker, W. A.; Matyjaszewski, K., Recent mechanistic developments in atom transfer radical polymerization. *J. Mol. Cat. A* **2006,** 254, (1-2), 155-164.

11. Weiss, E. A.; Ahrens, M. J.; Sinks, L. E.; Ratner, M. A.; Wasielewski, M. R., Solvent control of spin-dependent charge recombination mechanisms within donor-conjugated bridge-acceptor molecules. *J. Am. Chem. Soc.* **2004,** 126, (31), 9510-9511.

12. Liu, M.; Waldeck, D. H.; Oliver, A. M.; Head, N. J.; Paddon-Row, M. N., Observation of dynamic solvent effect for electron tunneling in U-shaped molecules. *J. Am. Chem. Soc.* **2004,** 126, (34), 10778-10786.

13. Ratera, I.; Sporer, C.; Ruiz-Molina, D.; Ventosa, N.; Baggerman, J.; Brouwer, A. M.; Rovira, C.; Veciana, J., Solvent tuning from normal to inverted marcus region

of intramolecular electron transfer in ferrocene-based organic radicals. *J. Am. Chem. Soc.* **2007,** 129, (19), 6117-6129.

14. Smith, W.; Forester, T. R., DL_POLY_2.0: A general-purpose parallel molecular dynamics simulation package. *J. Molecular Graphics* **1996,** 14, (3), 136-141.

15. Pranata, J.; Wierschke, S. G.; Jorgensen, W. L., OPLS ootential functions for nucleotide bases - relative association constants of hydrogen-bonded base-pairs in chloroform. *J. Am. Chem. Soc.* **1991,** 113, (8), 2810-2819.

16. Jorgensen, W. L., Optimized intermolecular potential functions for liquid alcohols. *J. Phys. Chem.* **1986,** 90, (7), 1276-1284.

17. Jorgensen, W. L.; Briggs, J. M.; Contreras, M. L., Relative partition-coefficients for organic solutes from fluid simulations. *J. Phys. Chem.* **1990,** 94, (4), 1683-1686.

18. Potoff, J. J.; Siepmann, J. I., Vapor-liquid equilibria of mixtures containing alkanes, carbon dioxide, and nitrogen. *Aiche J.* **2001,** 47, (7), 1676-1682.

19. Patel, N. C.; Teja, A. S., A new cubic equation of state for fluids and fluid mixtures. *Chem. Eng. Sci.* **1982,** 37, (3), 463-473.

20. Cichos, F.; Brown, R.; Bopp, P. A., Coupled molecular dynamics/semiempirical simulation of organic solutes in polar liquids. II. Coumarin 153 in methanol and acetonitrile. *J. Chem. Phys.* **2001,** 114, (15), 6834-6842.

21. Shukla, C. L.; Hallett, J. P.; Popov, A. V.; Hernandez, R.; Liotta, C. L.; Eckert, C. A., Molecular dynamics simulation of the cybotactic region in gas-expanded methanol- carbon dioxide and acetone-carbon dioxide mixtures. *J. Phys. Chem. B* **2006,** 110, (47), 24101-24111.

22. Horng, M. L.; Gardecki, J. A.; Papazyan, A.; Maroncelli, M., Subpicosecond measurements of polar solvation dynamics: Coumarin 153 revisited. *J. Phys. Chem.* **1995,** 99, (48), 17311-17337.

CHAPTER 5: EFFECTS OF SOLVENT STRUCTURE ON SOLVATOCHROMISM IN GAS-EXPANDED METHANOL

Introduction

Several studies, including the work presented in Chapter 3 have used spectroscopy to explore the cybotactic region around a solute molecule in organic liquids,[1] GXLs,[2-5] and SCFs.[6] Other studies have used MD simulations to calculate solvatochromic shifts in SCFs[7] and GXLs[2] for a direct experimental comparison. Calculating solvatochromic shifts are outside the scope of this work; however, linking solvent structural patterns to solvatochromic behavior is of interest. This chapter explores solvation around the simple heterocyclic probes shown in Figure 5.1 and the effect on solvatochromic behavior. Absorption spectra and radial distribution functions (RDFs) are very dependent on the solute structure. Simple changes in molecular structure lead to markedly different solvation patterns and absorption spectra, so the solutes are ideal probes for structure-property relationships. GXLs are unique solvents where a variety of intermolecular interactions are possible by cosolvent and/or pressure adjustments, and therefore requires chromophores that are sensitive to solvent interactions.

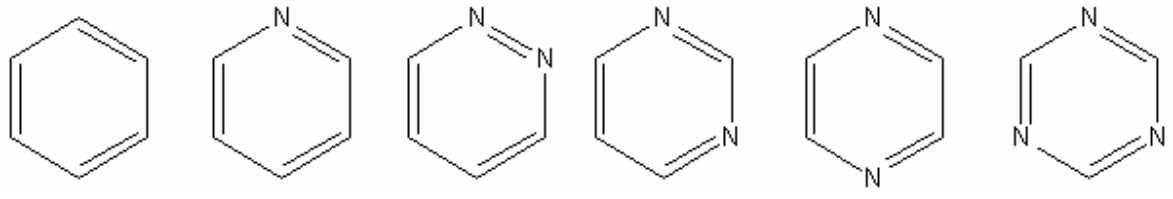

Figure 5.1: Solutes used in this study, from left: benzene, pyridine, pyridazine, pyrimidine, pyrazine, 1,3,5 triazine.

Absorption spectra of these heterocyclic compounds in organic solvents[8-12] (including MeOH) are solute dependent. Restructuring the nitrogen atoms on an aromatic ring changes the spectral characteristics. The solutes either show a decrease in dipole moment when excited or have a zero net dipole moment, as in the cases of benzene and pyrazine, so typical solvatochromic behavior is not observed. Excitation delocalizes the lone pair electrons on the nitrogen atoms into the π-cloud, and any interference with the delocalization increases the energy of transition (related to the maximum absorption wavelength, λ_{max}). CO_2 and MeOH interact with the lone-pair electrons and increase the transition energy, which decreases the λ_{max} observed in the absorption spectra. Consequently, MeOH-nitrogen hydrogen bonds, Lewis acid/base interactions with CO_2, and local polarity affect delocalization and ultimately the spectroscopy.

The arrangement of solvent molecules in the cybotactic regions has a large effect on absorption. In this case both CO_2 and MeOH interact with nitrogen and the proximity to the lone-pair impacts the spectra. Unfortunately spectroscopy can indicate only solvent distribution. MD simulations provide atomic-level solvent structures that give insight into solvent effects on absorption. This work further exemplifies the synergy of experiments and theory that was introduced in Chapter 3. Neither independent method gives the complete picture of electronic excitation, but their combination uses MD simulations to explore the structure-property relationship of absorption.

Experimental Techniques

Materials

All solutes (benzene, toluene, phenol, 2-naphthol, pyridine, pyridazine, pyrimidine, pyrazine and 1,3,5-triazine, analytical grade) were purchased from Sigma-Aldrich. All were used as received. Carbon dioxide was purchased from Airgas and dried over molecular sieves prior to use. Anhydrous methanol, from Sigma-Aldrich, was used in the UV/vis spectroscopy experiments.

UV/Vis Absorption

Absorption spectra were obtained using a Hewlett Packard 1050 series detector. Solvatochromic experiments were performed in a high-pressure optical cell equipped with sapphire windows and cooling jacket externally connected to a temperature-controlled ethylene glycol bath. Temperature was measured with an Omega J-type thermocouple (with 0.1°C precision) in contact with the liquid phase. Temperature was maintained at 40°C throughout the experiment. CO_2 was added to the cell with an Isco syringe pump and pressure was measured with a Druck pressure transducer with 1 psi precision. Samples were allowed to equilibrate for several hours before recording spectra.

Computational Methods

Force Fields and Ensembles Used

Representative conditions from each GXL was selected from experiments and used to conduct detailed and extensive MD simulations of the heterocyclic solutes in CO_2-expanded MeOH. The simulated systems are neat MeOH, 25%, and 75% CO_2 at 40°C. The simulation system represents a single liquid phase with the compositions and pressure determined by these experiments and the density determined by the Patel-Teja equation of state.[13]

Carbon dioxide and MeOH have been modeled as rigid collections of atomic sites with specified fixed charges interacting through pairwise-additive, site-site Lennard Jones and Coulomb forces. Equation 5.1 is the force field used in the CO_2-MeOH systems.

$$u_{ij} = \sum_i \sum_{j>i} \left[4\varepsilon_{ij} \left\{ \left(\frac{\sigma_{ij}}{r_{ij}} \right)^{12} - \left(\frac{\sigma_{ij}}{r_{ij}} \right)^{6} \right\} + \frac{q_i q_j}{r_{ij}} \right] \qquad \text{Equation 5.1}$$

Carbon dioxide pair interactions have been modeled using the TrAPPE potential.[14] The J2 potential[15] has been used for MeOH pair interactions. The potentials for pyridine, pyrimidine, pyridazine, pyrazine, and benzene are OPLS-derived.[16,17] 1,3,5-triazine was not used in the computational study due to the lack of a reliable force model. Each of the pairwise potentials specifies a representation for the fixed point charges and these are assumed to remain fixed in the heterogeneous pairwise Coulombic interactions.

Molecular dynamics (MD) simulations were carried out using the DL_POLY Software package.[18] Regardless of the relative composition, each simulated system box is populated by a total of 1001 molecules: one solute molecule and 1000 solvent/cosolvent molecules. Cubic periodic boundary conditions (PBCs) are used throughout, but the length of the system box is scaled to preserve the specified density. As a result, pair-wise terms in the potential were cut off at half the box length. Coulombic interactions were handled internally by DL_POLY with the Ewald summation method using the "automatic parameter optimization" option with a tolerance of 1E-5. The equations of motion were integrated using a time step of 2 fs with the Velocity verlet algorithm as implemented by DL_POLY. Initial configurations were generated by randomly distributing solvent molecules around a centralized solute and equilibrating using velocity rescaling for 200 ps in the canonical (NVT) ensemble. Temperature was thermostated using a Nose-Hoover

thermostat with 1ps relaxation time constant. Following equilibration, a long equilibrium simulation was run in the NVT ensemble. Trajectories were saved every 5ps and used as initial configurations for the transport and structural studies. Statistics of 100 trajectories were recorded over 500ps of MD simulation runs in the microcanonical (NVE) ensemble.

Radial distribution functions (RDFs), calculated by Equation 5.2, measure solvent structures by giving the most probable distances between atoms. In this study RDFs of nitrogen on the solute, or center of mass of benzene, and either the MeOH protic hydrogen or the CO_2 carbon are considered.

$$g(r) = \frac{< n(r) >}{\rho \cdot 4\pi \cdot r^2 \Delta r} \qquad \text{Equation 5.2}$$

where *g(r)* is the radial distribution function, *n(r)* is the average number of atoms in a spherical shell of width Δr at distance r, and ρ is the bulk density.. Higher dimension distribution functions were used to create solvent maps around benzene, pyridine, and pyridazine. Only these solutes were considered because information can be generalized to the other solutes and the corresponding RDFs. Extra dimensionality provides better spatial resolution around the solute and gives solvation information that is unobtainable or lost in one dimension. 3-dimensional (3D) solvent distribution functions, g(x,y,z) are found by periodically dividing the simulation box into finite elements and recording the positions of solvent atoms relative to benzene's center of mass or a nitrogen atom on pyridine and pyridazine. The magnitude of the distribution function in each finite element is calculated by Equation 5.3.

$$g(x,y,z) = \frac{\langle N_{Cell} \rangle / V_{Cell}}{N_{Box} / V_{Box}} \qquad \text{Equation 5.3}$$

where $<N_{Cell}>$ is the average number of a particular atom in a finite element of volume, V_{Cell}. N_{Box} and V_{Box} are the total number of a particular atom in the simulation box and volume of the simulation box, respectively. The DL_POLY source code was altered to accommodate the 3D distribution functions. Solvent distribution maps are then created by shading the finite elements according to the magnitude of the distribution function. The maps shown in this work are 2D sample planes that depict MeOH and CO_2 solvation of the solutes from in-plane perspectives.

Results and Discussion

UV/vis Solvatochromism

Solvent-dependent absorption, or solvatochromism, probes local polarity and solvent interactions with a chromophore.[19] The term local is used to emphasize the short-range effect that solvent polarity and specific interactions have on absorption. It is assumed that the absorption spectra are influenced by molecules within the cybotactic region; consequently interactions that could influence diffusion are assumed to occur within this region. Generally, a more polar local environment decreases the energy of transition required to electronically excite a chromophore, which is inversely proportional to the wavelength of maximum absorption (λ_{max}). This behavior is termed positive solvatochromism. The azo compounds used here display negative solvatochromism, where increased solvent polarity causes a blue shift (lower wavelength) in the λ_{max}[11,20] because the dipole moment decreases upon excitation.[11] Lone pair electrons on the nitrogen atoms results in a large ground-state dipole moment; after excitation, the lone-pair electrons become delocalized in the ring and the dipole moment decreases. Polar solvents hinder electron delocalization, particularly if the solvent can participate in

specific interactions, requiring additional energy for excitation. CO_2-expanded MeOH can form hydrogen bonds through MeOH and Lewis acid/base interactions through CO_2. Both would decrease the λ_{max}.

The six probes give very different spectra and solvatochromic behavior depending on the structural features of the probe. Benzene is the only solute that cannot form specific interactions with either solvent component; and as expected the absorption spectra (Figure 5.2) display positive solvatochromism, due to decreased solvent polarity with added CO_2. The blue shift is small (~1-2 nm) because benzene has no net dipole moment in either the ground state or excited state. The other non-dipolar solvents, pyrazine and 1,3,5-triazine have nitrogen atoms that can interact with both MeOH and CO_2. Pyrazine's spectra (Figure 5.3) blue shift slightly (~1nm) with added CO_2 because CO_2 interacts with the nitrogen. Other studies have shown that hydrogen bonding causes a large solvatochromic shift between isooctane and MeOH,[11,12] meaning the additional blue shift from CO_2-nitrogen interactions are small relative to hydrogen bonds, but important. Pyridine also displays this behavior (Figure 5.4) because of CO_2 interactions. A more dramatic blue shift with CO_2 is seen in 1,3,5-triazine (Figure 5.5a). A subsequent experiment in CO_2-expanded hexane exhibits a large blue shift (~5nm) with added CO_2 (Figure 5.5b). This proves that specific CO_2-nitrogen interactions are very influential on spectra because CO_2 is considered non-polar and a blue shift could only arise from a specific interaction with nitrogen.

Pyrimidine does not shift with CO_2 addition, but three absorption peaks between 260-270nm appear when a small amount of CO_2 is added to MeOH (Figure 5.6). Similar behavior was seen in the absorption spectra in isopentane/ethanol mixtures where

increased isopentane led to the appearance of these peaks on the blue side[10]. A significant solvatochromic shift was detected because of ethanol hydrogen bonding. These absorption peaks are consistent with n-π* transitions, which typically absorb at lower frequency than π-π* transitions. In neat MeOH the n-π* transitions could be negated by strong MeOH-nitrogen hydrogen bonds. As CO_2 is introduced, hydrogen bonds are replaced by weaker CO_2 interactions which are favorable to the n-π* transition. This pattern is unique to pyrimidine, which is the only solute with two isolated nitrogens and a dipole moment, thus more susceptible to specific solvent-nitrogen interactions. Pyridazine is the only solute that red shifts with added CO_2 pressure as seen in Figure 5.7. RDFs indicate decreased CO_2 interactions with the nitrogen atoms at higher CO_2 concentration are responsible for the red shift.

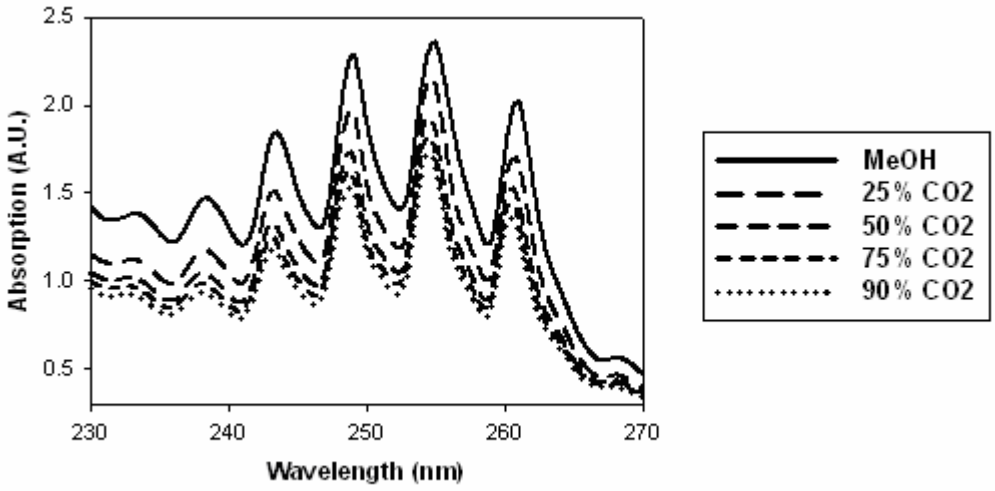

Figure 5.2: Benzene absorption spectra in CO_2-expanded MeOH.

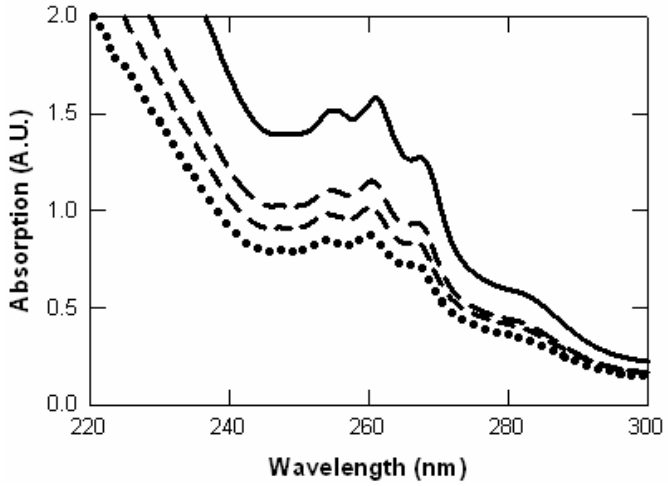

Figure 5.3: Pyrazine absorption spectra in MeOH GXLs. Lines represent the same compositions as Figure 5.2.

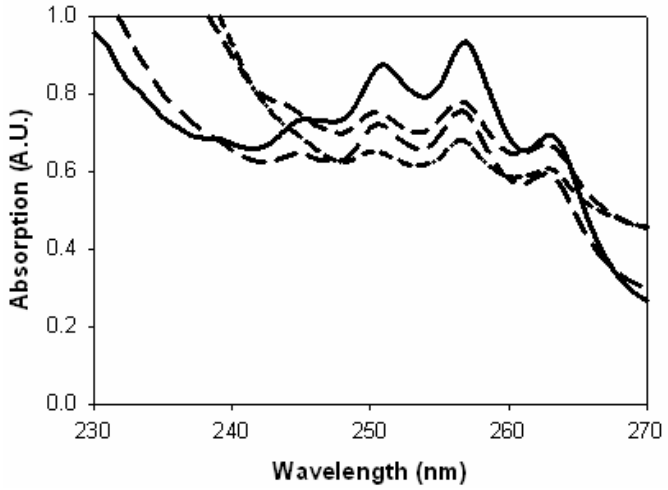

Figure 5.4: Pyridine absorption spectra in MeOH GXLs. Lines represent the same compositions as Figure 5.2.

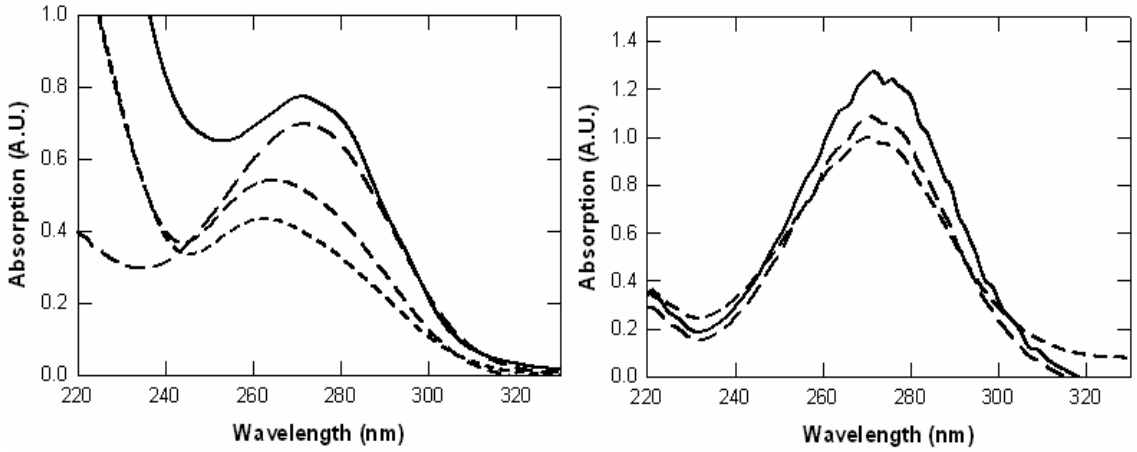

Figure 5.5: 1,3,5 Triazine absorption spectra in CO_2-expanded MeOH (left) and CO_2-expanded hexane (right). Lines represent the same compositions as Figure 5.2.

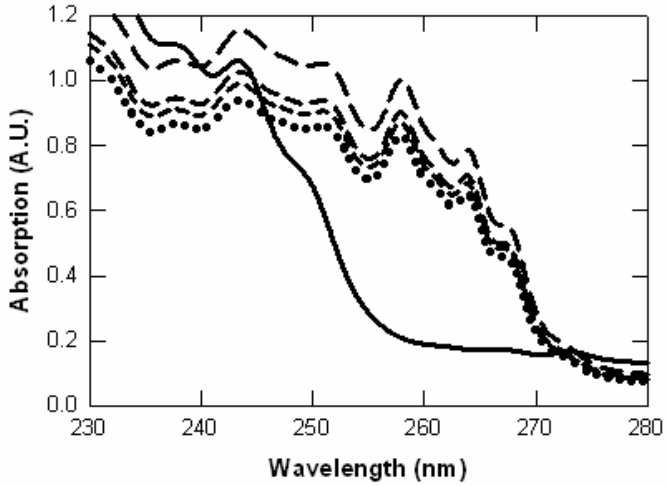

Figure 5.6: Pyrimidine absorption spectra in MeOH GXLs. Lines represent the same compositions as Figure 5.2.

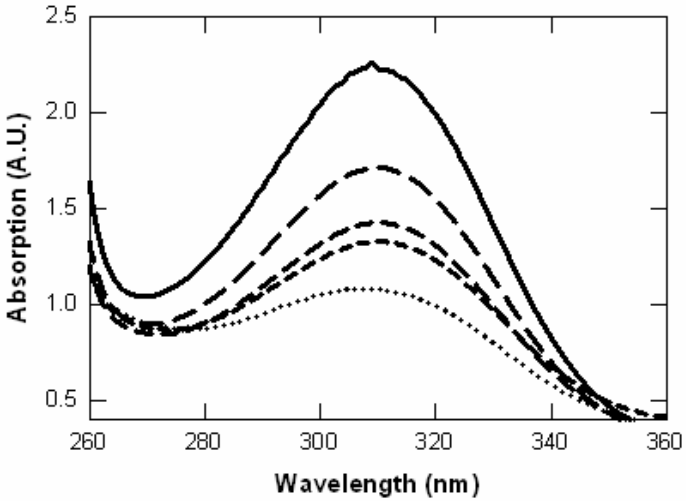

Figure 5.7: Pyridazine absorption spectra in MeOH GXLs. Lines represent the same compositions as Figure 5.2.

Solvent Structure

Molecular dynamics simulations provide atomic level structural details that aid the interpretation of spectra and diffusion results. RDFs between the solvent components and the solute nitrogen(s) indicate that both CO_2 and MeOH influence solvatochromic properties. Solute center-of-mass RDFs give less insight into solvent effects on spectra and diffusion and will therefore not be provided. Instead 2-dimensional solvent maps around the aromatic are shown because solvent ordering around the aromatic ring provides a general understanding about heterocyclic solvation. This structural analysis shows that while MeOH-nitrogen hydrogen bonds are the predominant interaction; CO_2 can interact with the probe and disrupt short and long-range solvent structure, ultimately affecting the absorption spectroscopy. The solvatochromic shift relative to pure MeOH is more dependent on the CO_2-nitrogen interactions than hydrogen bonds.

Benzene

UV/vis absorption suggests that the micro-environment around benzene becomes increasingly non-polar with CO_2 addition. Center-of-mass RDFs and 2-dimensional orientational distribution functions show that the solvent forms a neatly organized cage around the solute. Benzene is the only solute where center-of-mass RDFs and 2D distribution functions are considered because benzene lacks nitrogen atoms and many of the solvation features can be generalized to the other solute molecules. The 2D solvent distribution functions for CO_2 and MeOH are shown in Figure 5.8. These display solvation above and below the benzene molecule from an in-plane perspective. The distinct feature of MeOH solvation is the two areas ~3Å above the center of the ring. MeOH forms a circular solvent cage around benzene with significant agglomeration directly behind the two clusters. CO_2 forms an ovoid solvent cage with a higher composition than MeOH and increased clustering directly behind the two MeOH clusters at 3Å from the solute. These 2D solvent features can be used to analyze features in the 1D RDFs shown in Figure 5.9.

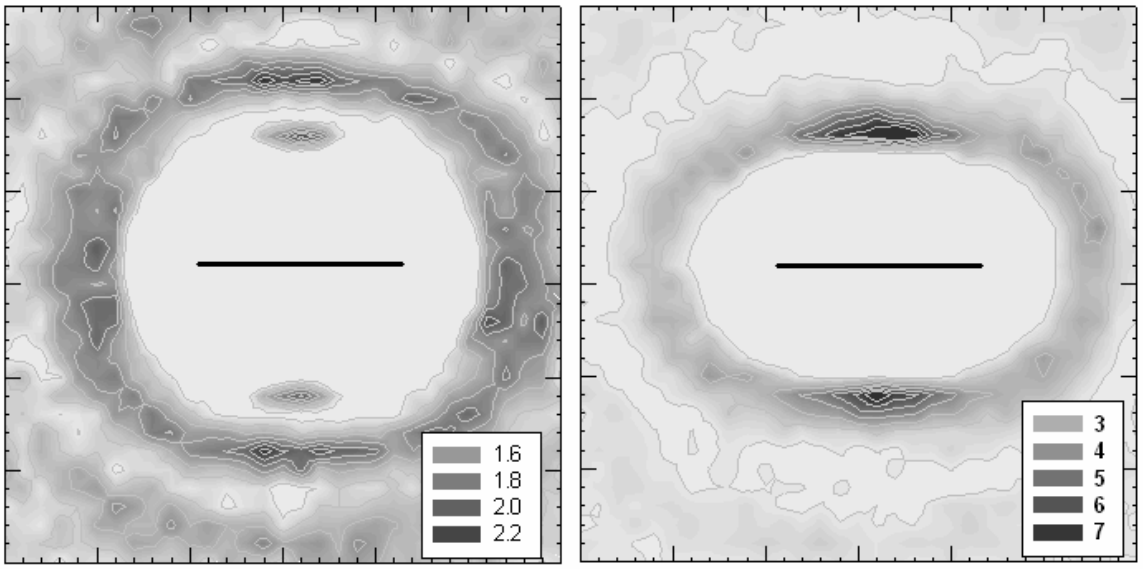

Figure 5.8: 3D distribution function from an in-plane perspective to illustrate MeOH accumulation (Left) and CO_2 accumulation (Right) above and below the benzene molecular plane. The horizontal line represents the benzene molecule. Tick marks are ~0.5Å apart.

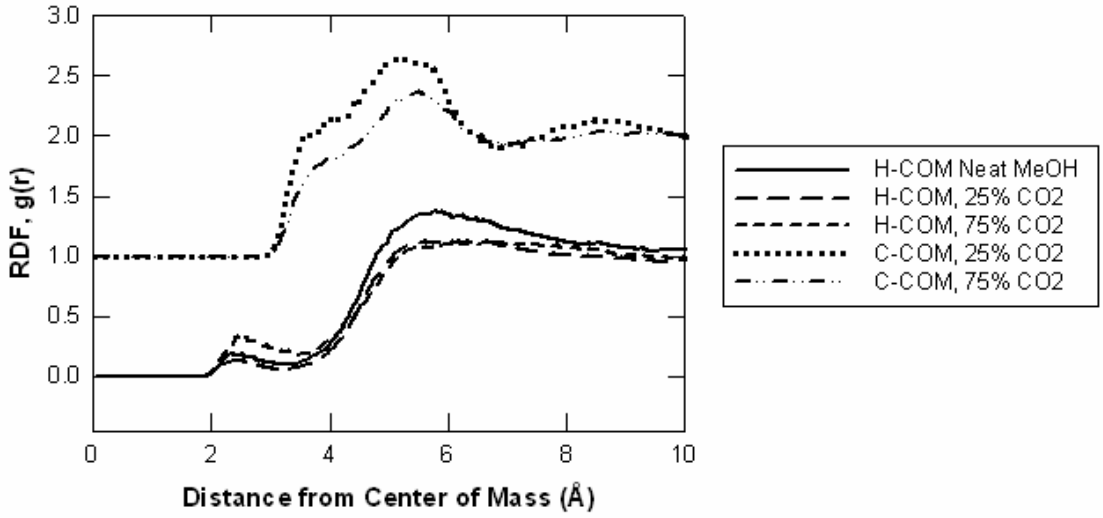

Figure 5.9: Benzene RDF from benzene's center of mass (COM) to either the MeOH protic hydrogen (H) or the CO_2 carbon (C). The insert shows the corresponding lines for the RDF type in the different GXLs. CO_2 RDFs have been offset by one.

The small (< 1) MeOH peaks near 2.5Å arise from the small MeOH cluster ~3Å from the center of mass. The broad peaks located between 5-7Å are the result of the solvent cage that MeOH forms around benzene. The magnitude of the broad peaks is slightly greater than unity, which means the local MeOH composition inside the solvent cage is larger than the bulk MeOH composition. This agrees with the 2D structure where the magnitude of the distribution function is between one and two. The broad peak characteristic is due to solvent cage asymmetry where some portions of the solvent cage are further from the probe than others because the cage is not a perfect sphere. The CO_2 RDFs have a broad peak at 5Å with a shoulder at 4Å. The shoulder occurs because of the CO_2 enhancements in the solvent cage directly behind the MeOH clusters 3Å above benzene. The CO_2 enhancements are closer to benzene because of the non-spherical solvent cage. The peak is due to the remainder of the solvent cage. A smaller peak at 8Å indicates long-ranged solvent ordering around benzene where CO_2 and MeOH solvent shells alternate. The RDFs show overlap between the MeOH and CO_2 solvent cages, which is better seen in the 2D solvent maps. A faint ring of CO_2 enhancement can be seen beyond the initial CO_2 cage in Figure 5.8 which is responsible for the peak at 3Å. The alternating MeOH/CO_2 solvation pattern is only seen in the 25% CO_2 GXL. At 75% CO_2 the 8Å CO_2 peak is almost non-existent and is substantially overlapped by the second MeOH peak. This implies a breakdown of the long range structure at higher CO_2 concentrations. Benzene solvation patterns provide an in depth look into general solvation patterns around heterocyclic molecules. Solvent ordering around the nitrogen atoms has a profound effect on the absorption spectroscopy and will consequently be the focus of the other solutes.

Pyridine

Interesting structural behavior occurs in the second and third solvent shells as seen in Figure 5.10. The first CO_2 and MeOH peaks remain at the same distance regardless of composition, but the proximity of the first MeOH peak indicates a hydrogen bond with the nitrogen atom. CO_2 addition causes the second and third CO_2 solvent shells to shift further from the nitrogen atom but become more well-defined. The second MeOH peaks show that MeOH is displaced by CO_2 when GXLs are formed. Another interesting feature of pyridine's solvent structure is the absence of the alternating CO_2/MeOH solvent shells that occurs with the other solutes. Beyond the first CO_2 peak there is substantial overlap of MeOH with the CO_2 peaks. This pattern could result from increasingly bulk-like behavior far from the solute or secondary solvation effects from other parts of the solute.

The 3D CO_2 and MeOH maps for pyridine in a 25% CO_2/MeOH GXL are shown in Figure 5.11. These maps show solvent clustering from an in-plane perspective. CO_2 forms a shell around the nitrogen atom; most enhancements occur directly above and below the nitrogen atom, relative to the molecular plane. Some long-range structure is seen, but is insignificant relative to the first shell as indicated by the RDF. MeOH enhancements occur on the opposite side of pyridine; however, there are several clusters ~2Å from the nitrogen that cause the first peak in the RDF. MeOH displays more long-range ordering than CO_2 as denoted by the concentric enhancement patterns.

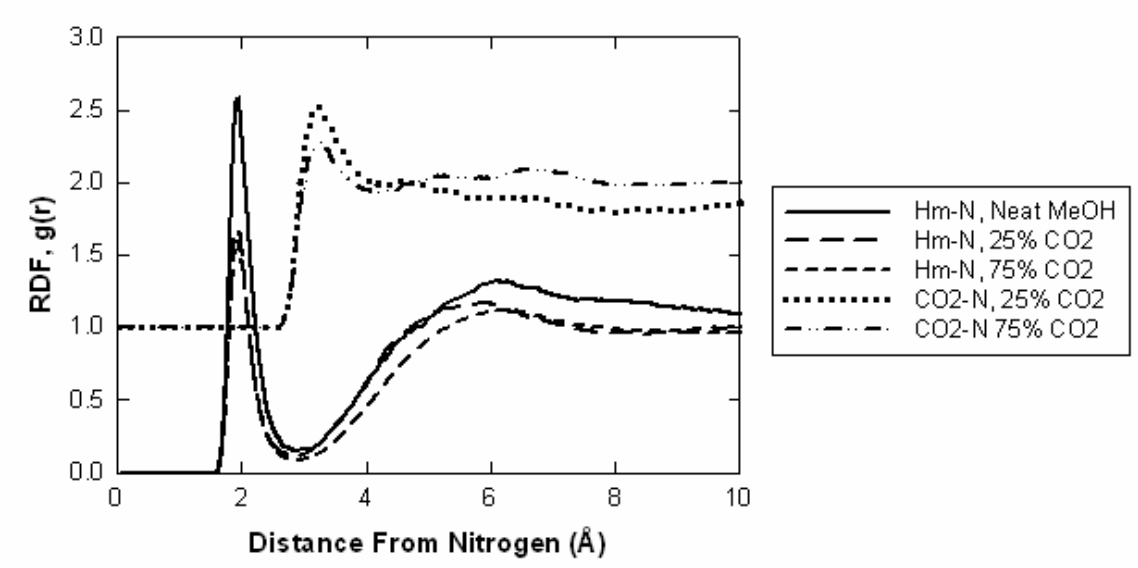

Figure 5.10: Pyridine RDFs from the nitrogen atom (N) to MeOH protic hydrogen (Hm) and CO_2 carbon atom at 313K and 150 bar. Insert corresponds to the CO_2 concentration of the solvent. CO_2 RDFs have been offset by one.

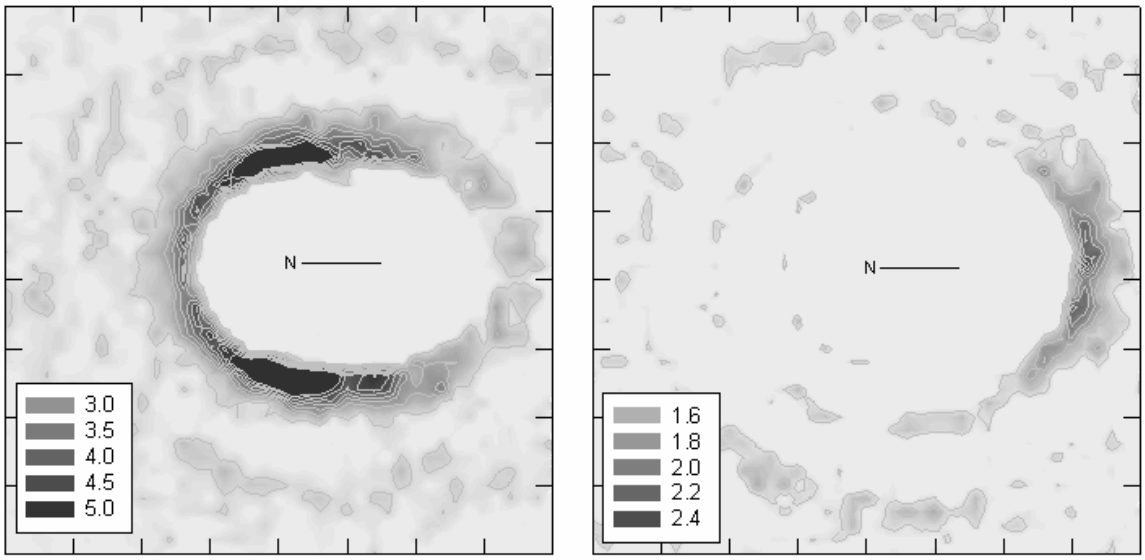

Figure 5.11: Pyridine solvent maps from in-plane perspective. CO_2 (left) MeOH (right).

Pyridazine

Pyridazine solvent structure, shown in Figure 5.12, has pressure-dependent CO_2 solvation patterns that could be responsible for the interesting absorption spectroscopy. The first CO_2 peak shifts from 3.1 to 3.5Å with added CO_2. This indicates weakened CO_2-nitrogen interactions which could facilitate a red shift in the absorption spectra. It is interesting to note the disappearance of the large CO_2 peak near 5Å between the 25% and 75% GXLs while the third CO_2 peak remains. As a result the alternating solvation pattern does not persist beyond the first solvent shells for the 25% CO_2 GXL. It does exist in the 75% GXL because of the peak. The entire MeOH structure remains at constant position, but increases in magnitude between 25% and 75% CO_2. There is little change in the structure between neat MeOH and the 25% CO_2 GXL.

Pyridazine solvent maps (Figure 5.13) show solvent ordering around the nitrogen atoms and the influence of hydrogen atom on the solvent structure. CO_2 and MeOH both accumulate in the same vicinity, directly below the nitrogen atoms in Figure 5.13, but CO_2 is slightly further from away from the nitrogen atoms than MeOH. Close examination of the two maps show that there are two CO_2 hot spots surrounding a single MeOH-rich area. CO_2 molecules are more persistent in this region forming a shell around the nitrogen atoms, while MeOH is localized to one small region. This suggests that a minimal number of MeOH molecules hydrogen bond to nitrogen. CO_2 molecules are more prevalent and free to interact in this region. This behavior has implications on the spectroscopy because the degree of CO_2 interaction with the nitrogen atoms dictates the transition energy. This phenomenon is composition-dependent and causes the observed red shift with added CO_2. Hydrogen influences the MeOH solvation pattern by pushing

the solvation shell back. There are MeOH enhancements between the hydrogen atoms, indicating interaction with the π-cloud. This is also seen in the CO_2 map, but to a lesser extent.

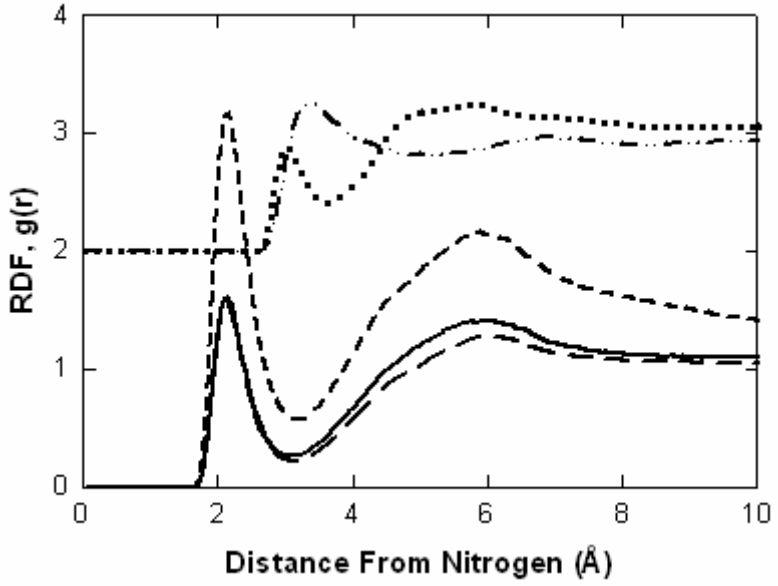

Figure 5.12: Pyridazine RDF at 313K and 150 bar between a pyridazine nitrogen atom and either MeOH protic hydrogen (Hm) or CO_2 carbon. Lines correspond to same features in Figure 5.10.

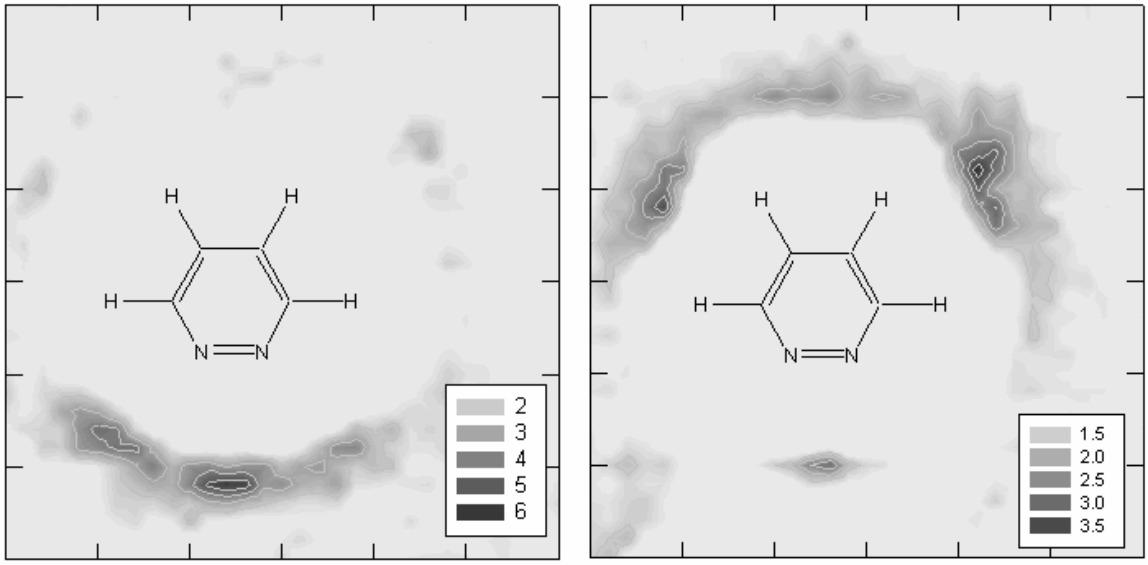

Figure 5.13: Pyridazine solvent maps from bird's eye perspective. CO_2 (left) MeOH (right).

Pyrimidine

Pyrimidine solvent maps for the 25% CO_2 GXL are shown in Figure 5.14. Several features that were seen in Pyridazine like the effect of hydrogens are present; but the overall structures are significantly different. The displacement of nitrogen has a big impact on the structure because a hydrogen atom separates them and disrupts the solvent shell. MeOH and CO_2 form localized solvent clusters around the nitrogen atoms instead of the large shell around the pyridazine nitrogen atoms. MeOH solvation at the nitrogen atoms is extremely large and explains the large MeOH peak in the RDF shown in Figure 5.15. The degree of CO_2 solvation is independent of bulk composition. MeOH solvation is very concentration dependent. A second MeOH shell at ~4.2Å is non-existent in neat MeOH but gradually becomes well defined with increasing CO_2 as does the broad third peak. This pattern influences the solvatochromic behavior where no shift was observed.

MeOH-nitrogen hydrogen bonds are strong and isolated by the adjacent hydrogens that CO_2 cannot displace MeOH. This is supported by the CO_2-nitrogen RDF which are independent of composition. Although no shift occurs, the two absorption peaks that are only present in the GXLs suggest CO_2 influences the MeOH solvation pattern and ultimately absorption spectra. This assumption is supported by the MeOH-nitrogen RDF which becomes larger in magnitude more ordered with added CO_2.

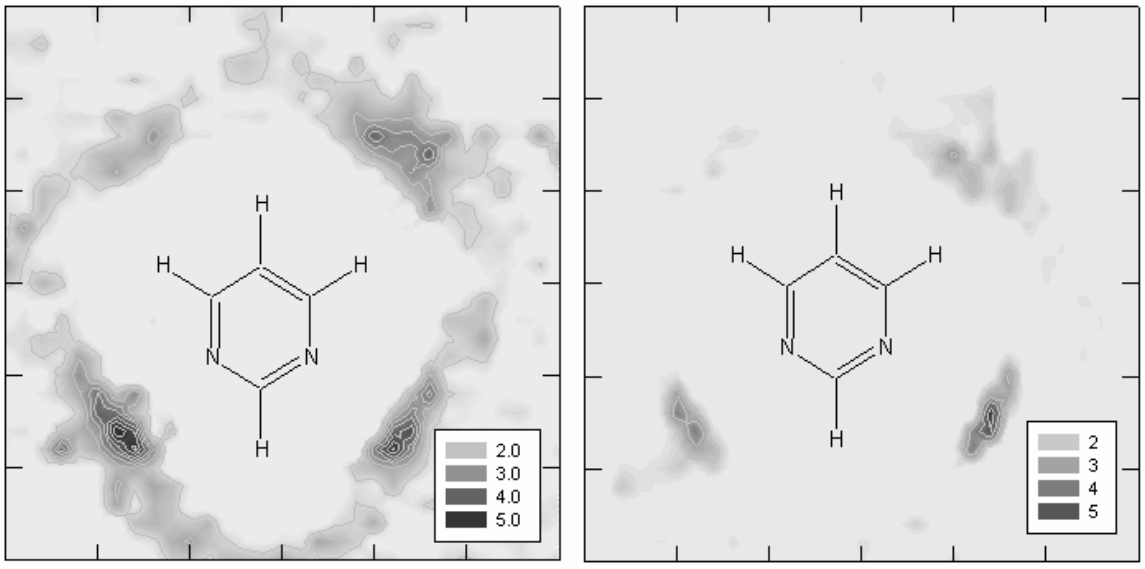

Figure 5.14: Bird's-eye-view view of CO_2 (left) and MeOH (right) solvent maps around pyrimidine.

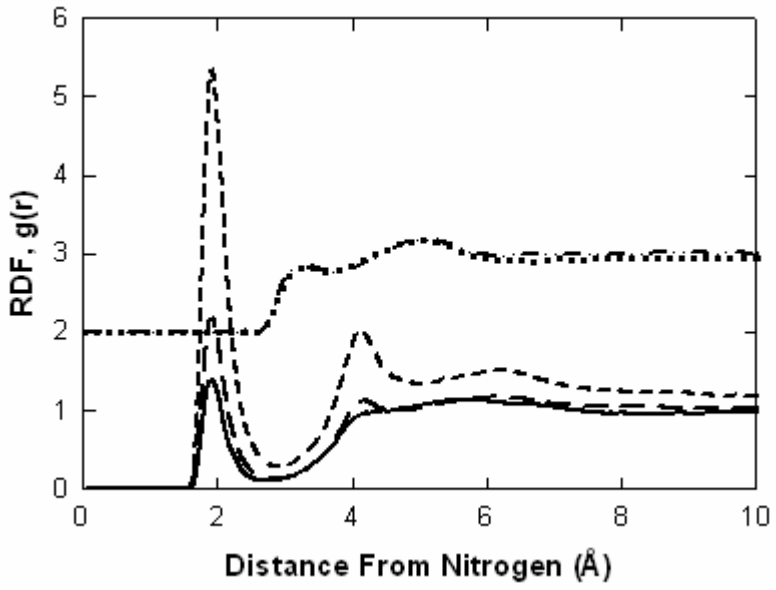

Figure 5.15: Pyrimidine RDF at 313K and 150 bar between a pyrimidine nitrogen atom and either MeOH protic hydrogen (Hm) or CO_2 carbon. Lines correspond to same features in Figure 5.10.

Pyrazine

Figure 5.16 shows CO_2 disruption of the secondary MeOH solvent structure, shifting the second peak further from the nitrogen atoms. The position of the first MeOH solvent shell remains unchanged with CO_2 dilution, but the magnitude is comparatively low. There is a crossover effect in the relative magnitudes of the first and second peaks. The pure MeOH first solvent shell peak is intermediate between 75% and 25% CO_2 peaks, but becomes the largest second-shell peak. This may be due to CO_2 displacing MeOH above and below the pyrazine plane. The 2D solvent maps around benzene indicate that CO_2 favors the aromatic ring. The CO_2 peaks remains at the same position in both GXLs, but decrease in magnitude with added CO_2.

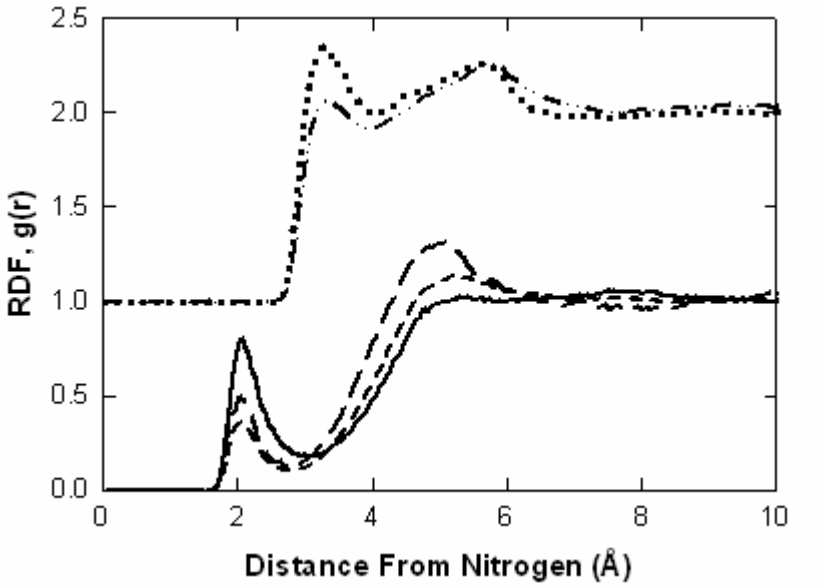

Figure 5.16: Pyrazine RDF at 313K and 150 bar between a pyrazine nitrogen atom and either MeOH protic hydrogen (Hm) or CO_2 carbon. Lines correspond to same features in Figure 5.10.

Conclusions

MD simulations reveal important structural information not attainable by solvatochromic experiments alone. As expected MeOH RDFs show significant hydrogen bonding interactions between the protic hydrogen and nitrogen atoms of the heterocyclic solutes that are concentration-dependent. Higher-ordered structure i.e. second solvent shell structure is also concentration dependent and exhibits alternating MeOH/CO_2 solvent shells well into the third solvent shell in some cases. More surprising are the solute structure effects on CO_2 solvation. CO_2-nitrogen RDFs are very dependent on bulk concentration where the first solvent shell can shift up to half an Angstrom. The impact on absorption spectroscopy is seen by the different solvatochromic behavior between the solute molecules. The solvatochromic and structural results presented here show that

molecular interactions are very dependent on the solute and the solvent choice and MD simulations give insight to spectroscopic phenomena.

References

1. Phillips, D. J.; Brennecke, J. F., Spectroscopic Measurement of Local Compositions in Binary Liquid Solvents and Comparison to the NRTL Equation. *Ind. Eng. Chem. Res.* **1993,** 32, (5), 943-951.

2. Li, H. P.; Arzhantsev, S.; Maroncelli, M., Solvation and solvatochromism in CO2-expanded liquids. 2. Experiment-simulation comparisons of preferential solvation in three prototypical mixtures. *J. Phys. Chem. B* **2007,** 111, (12), 3208-3221.

3. Ford, J. W.; Lu, J.; Liotta, C. L.; Eckert, C. A., Solvent effects on the kinetics of a Diels-Alder reaction in gas-expanded liquids. *Ind. Eng. Chem. Res.* **2008,** 47, (3), 632-637.

4. Gohres, J.; Kitchens, C.; Hallett, J.; Popov, A.; Hernandez, R.; Liotta, C.; Eckert, C., A spectroscopic and computational exploration of the cybotactic region of gas-expanded liquids: methanol and acetone. *J. Phys. Chem B, In Press. (doi:10.1021/jp077552p)* **2008,** 112, XXXX.

5. Gohres, J. L.; Hernandez, R.; Liotta, C. L.; Eckert, C. A., Viewing the cybotactic structure of gas-expanded liquids. In *Green Chemistry and Engineering with Gas Expanded Liquids and Near-critical Media. ACS Symposium Series Volume;*, Hutchenson, K. W.; Scurto, A. M.; Subramaniam, B., Eds. Oxford University Press: Oxford, 2008 (Submitted).

6. Rice, J. K.; Niemeyer, E. D.; Dunbar, R. A.; Bright, F. V., State-Dependent Solvation of Pyrene in Supercritical CO2. *J. Am. Chem. Soc.* **1995,** 117, (21), 5832-5839.

7. Kometani, N.; Arzhantsev, S.; Maroncelli, M., Polar solvation and solvation dynamics in supercritical CHF3: Results from experiment and simulation. *J. Phys. Chem. A* **2006,** 110, (10), 3405-3413.

8. Brealey, G. J.; Kasha, M., The role of hydrogen bonding in the n-pi-star blue-shift phenomenon. *J. Am. Chem. Soc.* **1955,** 77, (17), 4462-4468.

9. Krishna, V. G.; Goodman, L., Solvent effects on n-pi-star transitions in pyrazine. *J. Chem. Phys.* **1960,** 33, (2), 381-386.

10. Krishna, V. G.; Goodman, L., Protonation effects on n-Pi* transitions in pyrimidine. *J. Am. Chem. Soc.* **1961,** 83, (9), 2042-&.

11. Baba, H.; Goodman, L.; Valenti, P. C., Solvent Effects on Fluorescence Spectra of Diazines. Dipole Moments in (n, Pi) Excited States. *J. Am. Chem. Soc.* **1966,** 88, (23), 5410-&.

12. Hochstrasser, R. M.; Michaluk, J. W., Excited state dipole moment of pyridine. *J. Chem. Phys.* **1971,** 55, (9), 4668-&.

13. Patel, N. C.; Teja, A. S., A new cubic equation of state for fluids and fluid mixtures. *Chem. Eng. Sci.* **1982,** 37, (3), 463-473.

14. Potoff, J. J.; Siepmann, J. I., Vapor-liquid equilibria of mixtures containing alkanes, carbon dioxide, and nitrogen. *Aiche J.* **2001,** 47, (7), 1676-1682.

15. Jorgensen, W. L., Optimized intermolecular potential functions for liquid alcohols. *J. Phys. Chem.* **1986,** 90, (7), 1276-1284.

16. Duffy, E. M.; Kowalczyk, P. J.; Jorgensen, W. L., Do denaturants interact with aromatic-hydrocarbons in water? *J. Am. Chem. Soc.* **1993,** 115, (20), 9271-9275.

17. Jorgensen, W. L.; McDonald, N. A., Development of an all-atom force field for heterocycles. Properties of liquid pyridine and diazenes. *Theochem-J. Molec. Structure* **1998,** 424, (1-2), 145-155.

18. Smith, W.; Forester, T. R., DL_POLY_2.0: A general-purpose parallel molecular dynamics simulation package. *J. Molecular Graphics* **1996,** 14, (3), 136-141.

19. Reichardt, C., *Solvents and Solvent Effects in Organic Chemistry*. 2nd ed.; VCH: Weinheim, Germany, 1988.

20. Karelson, M.; Zerner, M. C., On the n-PI* blue shift accompanying solvation. *J. Am. Chem. Soc.* **1990,** 112, (25), 9405-9406.

CHAPTER 6: SPECTROSCOPIC MEASUREMENTS OF ALKYLCARBONIC ACID DISSOCIATION CONSTANTS IN CO_2-EXPANDED ALCOHOLS

Introduction

CO_2 and alcohols react under moderate pressure in gas-expanded liquids (GXLs) to form *in situ* acids called alkylcarbonic acids (ACAs),[1] which are similar to the formation of carbonic acid formed in CO_2/water mixtures. Unlike CO_2/water systems, CO_2 is highly soluble in alcohols and consequently the acid species exist in appreciable concentrations, making ACAs attractive for acid catalysis applications. ACAs can dissociate, or ionize, to the conjugate base and proton and is dependent on the alcohol. The multi-step ACA equilibrium[2] is shown below in Figure 6.1. The first step is the formation reaction with equilibrium constant K_1, the second reaction is the dissociation step with constant K_a.

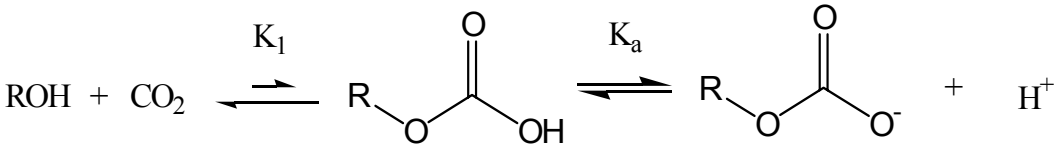

Figure 6.1 Alkylcarbonic acid formation and dissociation equilibrium reactions.

Acid catalysts are widely used in the chemical industry, but face environmental challenges: the need for neutralization with strong base and the concomitant formation of solid waste. ACAs exist in equilibrium systems and only exist when CO_2 is present. Venting the system reverses the equilibrium and destroys the ACA, thus eliminating neutralization and salt formation. The strength of acids is measured by their ability to

dissociate, or ionize, indicated by the acid's pK_a. This parameter is an important consideration when selecting an acid for catalysis; consequently, organic acids of comparable strength used in existing chemical processes can be replaced with environmentally benign ACAs. A recent kinetic study examining the acid catalyzed reaction of diazodiphenylmethane (DDM) showed that methylcarbonic acid (MCA) and ethylcarbonic acid (ECA) have faster reaction rates than carbonic acid (pK_a = 6.3 at 25°C). This suggests that the overall performance, and possibly the pK_a, are and larger than carbonic acid for MCA and comparable for ECA. A literature source reports the pK_a of MCA in water, to be 5.61[3] at 25°C determined by the hydrolysis reaction constant. This value is intermediate between carbonic acid and acetic acid. Most mineral acids used in industry have pK_a ~1, so ACAs are too weak to replace these acids if high concentrations are needed; however, ACAs have tunable properties and environmental benefits. Solution acidity can be changed orders of magnitude by alcohol substitution and the proton concentration can be fine tuned by changing the CO_2 pressure. As a result, ACAs are well suited for specialty applications or processes requiring dilute acid concentrations.

Recent studies by this group used ACAs as acid catalysis[2, 4-6] and a polarity switch in the formation of reversible ionic liquids[7]. The acid-catalyzed reaction of β-pinene into hydrolysis and hydrocarbon products is dependent on proton concentration;[2] therefore, the reaction can be designed to meet product specifications. Ionization constants are important criteria to select optimal operating conditions and the appropriate alcohol for a reaction system, but are difficult to measure in GXLs. Sampling from high-pressure systems require complex techniques and it is very difficult to sample without

disturbing the equilibrium. Spectroscopy is an *in situ* technique that avoids the problems of sampling from high pressure systems and has been used in extreme solvents like supercritical and nearcritical water,[8-10] sulfuric acid/ammonia,[11] and supercritical water/CO_2 mixtures.[12] The first and second ionization constants of carbonic acid were measured with spectroscopy[13, 14] and were in close agreement with literature values.

In this chapter three CO_2 expanded alcohols: MeOH, EtOH, and benzyl alcohol (BzOH) were studied with UV/vis spectroscopy. The results show the relative strength of each acid, but the multiple equilibrium nature of ACAs introduces a degree of freedom and complicates the analysis. Separation of the formation and dissociation constants (K_1 and K_a, respectively) requires an extra equation, so a novel approach is presented to overcome this problem. This technique is dependent on vapor-liquid equilibrium (VLE) and works only for the system MeOH/CO_2 because of unique characteristics of this system. Reasons for this behavior are discussed and "effective" equilibrium constants (K_{eff}) are presented as an alternative comparison tool.

Experimental Techniques

The dye 2,6 dinitrophenol (DNP) was used as an optical indicator because it is readily protonated in acidic medium and the acid and base forms absorb at 343nm and 425nm respectively. The relative concentrations of each peak are affected by the proton concentration and the equilibrium constants of DNP and the ACA can be found via the spectra and equilibrium relationships.

Materials

2,6 dinitrophenol (>99% purity) and anhydrous alcohols (MeOH, EtOH, BzOH) were obtained from Sigma-Aldrich and used as received. Alcohols were stored under inert gas (nitrogen or argon) and metered into an evacuated cell using a gas-tight syringe. CO_2 was obtained from Airgas and dried over molecular sieves prior to use in an Isco syringe pump.

Equipment

Absorption spectra were recorded on a Hewlett-Packard 1050 Series UV spectrometer. The high-pressure optical cell was equipped with sapphire windows and a cooling jacket that was connected externally to an ethylene glycol bath. Temperature was monitored by contacting the liquid phase with an Omega J-type thermocouple with 0.1°C precision. Pressure was measured with a Druck pressure transducer (1 psi precision) calibrated with a hydraulic balance system from Ruska. CO_2 was added to the optical cell with an Isco syringe pump. All spectra were deconvoluted and integrated with software from Origin Labs v8.0.

Procedure

A stock solution ($5x10^{-4}$ M) of DNP in the appropriate alcohol was made and stored under inert atmosphere. The solution was introduced to an evacuated cell with a gas-tight syringe to minimize water (specifically, carbonic acid) contamination. CO_2 was added to the cell via Isco pump to the appropriate pressure as determined by the Patel-Teja equation of state. The system was stirred with a magnetic stir bar at 25°C until the absorption spectrum remained constant. Acid-base kinetics were slow and each sample took at least 24 hours to equilibrate. Spectra were recorded at 100psi intervals, including

neat alcohol, up to 600psi. Spectra were deconvoluted with Gaussian fits and integrated. Absorption spectra at varying CO_2 compositions are shown in Figure 6.2 to Figure 6.4

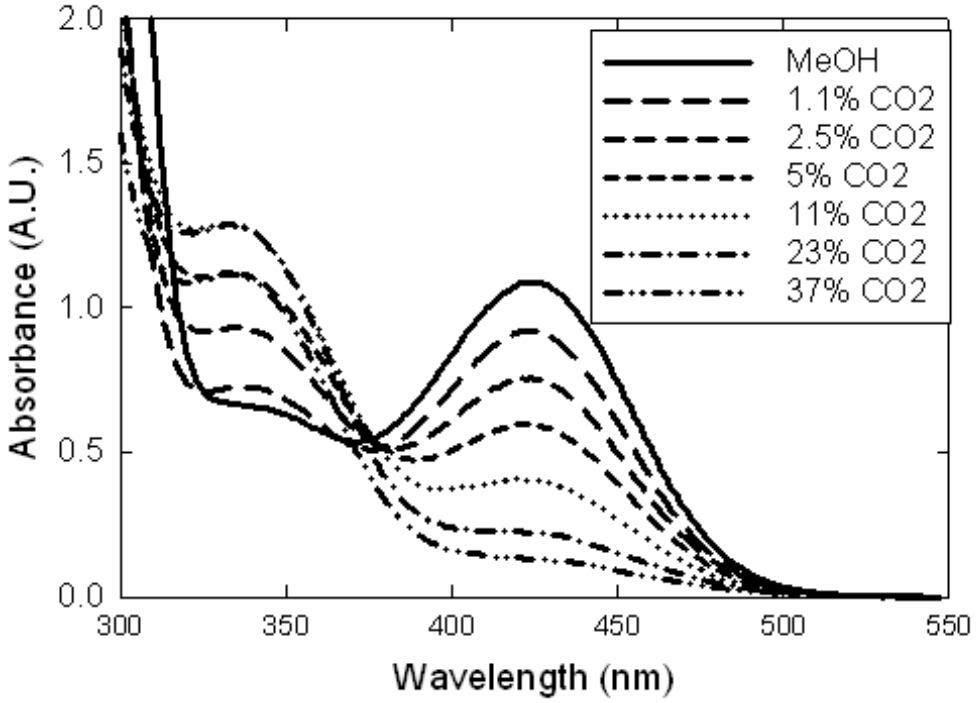

Figure 6.2: Absorption spectra of 2,6 DNP in MeOH/CO_2 at varying CO_2 composition.

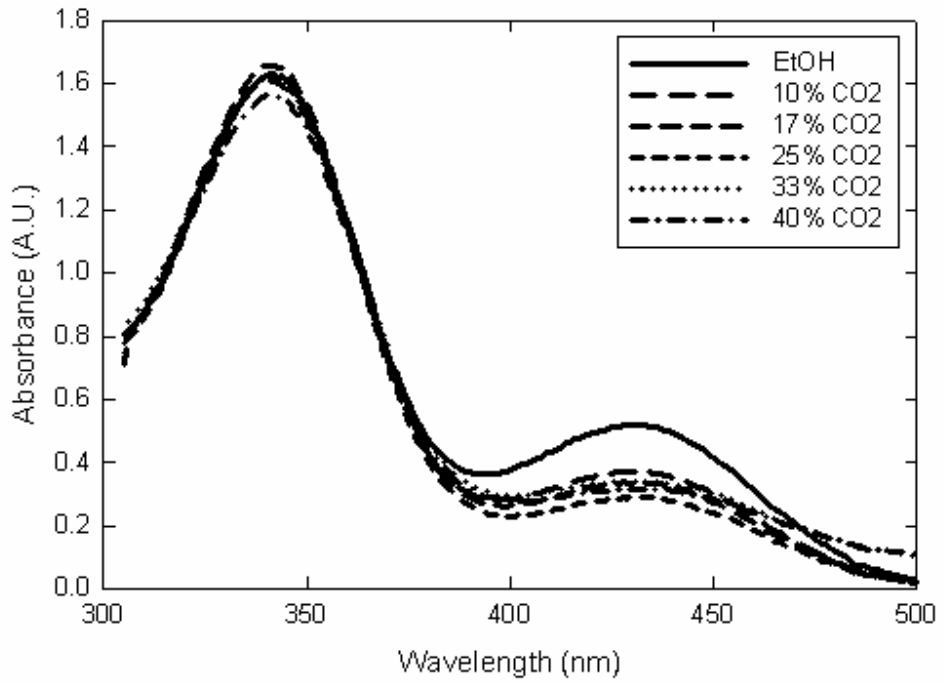

Figure 6.3: Absorption spectra of 2,6 DNP in EtOH/CO_2 at varying CO_2 composition.

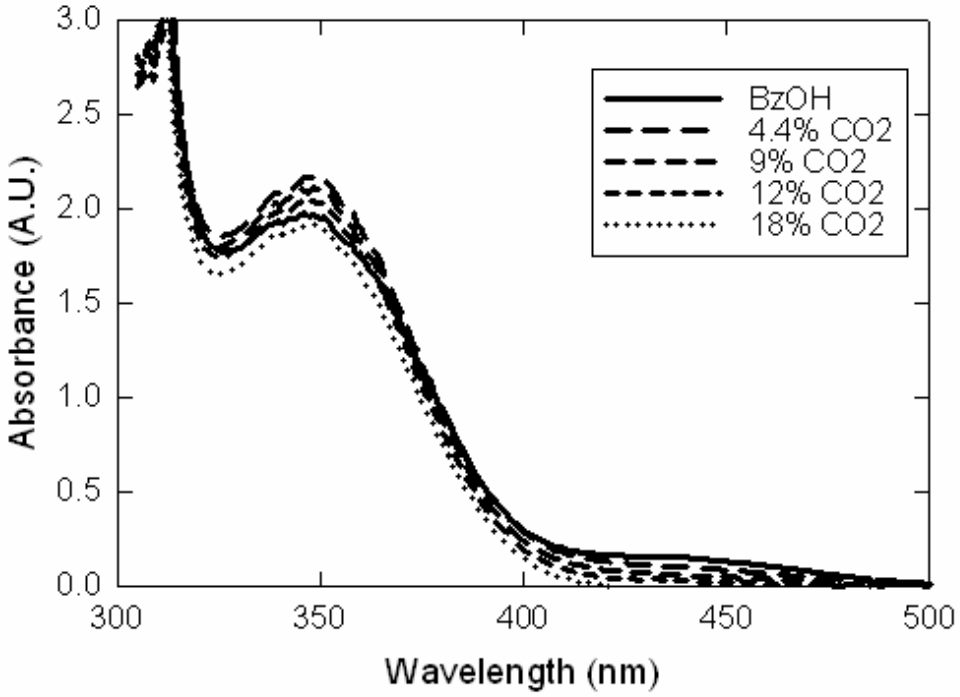

Figure 6.4: Absorption spectra of 2,6 DNP in BzOH/CO_2 at varying CO_2 composition.

Titrations

The Beer-Lambert law shown in Equation 6.1 relates absorption spectra to concentrations**.**

$$A(\lambda) = \varepsilon(\lambda)cl \qquad \text{Equation 6.1}$$

where A is absorption, ε is the molar absorptivity or extinction coefficient at a certain wavelength (λ), c is the molal concentration, and l is the path length. Absorption and molar absorptivity are dependent on the wavelength. Since the acidic and basic forms of DNP absorb at different wavelengths, there are two molar absorptivities for the acidic and basic forms that must be determined in each alcohol to determine concentrations of both forms. Absorption versus concentration curves of each form were constructed by bleaching the acidic or basic peak with NaOH and trifluoroacetic (TFA) acid respectively. Because the path length is constant, it was lumped with the molar absorptivity term. A sample spectra of the basic and absorption spectra in the three alcohols are shown in Figure 6.5, Figure 6.6, and Figure 6.7 and a calibration curve of the basic form in MeOH is shown in Figure 6.8. All molar absorptivity ratios are provided in Table 6.1.

Table 6.1: 2,6 DNP dissociation constants in the three neat alcohols and molar absorptivity ratios

	MeOH	**EtOH**	**BzOH**
pK_{DNP}	4.34	4.49	7.24
$\varepsilon_{acid}/\varepsilon_{base}$	0.33	0.48	0.27

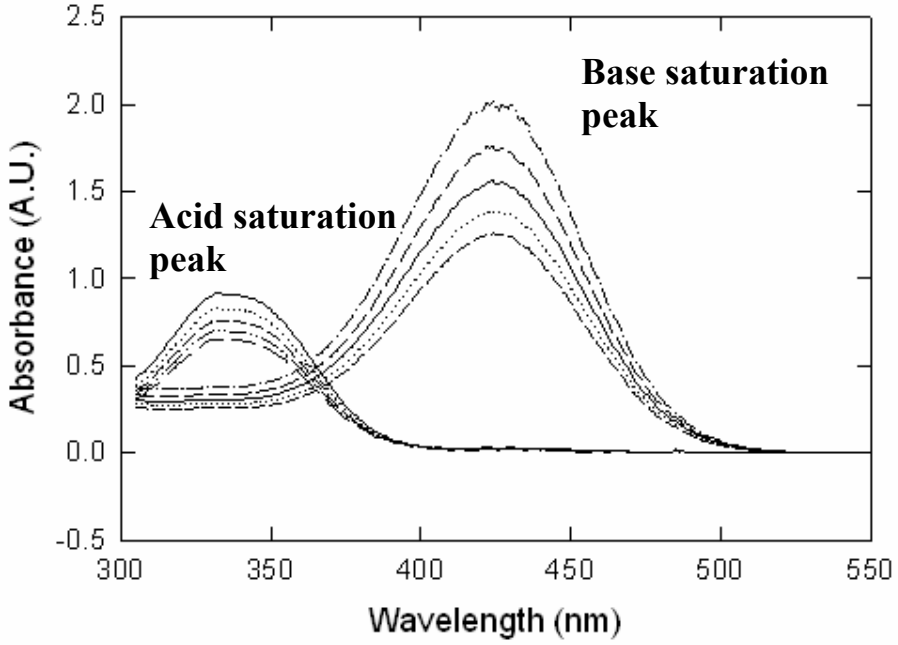

Figure 6.5: Acid and base absorption spectra in MeOH after saturation with TFA and NaOH.

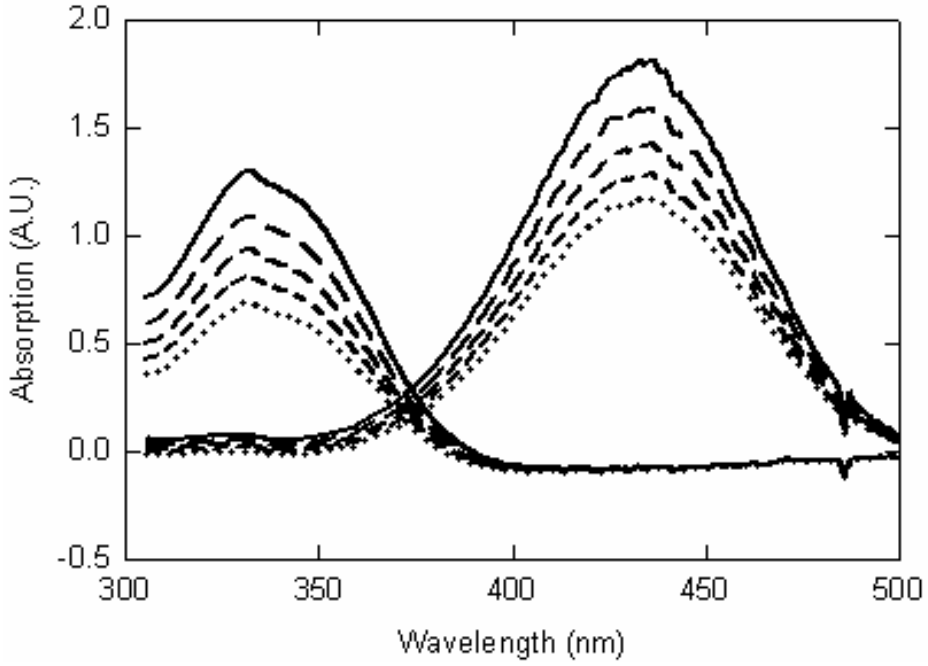

Figure 6.6: Acid and base absorption spectra in EtOH after saturation with TFA and NaOH.

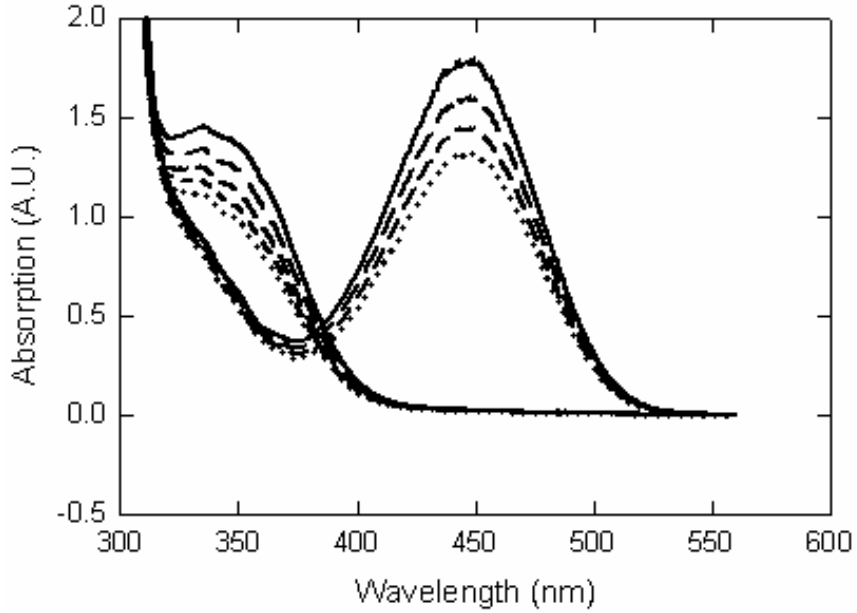

Figure 6.7: Acid and base absorption spectra in BzOH after saturation with TFA and NaOH.

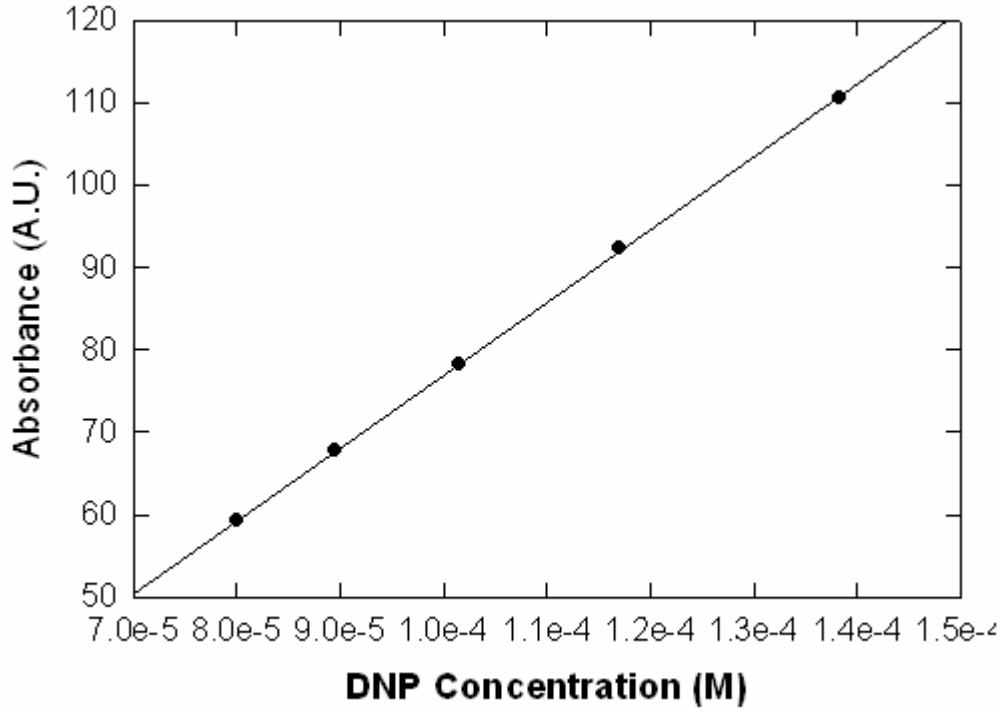

Figure 6.8: Calibration curve of the basic form of 2,6 DNP in EtOH.

Results and Discussion

Dissociation constant of 2,6 dinitrophenol

DNP has a dissociation constant as shown in Figure 6.9. The pK_a of DNP in water is 3.69 at 25°C, but is solvent dependent and must be determined in each alcohol considered.[15]

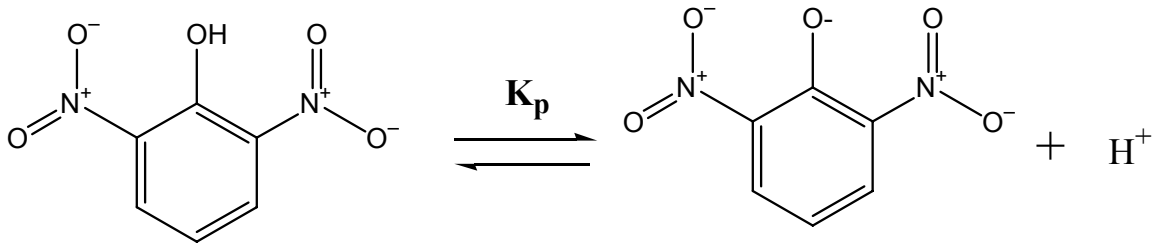

Figure 6.9: 2,6 DNP equilibrium.

Variability from CO_2 addition was not considered as ACA formation would complicate the analysis. This is a reasonable estimate at all of the pressures considered, since most polar solute molecules are preferentially solvated by the organic species up to ~80% CO_2 in CO_2-expanded MeOH, as was shown in Chapter 3. The equilibrium expression for DNP dissociation is given by Equation 6.2 and is used to calculate the proton concentration from spectra:

$$K_{DNP} = \frac{m_{H^+} m_{I^-} \gamma_{\pm}^{\ 2}}{m_{HI}} \qquad \text{Equation 6.2}$$

where K_{DNP} is the dissociation constant of DNP, m is the molal concentration in mol kg^{-1} and $\gamma_{\pm}$ is the activity coefficient of the charged species. The subscript HI denotes the protonated form of DNP, I^- refers to the basic form of DNP, and H^+ is the free proton

concentration. DNP concentrations were obtained by a modified form of the Beer-Lambert law (Equation 6.1):

$$\frac{m_{I^-}}{m_{HI}} = \frac{\varepsilon_{I^-} A_{I^-}}{\varepsilon_{HI} A_{HI}} \qquad \text{Equation 6.3}$$

where A is the absorption at the respective acidic or basic wavelength, but was taken as the area of the respective acid or base peak. ε is the molar absorptivity of the appropriate form determined by the method outlined in the previous section. In neat alcohols, all free protons result from DNP dissociation, so the charge balance is:

$$m_{H^+} = m_{I^-} \qquad \text{Equation 6.4}$$

A DNP mass balance provides a check for Equation 6.3 and is used to find individual concentrations needed for activity coefficient calculations and systems with ACAs.

$$m_{HI}^0 = m_{HI} + m_{I^-} \qquad \text{Equation 6.5}$$

where m_{HI}^0 is the initial DNP concentration. Activity coefficients of ionic species were calculated from the mean ionic activity coefficient determined from Pitzer's formula[16] shown in Equation 6.6. Activity coefficients of neutral species were assigned a value of unity. Ionic strength was found by Equation 6.7.

$$\ln \gamma_{\pm} = -A\left[\frac{\sqrt{I}}{1+1.2\sqrt{I}} + \frac{2}{1.2}\ln(1+1.2\sqrt{I})\right] \qquad \text{Equation 6.6}$$

$$I = \frac{1}{2}\sum_i m_i q_i^2 \qquad \text{Equation 6.7}$$

where A is the Debeye-Huckel parameter taken from Bradley and Pitzer,[17] I is the ionic strength of solution, and m_i and q_i are the molal concentration and charge of ionic species *i*. Activity coefficients and proton concentration are calculated via an iterative method involving the above equations. DNP dissociation constants (pK_{DNP}) in the solvents are provided in Table 6.1. The dissociation constants vary over several orders of magnitude between the different alcohols and an order of magnitude between water and the fastest alcohol, MeOH.

Effective dissociation constant of Alkylcarbonic acids

The equilibrium expressions for the formation and dissociation reactions are given by Equation 6.8 and Equation 6.9. The CO_2 term in the formation equilibrium is the fugacity to account for pressure and non-idealities.

$$K_1 = \frac{m_{ACA}}{m_{ROH} f_{CO_2}} \qquad \text{Equation 6.8}$$

$$K_{ACA} = \frac{m_{H^+} m_{ACA^-} \gamma_{\pm}^2}{m_{ACA}} \qquad \text{Equation 6.9}$$

where m_{ROH} and f_{CO2} are the molal concentrations of the alcohol and fugacity of CO_2, m_{ACA} and m_{ACA-} are the molal concentrations of the ACA and the carboxylate ion (conjugate base), respectively. The activity coefficient is calculated from Equation 6.6 and Equation 6.7 as described in the previous section. CO_2 and alcohol concentrations and liquid phase densities and liquid volumes were taken from the VLE data.[18,19] Carboxylate ion concentrations were determined from a charge balance, similar to Equation 6.4, but including the carboxylate ion concentration. The charge balance is

rearranged to Equation 6.10. This simplification uses DNP concentration ratio (R) and the initial DNP concentration (m_I^0).

$$m_{H^+} = m_{I^-} + m_{ACA^-} \qquad \text{Equation 6.10}$$

$$m_{I^-} = \frac{m_{I^0}}{1 + \frac{1}{R}} \qquad \text{Equation 6.11}$$

There are three unknowns in Equation 6.8 and Equation 6.9: K_1, K_a, and m_{ACA}, which leaves the system underspecified. An effective equilibrium constant, K_{eff}, can be formed by combining the formation and dissociation equations. The fugacity term was replaced to yield the applicable form:

$$K_{eff} = K_1 K_{ACA} = \frac{P_0 \cdot m_{H^+} m_{ACA^-} \gamma_{\pm}^2}{P \cdot \phi_{CO_2} m_{ROH} m_{CO_2}} \qquad \text{Equation 6.12}$$

where ϕ is the fugacity coefficient of CO_2 estimated by the Lee/Kesler correlation[20] and were within the range of 0.8 to 1, P is the pressure in bar, and P_0 is a reference pressure in bar. This equation eliminates the ACA concentration term and combines the two remaining equilibrium constants into one solvable term. Effective equilibrium constants provide insight into the relative strength of ACAs and can be used to calculate the proton concentration, which is important for catalysis and other pH-sensitive applications. Values for the three effective equilibrium constants are shown in Table 6.2. The relative trend of acid strength denoted by K_{eff} is MCA > ECA > BCA. This finding is consistent with the absorption spectra where increased CO_2 concentration has the largest impact on the absorption spectra in MeOH, less impact in EtOH, and minimal impact in BzOH. This also agrees with a pH-sensitive kinetic study[4, 5] that reported the following trend for acid strength: 1° > 2° > 3°.

Table 6.2: Equilibrium constants for the three alkylcarbonic acids. [a]Effective equilibrium constant determined via Equation 6.12. [b]Effective equilibrium constant determined by the product of K_1 and K_a.

	MCA	ECA	BCA
pK_{eff}[a]	8.97	10.1	12.4
pK_a	5.73	-	-
pK_1	3.21	-	-
pK_{eff}[b]	8.94	-	-

Separation of effective equilibrium constants

Effective equilibrium constants are important design tools that give information about the relative strength of ACAs; but dissociation constants compare ACAs to other acids. Processes using acids of similar pK_a can be redesigned around ACAs to take advantage of the tunable properties and environmental benefits. To overcome the degree-of-freedom problem discussed in the previous section, another equation must be used to solve for the dissociation constant. The ACA carboxylate concentration can be determined from a charge balance and exists in very small quantities; however, the ACA is formed in appreciable (~0.1 mM) amounts and can be estimated from an alcohol balance:

$$m_{ROH^0} = m_{ROH^L} + m_{ROH^{Vap}} + m_{ACA} + m_{ACA^-} \qquad \text{Equation 6.13}$$

where the superscripts *0*, *L*, and *Vap* denote the initial, liquid phase, and vapor phase concentrations of the alcohol. The liquid and vapor phase concentration are determined from an equation of state calculation. Equation 6.13 allows the calculation of the acidic

ACA species, which can be used in Equation 6.8 and Equation 6.9 to find the equilibrium constants.

This approach is sensitive to the precision of the equation of state calculation (or VLE data) and could introduce error since the initial, liquid phase, and vapor phase alcohol concentrations can be several orders of magnitude larger than the ACA concentration. The two equilibrium constants can be multiplied and compared to the effective equilibrium constant as a check. This technique was applicable for MCA, which has a pK_a of 5.73 which is in good agreement with a literature source[3]. This value and the formation constant, K_1, are shown in Table 6.2. The EtOH and BzOH spectra (Figure 6.3 and Figure 6.4) are less sensitive to CO_2 addition because the DNP dissociation constant is lower in these alcohols and the ACAs are weaker than MCA. This increases the uncertainty in the mass balance and leads to erroneous equilibrium constants. Consequently this technique is applicable only to acids similar in strength to MCA.

Conclusions

A spectroscopic technique is presented to study the formation and dissociation at 25°C of ACAs formed *in situ* in CO_2-expanded alcohols. ACAs are an interesting and green system because they offer tunable proton concentration and can be reversed by depressurization, thus eliminating neutralization and solid waste generation. The multiple ACA equilibria introduce a degree of freedom and hinder a straightforward pK_a measurement. An effective equilibrium constant was calculated for each ACA which is an assessment tool to compare the relative strength of ACAs. The effective constants ranged over several orders of magnitude with overall ACA performance in the order: MeOH > EtOH > BzOH. This demonstrates the tunability of ACAs systems and provides

a parameter that can be used to determine proton concentration and select operating conditions for an acid catalysis system.

An alcohol balance was used to remove the degree of freedom and separate the effective constant into formation and dissociation terms. This led to a pK_a of 5.73 for MCA, which is in good agreement with a reported value of 5.61. Attempts in ECA and BCA acids led to erroneous results brought on by uncertainty. Specifically the smaller DNP pK_a in EtOH and BzOH minimizes the effect of CO_2 on the absorption spectra and introduces error in the equilibrium expressions. The combined use with VLE data in the mass balances adds too much uncertainty for a reliable pK_a calculation. This study demonstrates the ability of spectroscopy to measure acid ionization constants in non-conventional media like GXLs. Future spectroscopic pK_a measurements of supercritical alcohols are important for biomass pretreatment and therefore an important design parameter.

References

1. Hallett, J. P.; Pollet, P.; Liotta, C. L.; Eckert, C. A., Reversible in situ catalyst formation. *Acc. Chem. Res.* **2008,** 41, (3), 458-467.

2. Chamblee, T. S.; Weikel, R. R.; Nolen, S. A.; Liotta, C. L.; Eckert, C. A., Reversible in situ acid formation for beta-pinene hydrolysis using CO2 expanded liquid and hot water. *Green Chem.* **2004,** 6, (8), 382-386.

3. Gattow, G.; Behrendt, W., Methyl hydrogen carbonate. *Angew. Chem., Int. Ed.* **1972,** 11, (6), 534-&.

4. West, K. N.; Wheeler, C.; McCarney, J. P.; Griffith, K. N.; Bush, D.; Liotta, C. L.; Eckert, C. A., In situ formation of alkylcarbonic acids with CO2. *J. Phys. Chem. A* **2001,** 105, (16), 3947-3948.

5. Weikel, R. R.; Hallett, J. P.; Liotta, C. L.; Eckert, C. A., Self-neutralizing in situ acid catalysts from CO2. *Topics in Catalysis* **2006,** 37, (2-4), 75-80.

6. Weikel, R. R.; Hallett, J. P.; Liotta, C. L.; Eckert, C. A., Self-neutralizing in situ acid catalysis for single-pot synthesis of iodobenzene and methyl yellow in CO2-Expanded methanol. *Ind. Eng. Chem. Res.* **2007,** 46, (16), 5252-5257.

7. Phan, L.; Chiu, D.; Heldebrant, D. J.; Huttenhower, H.; John, E.; Li, X. W.; Pollet, P.; Wang, R. Y.; Eckert, C. A.; Liotta, C. L.; Jessop, P. G., Switchable solvents consisting of amidine/alcohol or guanidine/alcohol mixtures. *Ind. Eng. Chem. Res.* **2008,** 47, 539-545.

8. Xiang, T.; Johnston, K. P., Acid-base behavior of organic-compounds in supercritical water. *J. Phys. Chem.* **1994,** 98, (32), 7915-7922.

9. Ryan, E. T.; Xiang, T.; Johnston, K. P.; Fox, M. A., Absorption and fluorescence studies of acridine in subcritical and supercritical water. *J. Phys. Chem. A* **1997,** 101, (10), 1827-1835.

10. Chlistunoff, J.; Ziegler, K. J.; Lasdon, L.; Johnston, K. P., Nitric/nitrous acid equilibria in supercritical water. *J. Phys. Chem. A* **1999,** 103, (11), 1678-1688.

11. Xiang, T.; Johnston, K. P.; Wofford, W. T.; Gloyna, E. F., Spectroscopic measurement of pH in aqueous sulfuric acid and ammonia from sub- to supercritical conditions. *Ind. Eng. Chem. Res.* **1996,** 35, (12), 4788-4795.

12. Minami, K.; Suzuki, T.; Aizawa, T.; Sue, K.; Arai, K.; Smith, R. L., Proton concentration of supercritical water and high-concentrated carbon dioxide mixture using UV-vis spectroscopy. *Fluid Phase Equilib.* **2007,** 257, (2), 177-182.

13. Park, S. N.; Kim, C. S.; Kim, M. H.; Lee, I. J.; Kim, K., Spectrophotometric measurement of the first dissociation constants of carbonic acid at elevated temperatures. *J. Chem. Soc.-Faraday Trans.* **1998,** 94, (10), 1421-1425.

14. Park, S. N.; Kim, H.; Kim, K.; Lee, J. A.; Lho, D. S., Spectroscopic measurement of the acid dissociation constant of 2-naphthol and the second dissociation constant of carbonic acid at elevated temperatures. *Phys. Chem. Chem. Phys.* **1999,** 1, (8), 1893-1898.

15. Kim, M. H.; Kim, C. S.; Lee, H. W.; Kim, K., Temperature dependence of dissociation constants for formic acid and 2,6-dinitrophenol in aqueous solutions up to 175 degrees C. *J. Chem. Soc.-Faraday Trans.* **1996,** 92, (24), 4951-4956.

16. Silvester, L. F.; Pitzer, K. S., Thermodynamics of electrolytes .8. high-temperature properties, including enthalpy and heat-capacity, with application to sodium-chloride. *J. Phys. Chem.* **1977,** 81, (19), 1822-1828.

17. Bradley, D. J.; Pitzer, K. S., Thermodynamics of electrolytes .12. dielectric properties of water and debye-huckel parameters to 350°C and 1-kbar. *J. Phys. Chem.* **1979,** 83, (12), 1599-1603.

18. Chang, C. J.; Day, C. Y.; Ko, C. M.; Chiu, K. L., Densities and P-x-y diagrams for carbon dioxide dissolution in methanol, ethanol, and acetone mixtures. *Fluid Phase Equilib.* **1997,** 131, (1-2), 243-258.

19. Chen, J. T.; Lee, M. J., Vapor-liquid equilibria for benzyl alcohol with carbon dioxide, ethane, or nitrogen at elevated pressures. *Fluid Phase Equilib.* **1997,** 130, (1-2), 231-242.

20. Lee, B. I.; Kesler, M. G., Generalized thermodynamic correlation based on 3-parameter corresponding states. *Aiche J.* **1975,** 21, (3), 510-527.

CHAPTER 7: CONCLUSIONS AND RECOMMENDATIONS

Local Compositions in Gas-Expanded Liquids

In this work, a synergistic study of high-pressure spectroscopy and MD simulations was used to study steady-state solvation of Coumarin 153 in the ground and excited states. A technique based on solvent and solute characteristics was developed to estimate local compositions from spectral maxima. This showed improvement over the commonly-used linear estimation technique which would have overestimated MD simulation predictions in this study. MD simulations provided atomic-level information that spectroscopy cannot probe and served as a direct comparison to the experimental local compositions.

The simulations and experiments agreed in ground state solvation, but did not agree in excited-state solvation. 3D distribution functions, or solvent maps, provided insight into this disparity. A consequence of C153 excitation is increased solvation by CO_2 and the organic species. Organic solvation was localized to small areas near the polar functional groups, while CO_2 was distributed uniformly around C153. This dilutes the organic enhancement and predicts erroneous local compositions. Fluorescence spectroscopy is related to the solvation energy and could be dominated by polar solvent molecules. Absorption maxima were very similar to the maxima in neat organic liquids at CO_2 compositions up to 80%. This indicates preferential solvation, but shows the composition ranges where GXLs are behave like the organic component and is a recurring theme throughout this thesis.

Solvent and Solvation Dynamics in Gas-Expanded Liquids

Solvation is an important process that can impact chemical processes. This study demonstrates the importance of preferential solvation and further highlights the applications of tunable solvent properties. MD simulations are an alternative method to experimental techniques like time-resolved fluorescence spectroscopy and give atomic-level insight to the reorganization process. GXLs display composition-dependent solvent rotations and solvation timescales that result from intermolecular interactions and bulk properties like polarity and viscosity. This study shows that GXLs are a versatile medium for fast chemical processes and are advantageous over neat organic liquids. Future studies should use this information to study a process that is dependent on solvation. Numerous examples are available in the literature, but electron transfer polymerizations are promising and could be performed in this lab.

GXLs are an attractive medium for polymerizations because the tunable solvation dynamics can be used to control molecular weight distribution.[1] Electron transfer polymerizations use organometallic catalysts to cleave an alkyl halide bond and generate alkyl and halide radicals. The halide can complex with the metal or accept an electron and remain in solution as an ion. The metal-halide complex can deactivate the radical and cease polymerization by the reverse process. The ratio of activation to deactivation rates is dependent on the solvent and its ability to solvate the halide ion and facilitate electron transfer from the metal complex to the halide radical. MeOH and acetone have slower response rates than their respective GXLs because of preferential solvation and enhanced transport. Halide solvation could be faster in GXLs; therefore, yielding better molecular weight control and facilitating downstream separation by GAS precipitation or venting

CO_2. This chapter provides the necessary information to select solvents and the appropriate operating conditions to obtain the optimal molecular weight distribution.

Effects of Solvent Structure on Solvatochromism in Gas-Expanded Liquids

This work links the two analytical techniques in this thesis, solvatochromism and MD simulations, with structure-property relationships. The solutes were very similar in structure, a single aromatic ring with different numbers and placements of nitrogen atoms; but displayed very different absorption spectra and solvent interactions. An interesting feature of the solutes is the range of dipole moments and interactions with the solvent components. Dipole moments ranged from a net dipole of zero like benzene and pyrazine, to the very large moment of pyridazine. Higher order moments are also present. Solvent-solute interactions that influence spectroscopy include Van der Waals interactions, as seen in benzene solvatochromism, hydrogen bonds between nitrogen and MeOH, and Lewis acid/base interactions between nitrogen and CO_2. Each of these interactions and the solute dipole moment impact the spectra and are sensitive to local solvent structure and composition.

Absorption spectra are unique to the individual solutes and the types of interactions with the two solvent species. Both red and blue shifts are observed, and the synergistic approach used in this study provides insight to the mechanism. Except for benzene, lone pair electrons on the nitrogen are delocalized into the aromatic ring upon excitation; and solvents that interact with the nitrogen hinder delocalization and cause a blue shift. A surprising revelation was the observed blue shift of pyridine, pyrazine, and 1,3,5 triazine when CO_2 was added to MeOH. CO_2 molecules displaced the strongly interacting MeOH molecules and caused a blue shift relative to neat MeOH. The

observed red shift in the pyridazine case was attributed to weakened CO_2 interaction at higher CO_2 composition.

The computational results supported these findings and provided a detailed visualization of the complex micro-environment surrounding the solutes. 1D RDFs reveal concentration-dependent structural information that affects solvatochromism. 3D distribution functions show that CO_2 and MeOH form intricate solvation patterns around the solutes. ADFs provide better spatial resolution and highlight features in the RDFs. 3D imaging gives a better understanding of solvation and solvatochromism and is a viable structural analysis technique that is applicable to other complex systems.

Spectroscopic Measurements of Alkylcarbonic Acid Dissociation

This project presents a novel spectroscopic method to measure the pK_a of ACAs which form *in situ* by the reversible reaction of CO_2 and an alcohol under pressure. ACAs have been used as acid catalysts and polarity switches, but the dissociation is unknown because of multiple equilibrium reactions and the high pressure nature. Effective equilibrium constants, the product of the formation and dissociation constants, were measured in MCA, ECA, and BCA. This parameter indicates the relative acid strength of the ACAs and is a selection parameter for choosing an ACA.

Alcohol material balances were used to remove a degree of freedom and solve for the independent association and dissociation constants. Unfortunately this technique only worked for MCA. The formation and dissociation constants for ECA and BCA are too small and add uncertainty to the spectral analysis. MCA's pK_a is 5.8 at 25°C which is similar to a literature value[2] of a similar CO_2/MeOH system. The pK_a is slightly lower than carbonic acid's pK_a and is consistent with kinetic data.[3] This study highlights the

pressure-tunable acid concentrations that GXLs offer and provides information that can be used to design a chemical process like an acid catalyzed reaction.

Future Directions

GXLs have tremendous opportunity in the chemical industry because of the environmental and economical benefits. This thesis provides a molecular-scale understanding of GXLs that can be applied to real applications like separations, extractions, and reactions. The work in this thesis is complete and does not require ongoing work from a successor, but there are exciting opportunities that can take advantage of the fundamental information presented here.

Chapters 3 and 5 focus on steady state solvation patterns around solute molecules and the effect on spectroscopy. The spectroscopic techniques and MD simulation analysis techniques could be applied to any other solvent system to obtain a fundamental understanding of molecular interactions in these solvent systems. Examples in this laboratory include designer solvents like piperylene sulfone and reversible ionic liquids. There are several broad-scale applications that could serve several industries, most notably the pharmaceutical and oil and gas industries. The most attractive use for GXLs is GAS crystallization, and investigating optimal solvents and conditions to selectively precipitate molecules (i.e. products or catalysts) is applicable to nanomaterials processing, homogeneous catalyst recovery and recycle, and crystallization. Solute solubility is dependent on interactions with the solvent; therefore, exploring the cybotactic region would allow researchers to design a solvent for a particular GAS separation scheme. Enhanced oil recovery is a technique used to extract crude oil from a drilling well. When CO_2 is added to the well, the crude viscosity decreases and is easier

to process; however, this causes asphaltine molecules to precipitate which leads to scaling and processing problems. Opportunities exist in both chemistry and engineering. A study similar to this could provide information about solvent-asphaltine interactions and different additives or the appropriate operating conditions could be developed to prevent precipitation.

The solvation dynamics work presented in Chapter 4 provides many opportunities for controlled chemistry. As mentioned in the chapter, solvent dynamics affect ultrafast chemistries like nanomaterial behavior and electron-transfer polymerizations, and the results from this study provide insight into solvent selection for these applications. These applications can be strongly coupled to the solvent environment and their performance can be hindered or enabled by changing this variable. A GXL can be tuned from organic-like to gas-like properties, which allows control over nano-device performance or polymer molecular-weight control. A successor could use GXLs as a medium for the polymerization reaction described in this chapter to control molecular weight distribution by adjusting the CO_2 composition.

The techniques to measure dissociation constants of ACAs offer immediate opportunities for a new graduate student to learn about GXLs, UV/vis spectroscopy, and high-pressure systems. The work presented in this chapter studies only three alcohol/CO_2 systems at one temperature. Other alcohols and temperatures should be explored to complete the ACA study. Once this is known, other acid catalyzed reactions and pH-sensitive chemistries could be explored with this new information.

References

1. Braunecker, W. A.; Matyjaszewski, K., Recent mechanistic developments in atom transfer radical polymerization. *J. Mol. Cat. A* **2006,** 254, (1-2), 155-164.

2. Gattow, G.; Behrendt, W., Methyl hydrogen carbonate. *Angew. Chem., Int. Ed.* **1972,** 11, (6), 534-&.

3. Weikel, R. R.; Hallett, J. P.; Liotta, C. L.; Eckert, C. A., Self-neutralizing in situ acid catalysis for single-pot synthesis of iodobenzene and methyl yellow in CO2-Expanded methanol. *Ind. Eng. Chem. Res.* **2007,** 46, (16), 5252-5257.

APPENDIX A: SOLVENT MAPS FOR CHAPTER 3

Parts a&c are plane that are coplanar to the C153 molecule. Vertical line through the probe molecule represents the sample plane used in parts b&d to show solvent accumulation above and below the C153 plane. Tick marks are spaced ~3Å.

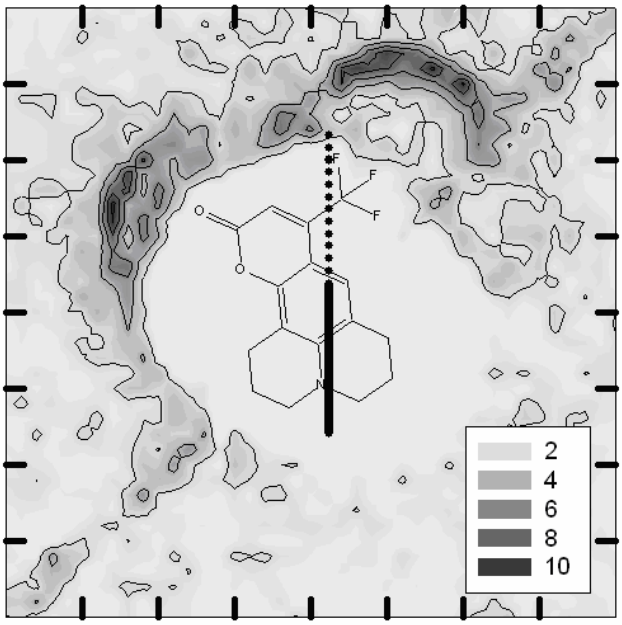

a

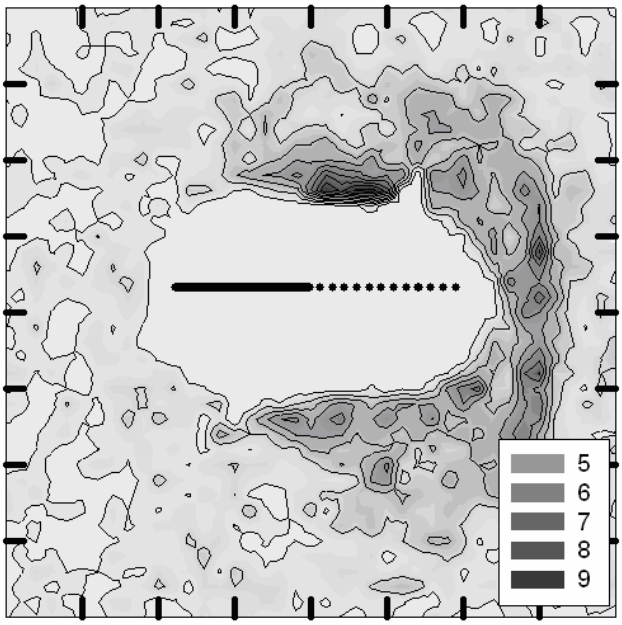

b

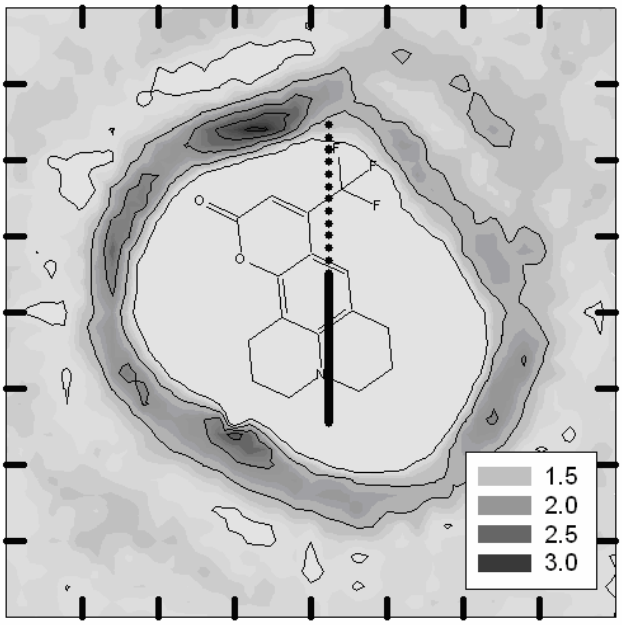

c

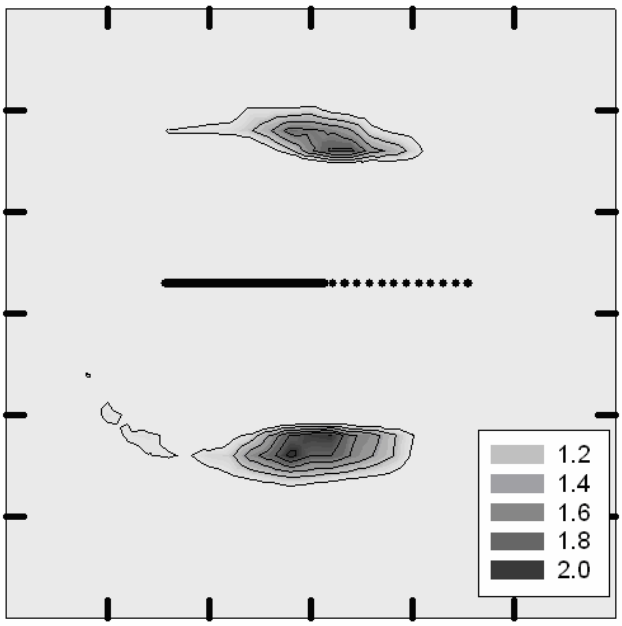

d

Figure A.1: Axial distribution functions relative to ground-state C153 in a 2% MeOH GXL. (a&b) MeOH and (c&d) CO_2 clustering around the C153 probe.

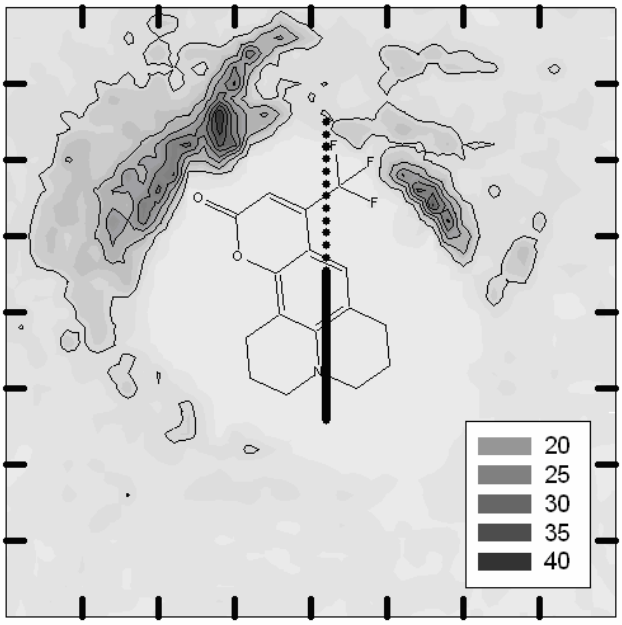

a

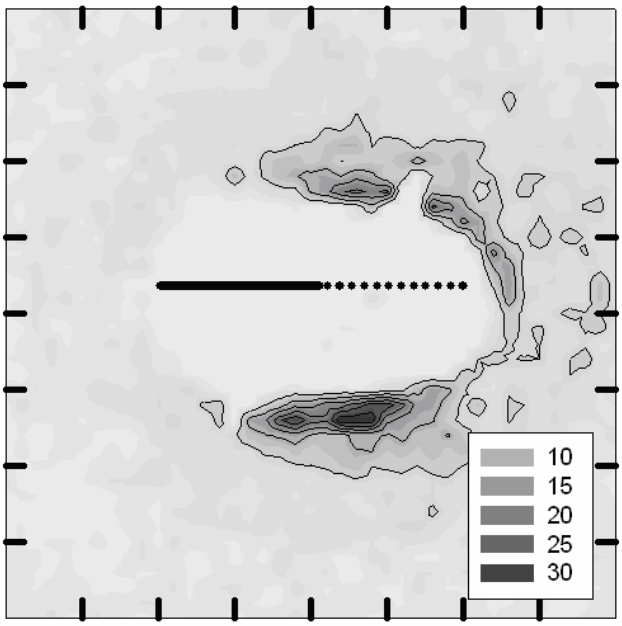

b

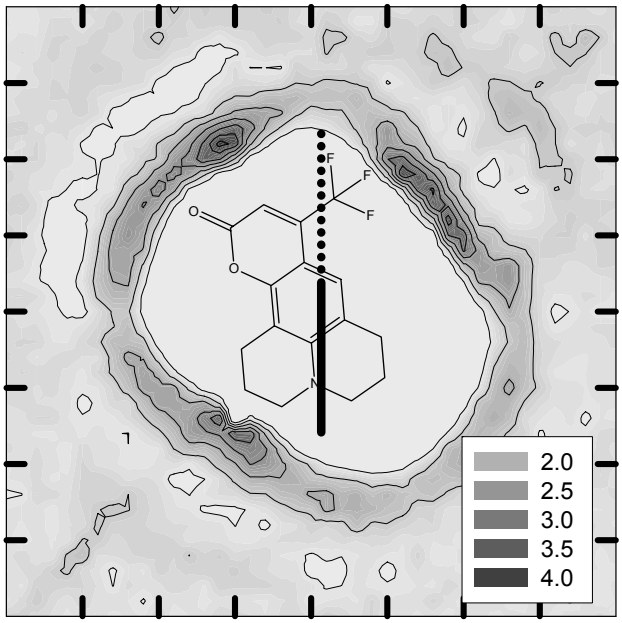

c

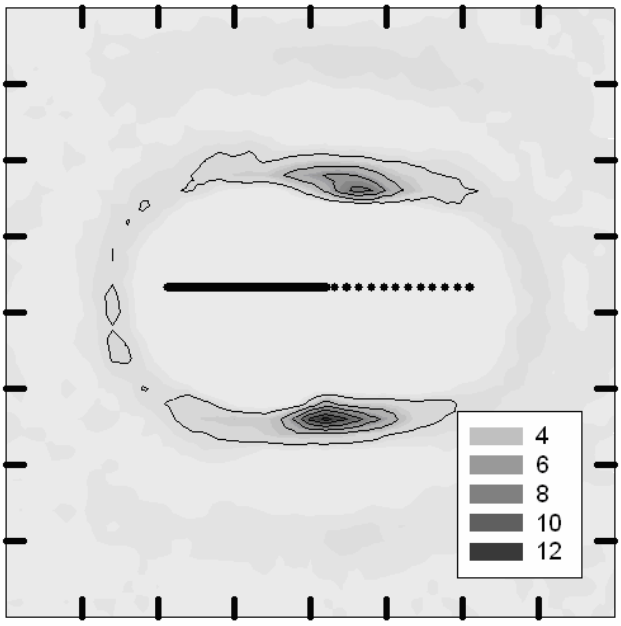

d

Figure A.2: Axial distribution functions relative to excited-state C153 in a 2% MeOH GXL. (a&b) MeOH and (c&d) CO_2 clustering around the C153 probe.

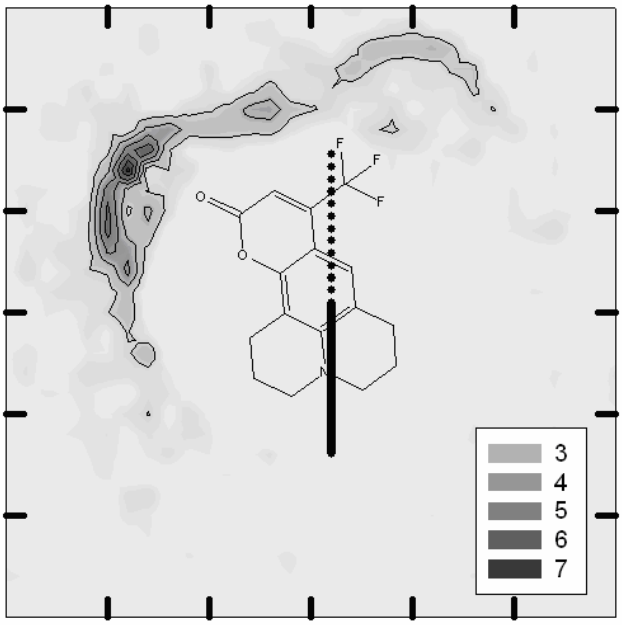

a

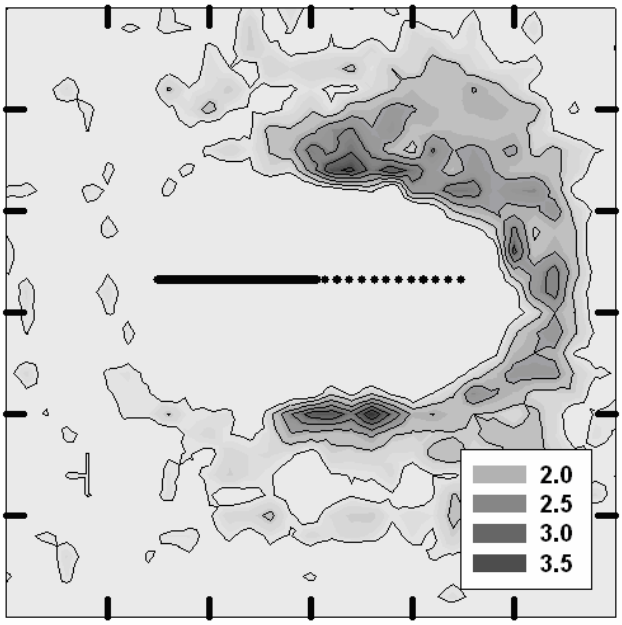

b

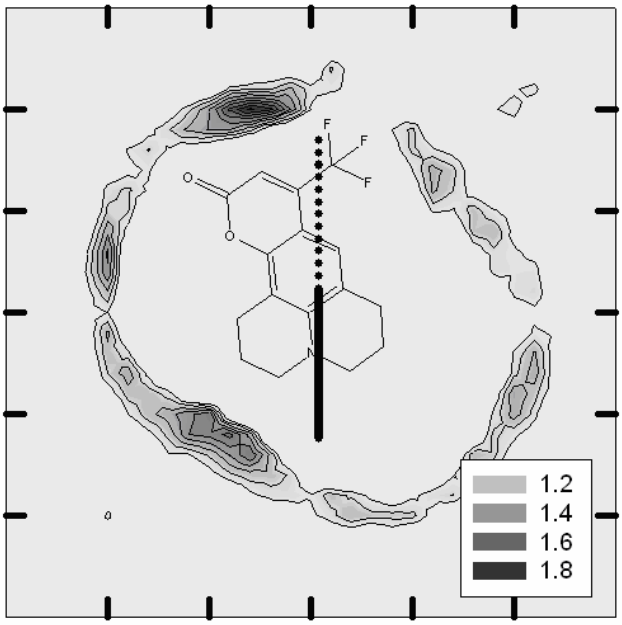

c

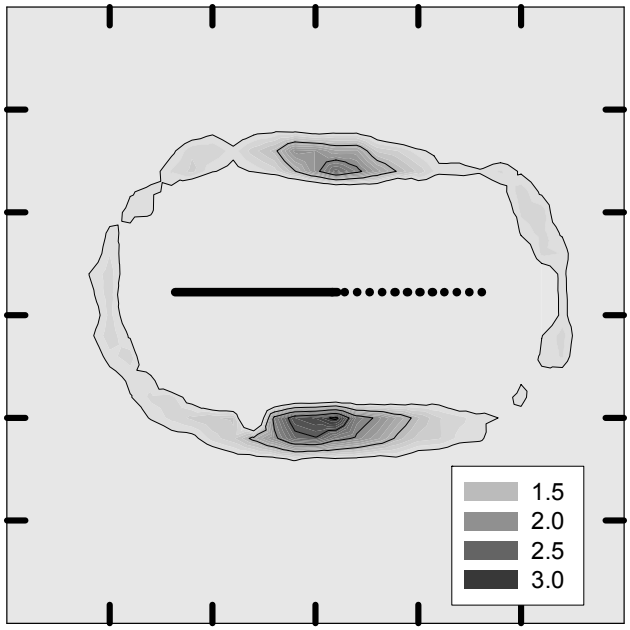

d

Figure A.3: Axial distribution functions relative to ground-state C153 in a 5% MeOH GXL. (a&b) MeOH and (c&d) CO_2 clustering around the C153 probe.

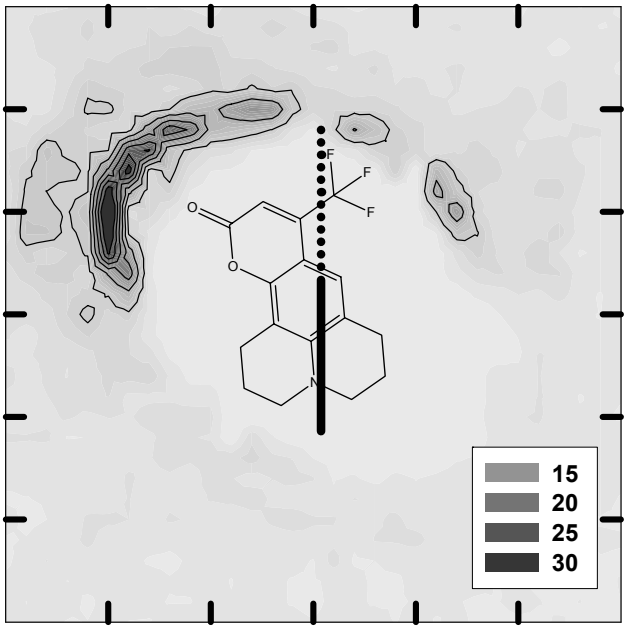

a

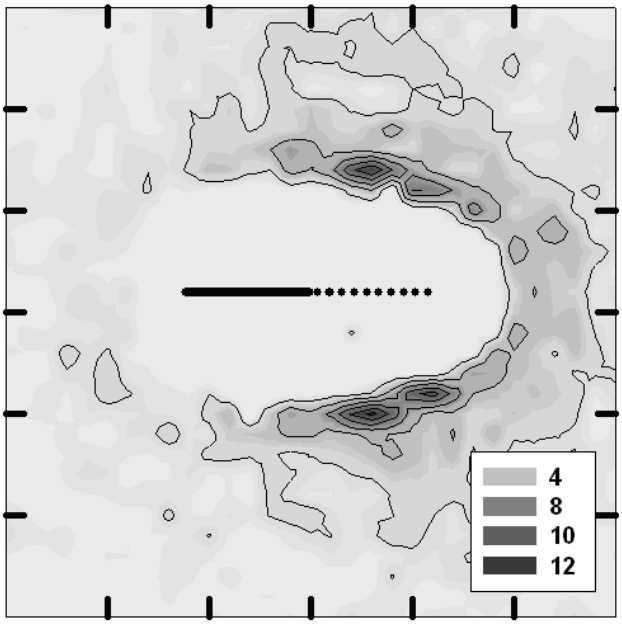

b

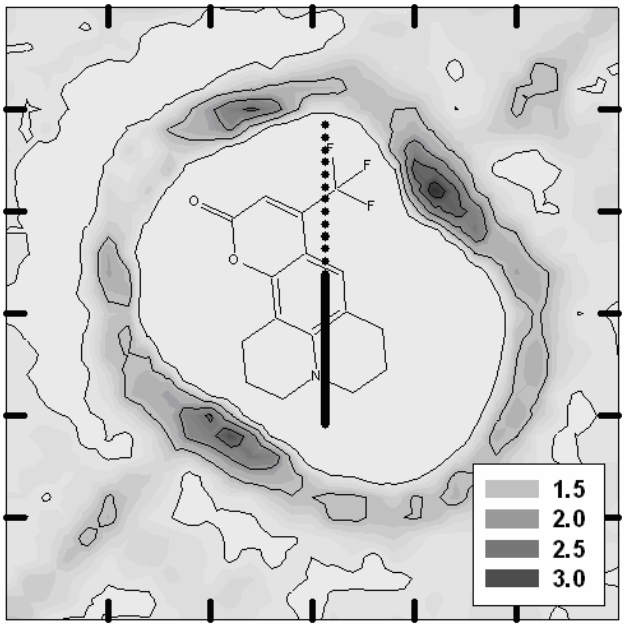

c

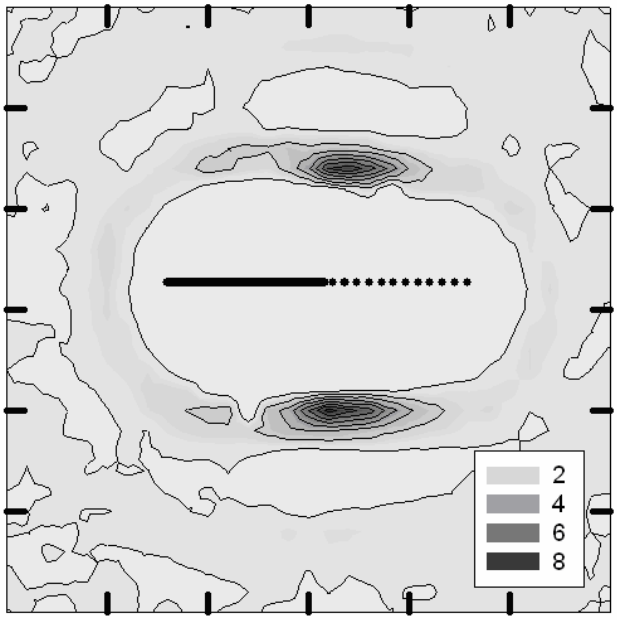

d

Figure A.4: Axial distribution functions relative to excited-state C153 in a 5% MeOH GXL. (a&b) MeOH and (c&d) CO_2 clustering around the C153 probe.

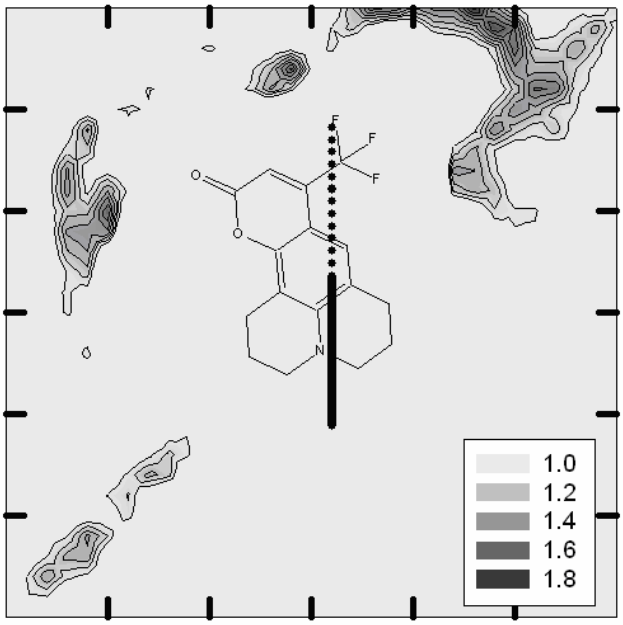

a

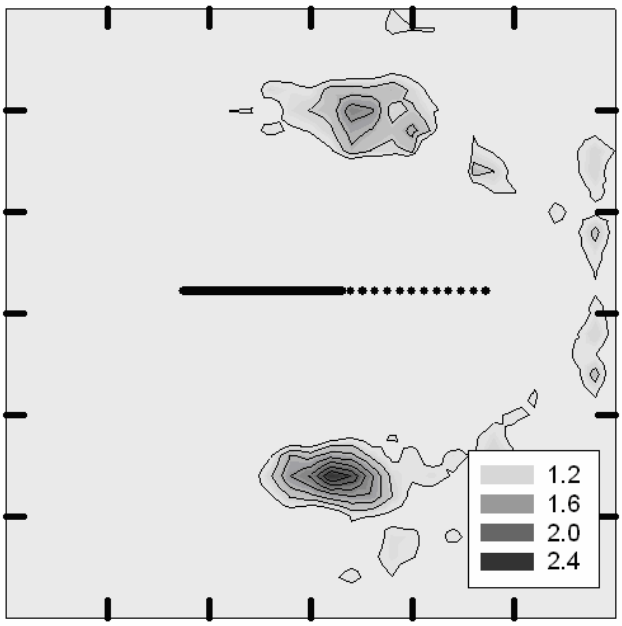

b

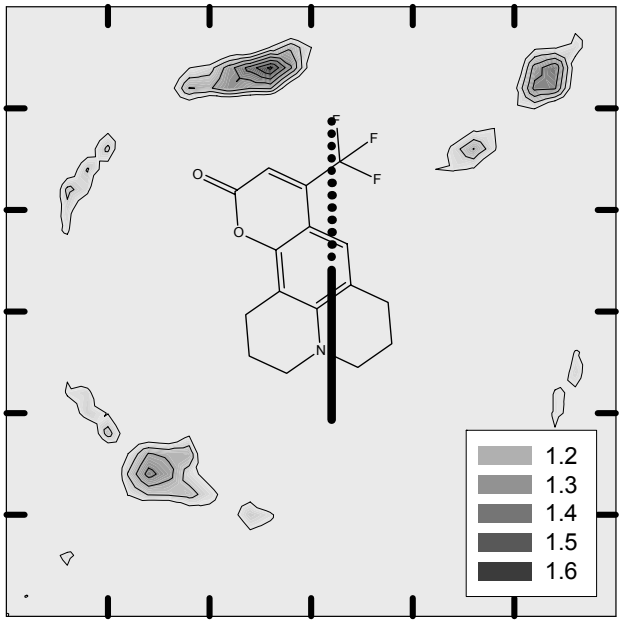

c

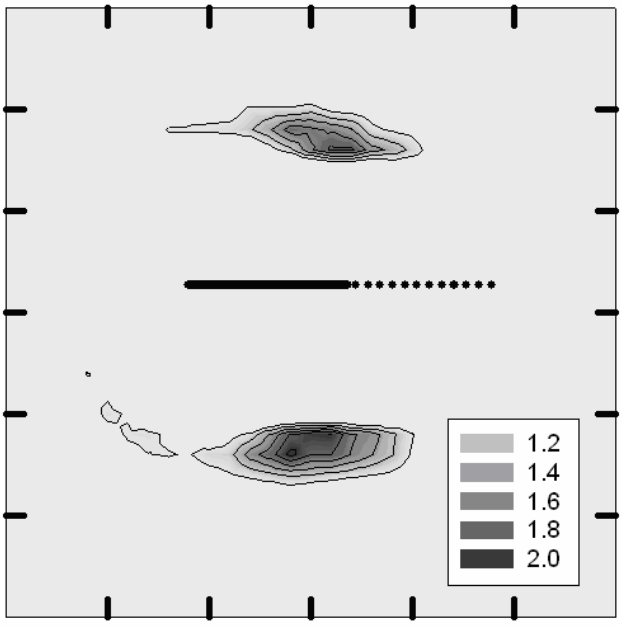

d

Figure A.5: Axial distribution functions relative to ground-state C153 in a 20% MeOH GXL. (a&b) MeOH and (c&d) CO_2 clustering around the C153 probe.

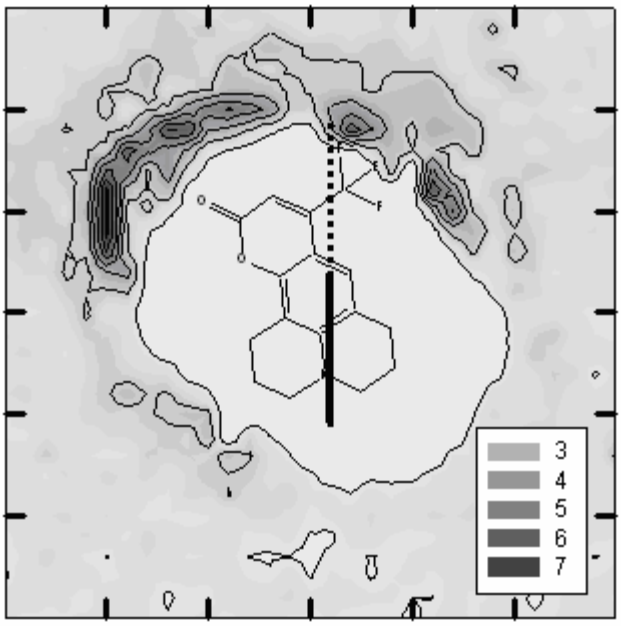

a

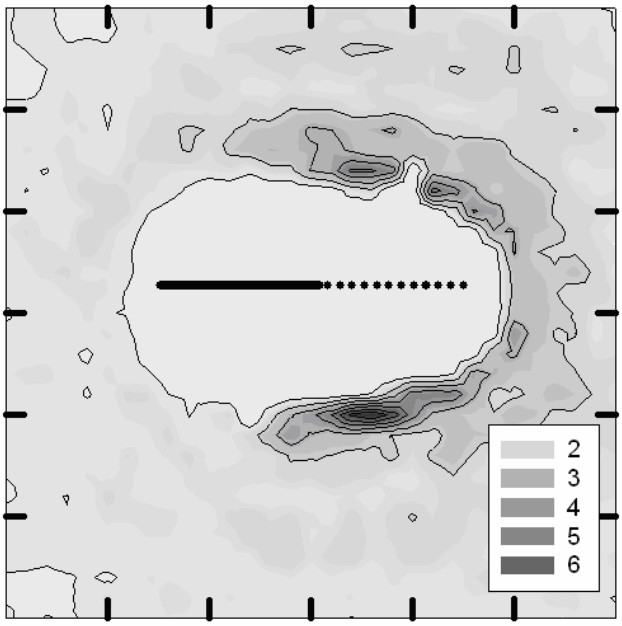

b

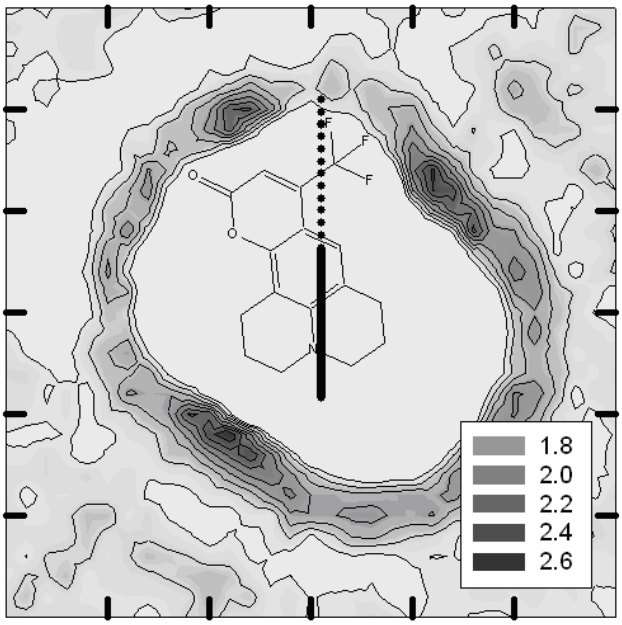

c

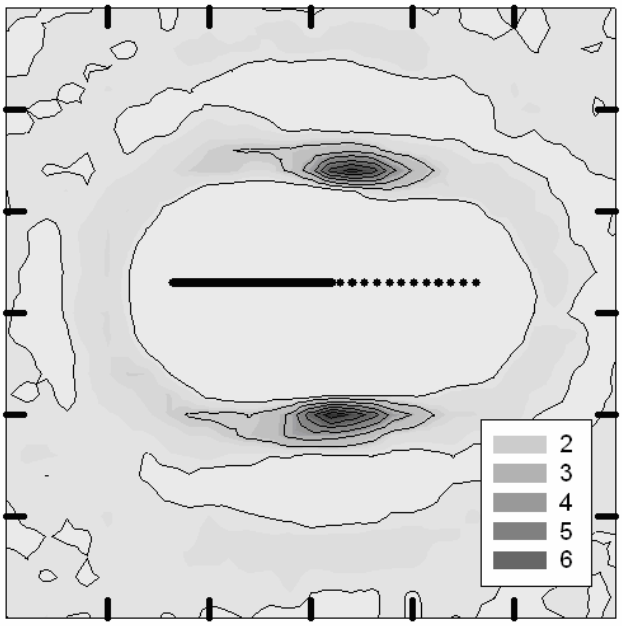

d

Figure A.6: Axial distribution functions relative to excited-state C153 in a 20% MeOH GXL. (a&b) MeOH and (c&d) CO_2 clustering around the C153 probe.

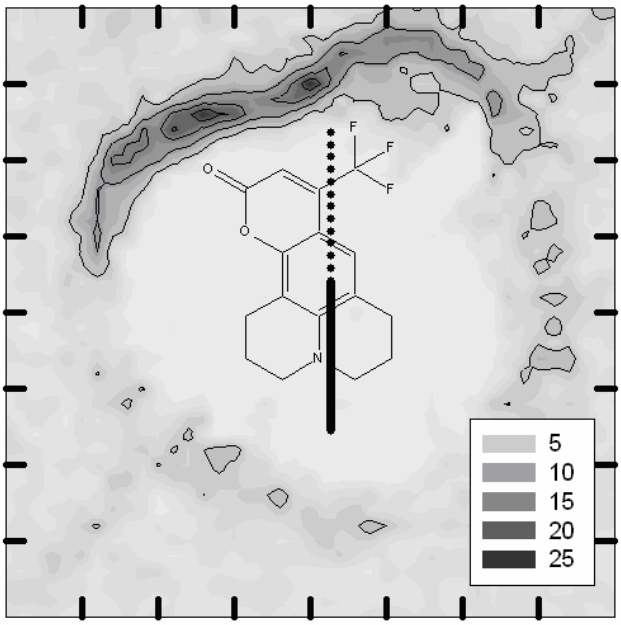
F
F
F
O
O
N
5
10
15
20
25

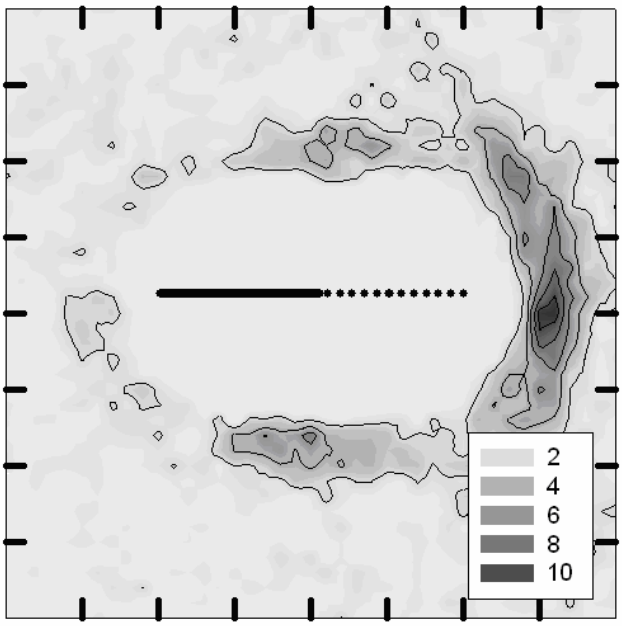
2
4
6
8
10

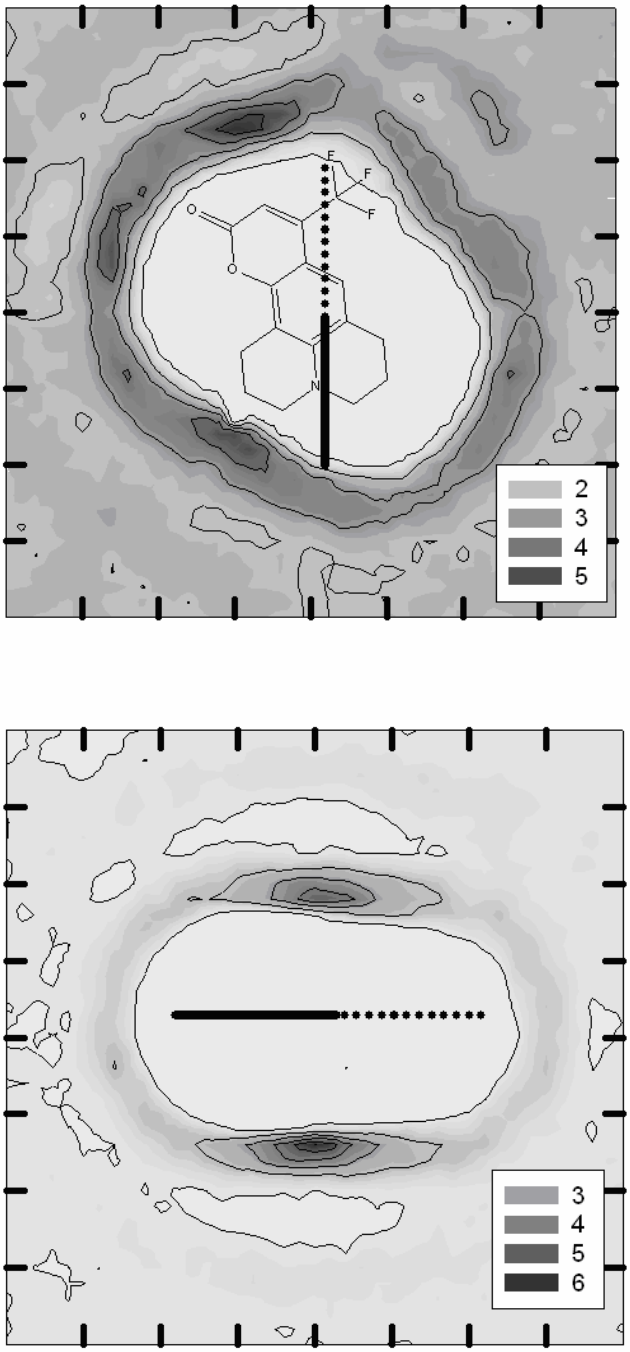

Figure A.7: Axial distribution functions at two different vantage points around ground-state C153 in a 2% acetone GXL. Scale represents values of the ADF for (a&b) Acetone and (c&d) CO_2 clustering around C153.

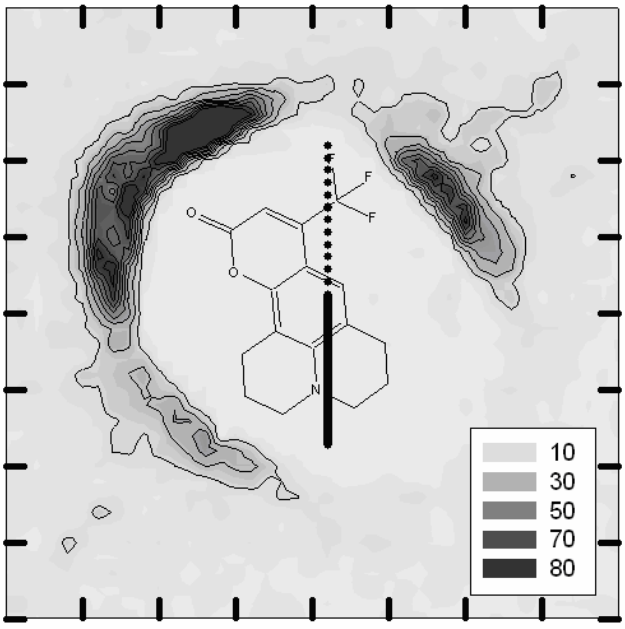
F
F
F
O
O
N
10
30
50
70
80

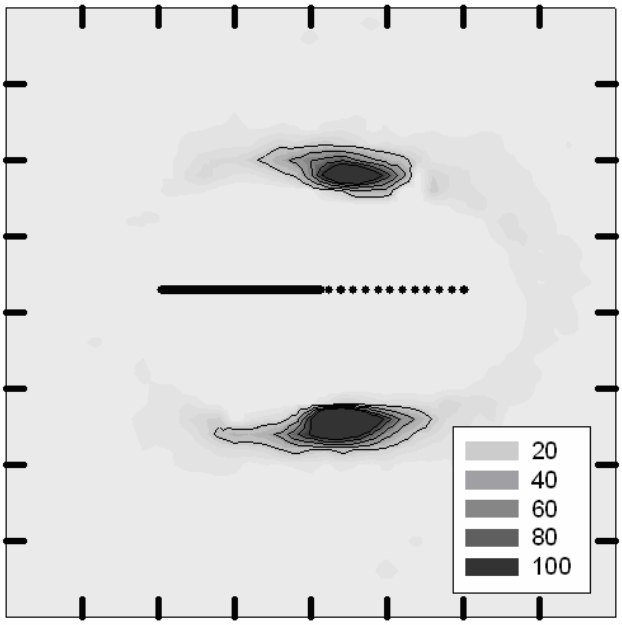
20
40
60
80
100

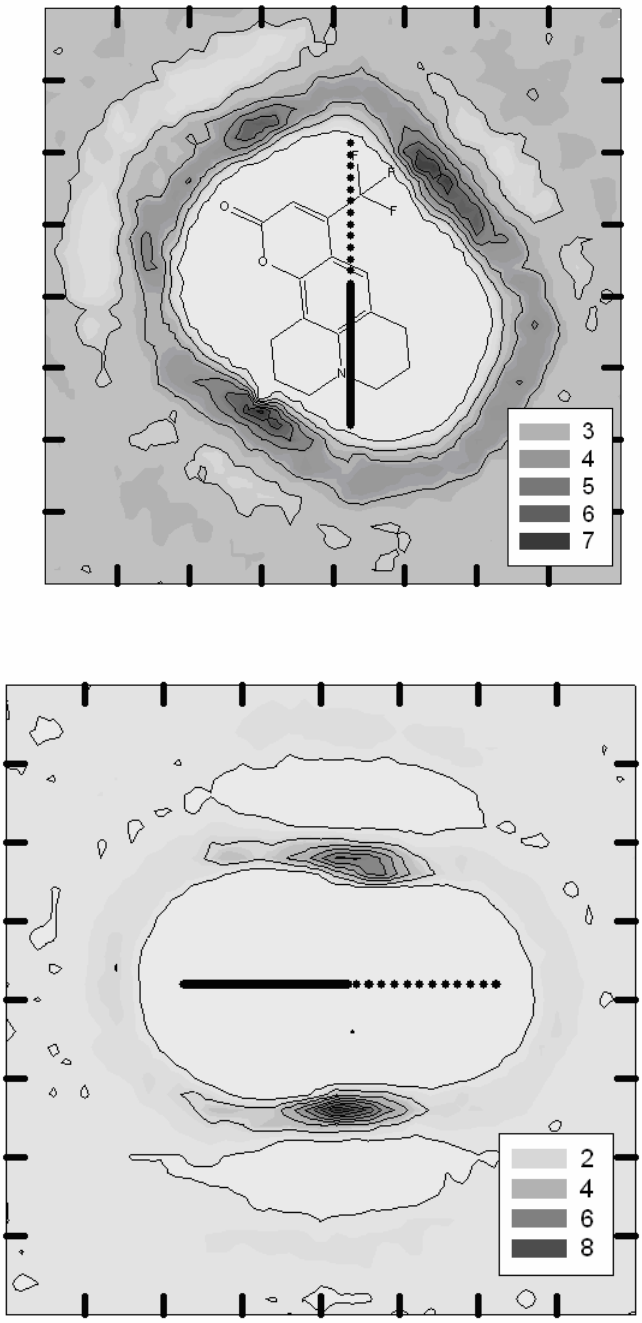

Figure A.8: Axial distribution functions relative to excited-state C153 in a 2% acetone GXL. (a&b) Acetone and (c&d) CO_2 clustering around the C153 probe.

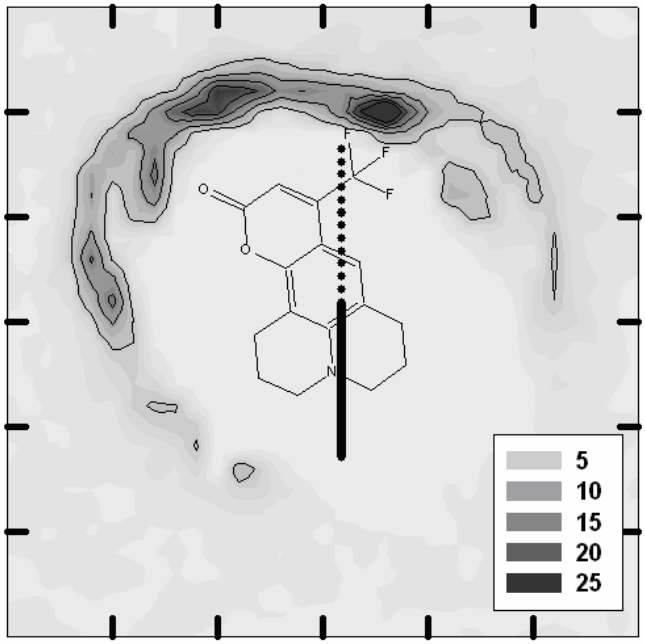
F
F
O
O
N
5
10
15
20
25

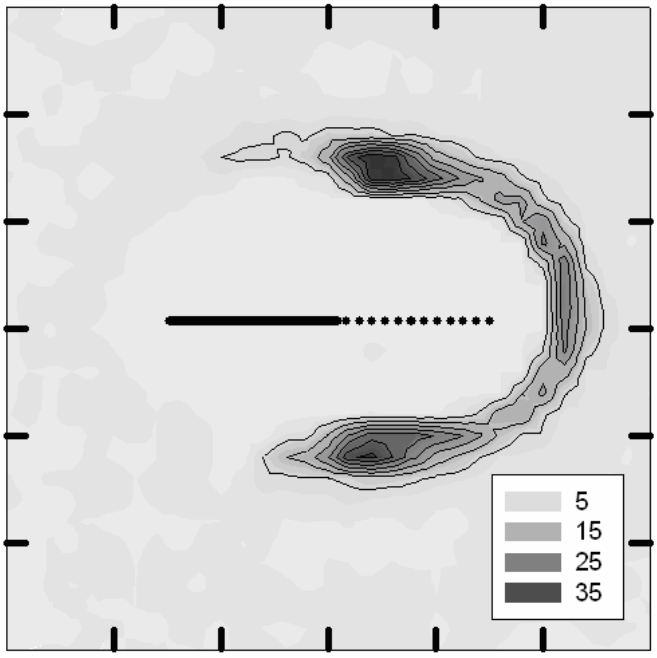
5
15
25
35

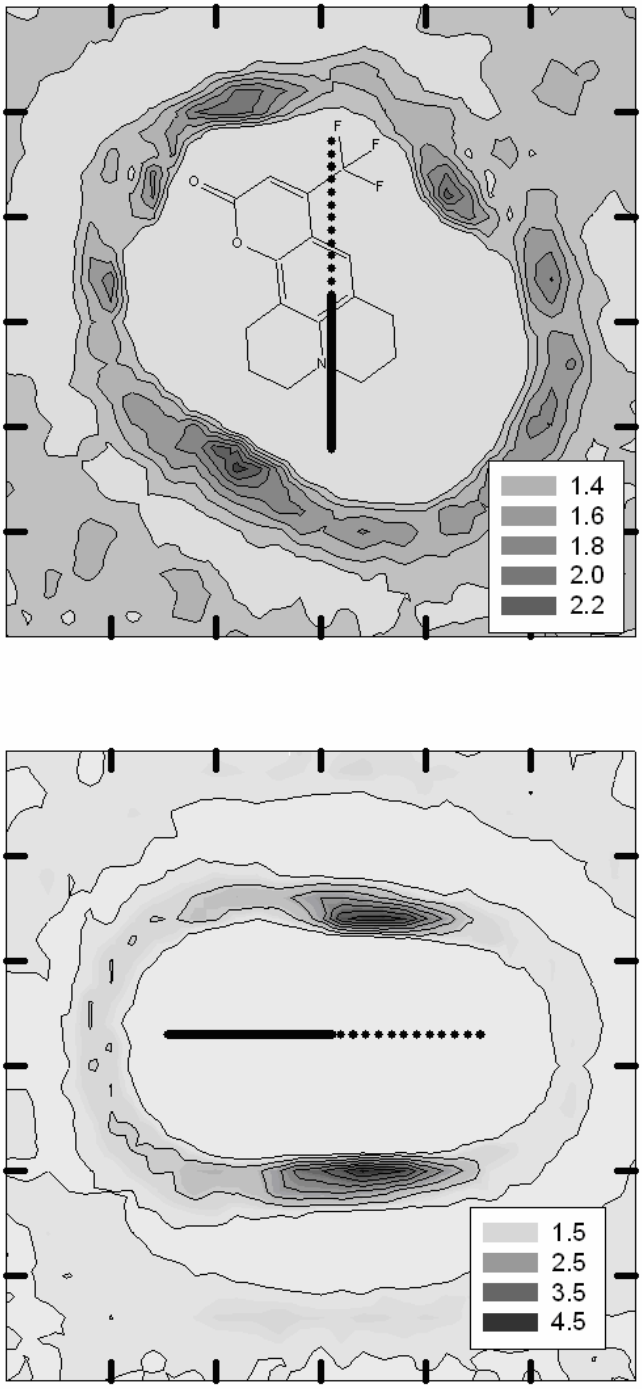

Figure A.9: Axial distribution functions relative to excited-state C153 in a 5% acetone GXL. (a&b) Acetone and (c&d) CO_2 clustering around the C153 probe.

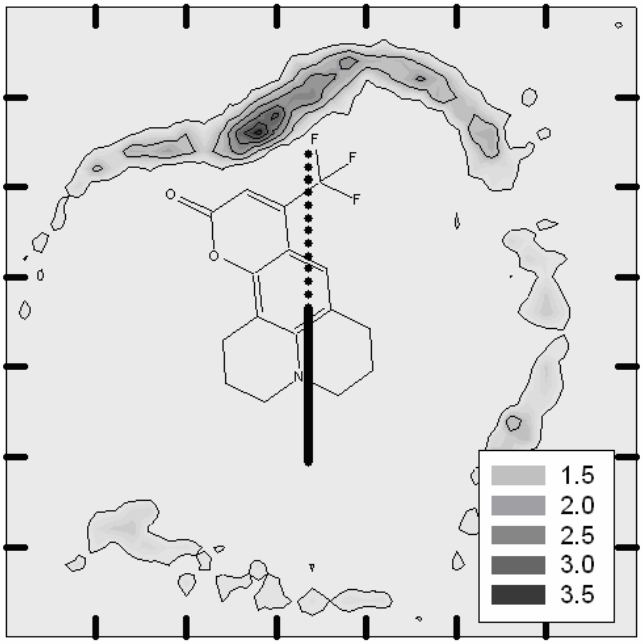
F
F
F
O
N
1.5
2.0
2.5
3.0
3.5

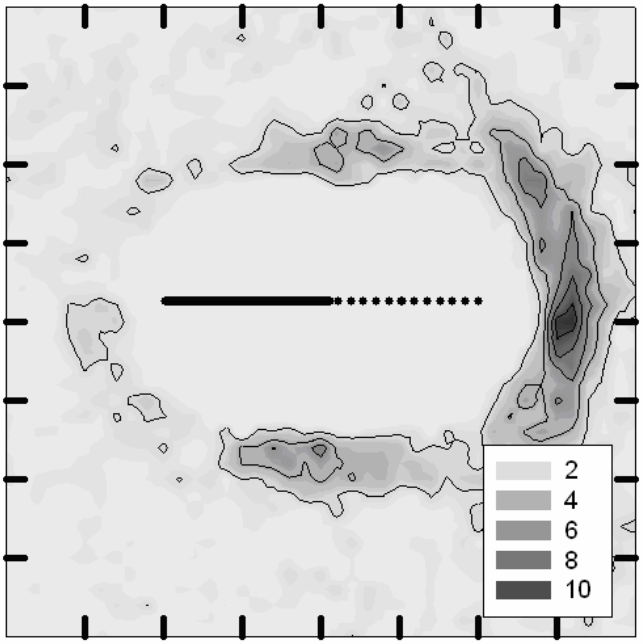
2
4
6
8
10

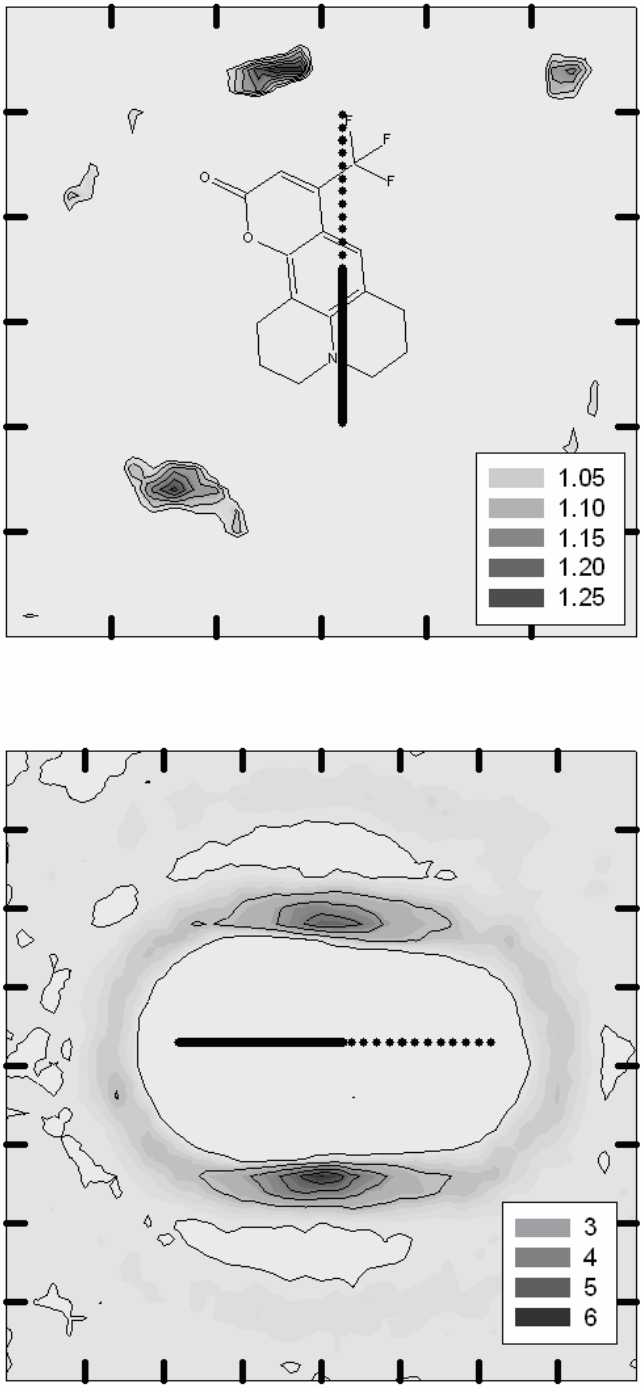

Figure A.10: Axial distribution functions relative to ground-state C153 in a 20% acetone GXL. (a&b) Acetone and (c&d) CO_2 clustering around the C153 probe.

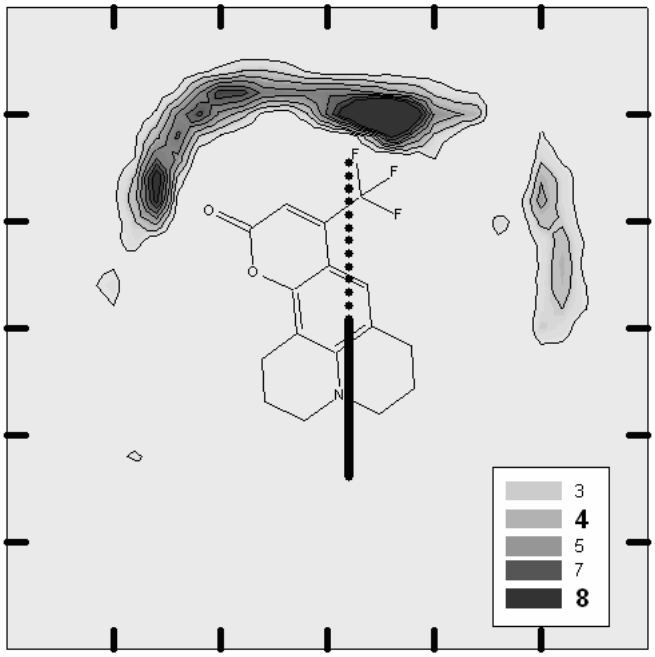
F
F
F
O
O
N
3
4
5
7
8

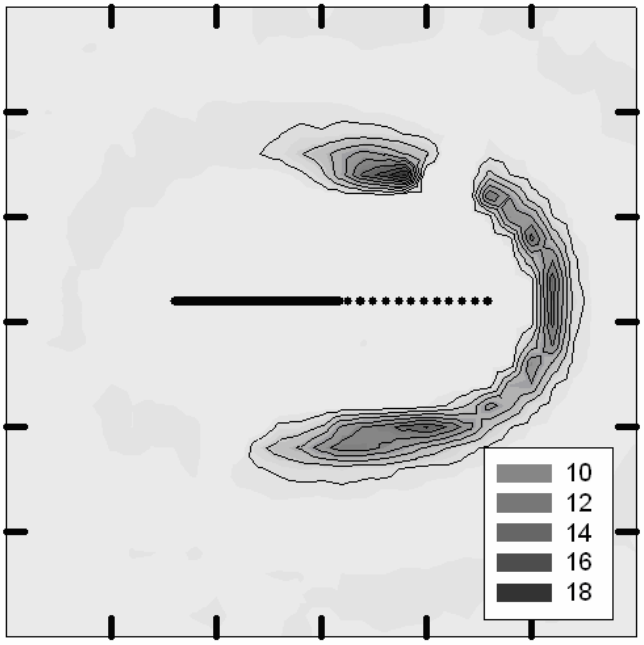
10
12
14
16
18

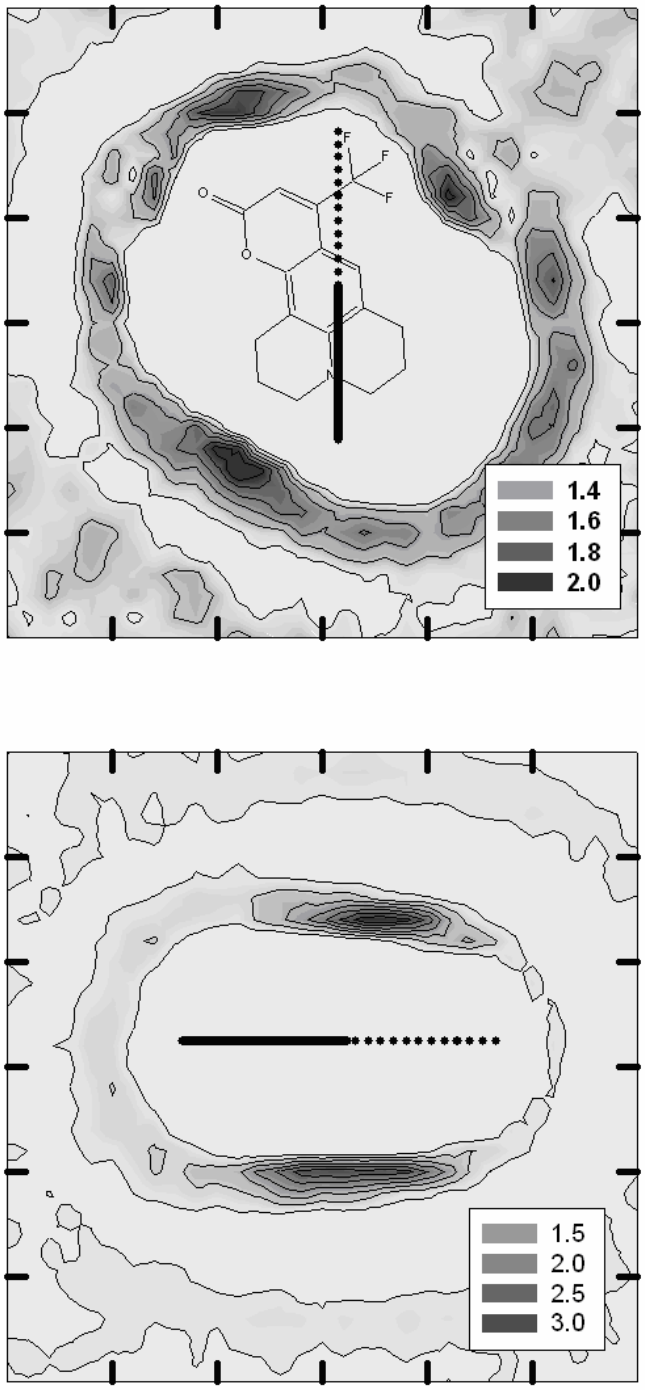

Figure A.11: Axial distribution functions relative to excited-state C153 in a 20% acetone GXL. (a&b) Acetone and (c&d) CO_2 clustering around the C153 probe.

APPENDIX B: ROTATIONAL CORRELATION FUNCTIONS AND FITTING PARAMETERS FOR CHAPTER 4

This appendix contains RCFs that were referenced in Chapter 4 and the fitting parameters used to fit Equation 4.4 to RCF data (also referenced in Chapter 4).

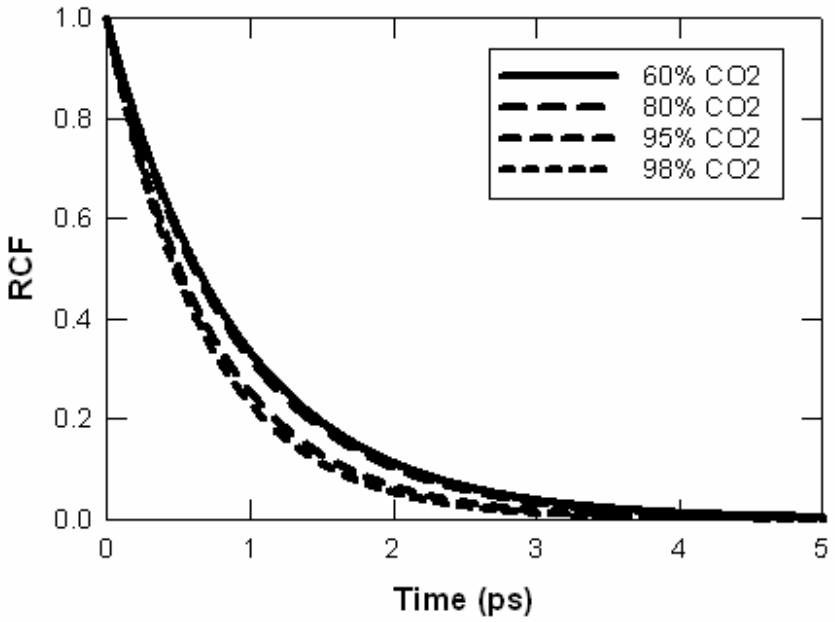

Figure B.1: First-order CO_2 RCFs in several acetone GXLs (SRF case).

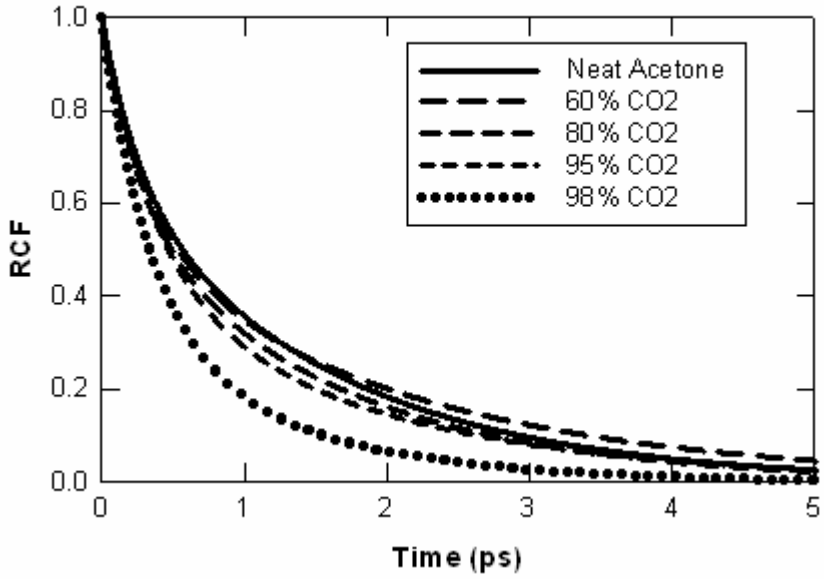

Figure B.2: First-order acetone RCFs along the C-O bond vector in acetone GXLs (SRF case).

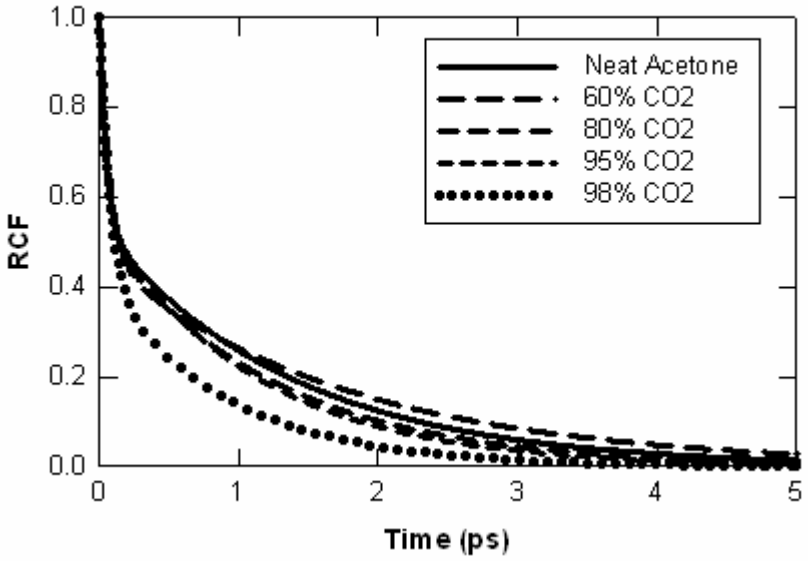

Figure B.3: First-order acetone RCFs along the C-Me bond vector in acetone GXLs (SRF case).

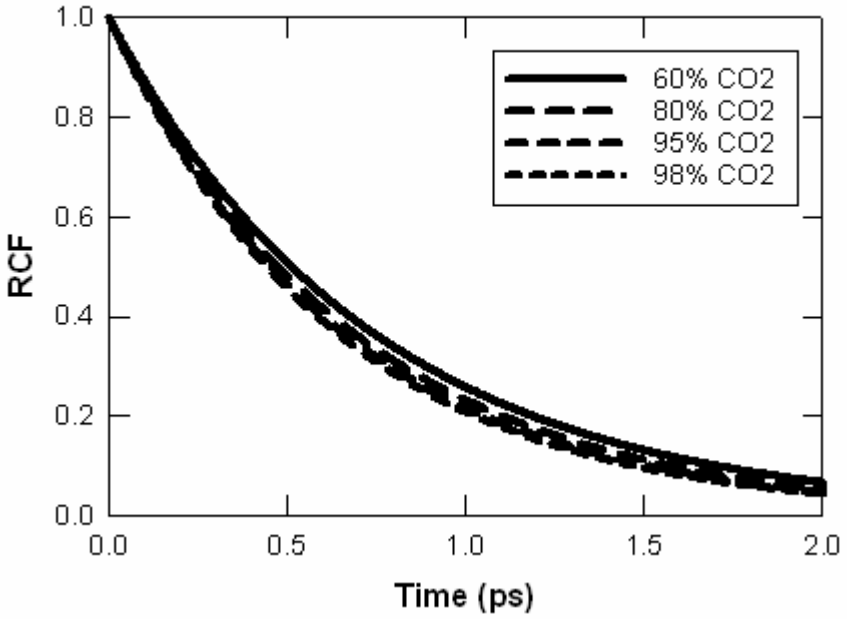

Figure B.4: First-order CO_2 RCFs in several MeOH GXLs (SRF case).

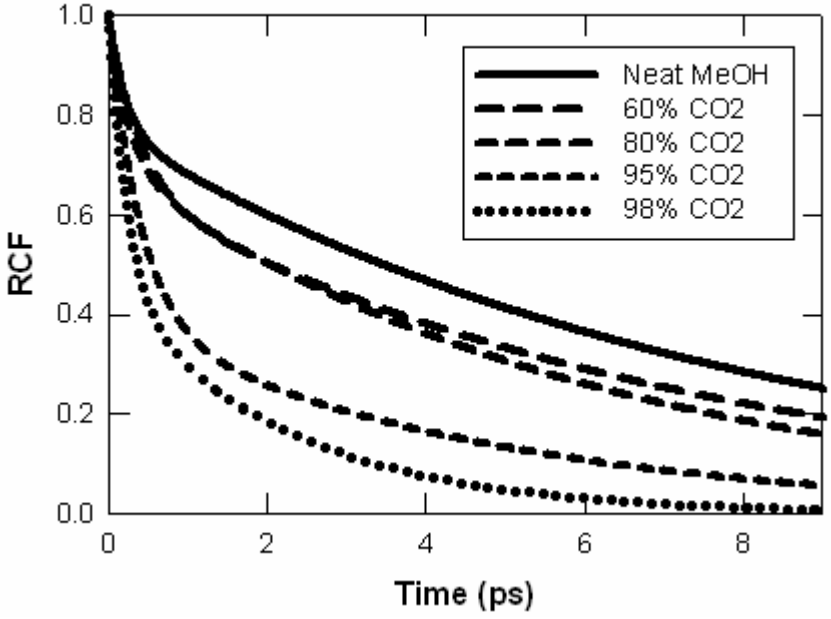

Figure B.5: First-order MeOH RCFs in MeOH GXLs (SRF case).

Table B.1: First-order CO_2 exponential decay fitting parameters in CO_2-expanded MeOH and Acetone. Pre-exponential parameters are unity.

τ_1 (ps) Acetone GXLs			
% CO_2	**Bulk**	**SRF**	**Cybo**
60%	0.942	0.914	1.139
80%	0.860	0.879	1.264
95%	0.704	0.732	0.904
98%	0.603	0.683	0.778
τ_1 (ps) MeOH GXLs			
60%	0.637	0.738	0.785
80%	0.629	0.683	0.971
95%	0.613	0.653	0.931
98%	0.614	0.637	0.629

Table B.2: Second-order CO_2 exponential decay parameters in CO_2-expanded MeOH and acetone. Pre-exponential parameters are unity.

τ_1 (ps) Acetone GXLs			
% CO_2	**Bulk**	**SRF**	**Cybo**
60%	0.300	0.307	0.340
80%	0.341	0.342	0.376
95%	0.366	0.356	0.429
98%	0.383	0.398	0.446
τ_1 (ps) MeOH GXLs			
60%	0.299	0.298	0.310
80%	0.277	0.289	0.378
95%	0.280	0.259	0.338
98%	0.261	0.258	0.280

Table B.3: First-order acetone RCF bi-exponential decay fitting parameters along both axes of rotation.

	a_1, C-O Rotational Axis			a_2, C-O Rotational Axis		
% CO_2	**Bulk**	**SRF**	**Cybo**	**Bulk**	**SRF**	**Cybo**
0%	0.288	0.331	0.274	0.712	0.669	0.726
60%	0.402	0.469	0.332	0.598	0.539	0.668
80%	0.504	0.406	0.477	0.496	0.594	0.523
95%	0.893	0.557	0.383	0.107	0.443	0.617
98%	0.875	0.646		0.125	0.354	
	τ_1 (ps), C-O Rotational Axis			**τ_2 (ps), C-O Rotational Axis**		
0%	0.231	0.258	0.188	1.430	1.548	1.915
60%	0.286	0.330	0.203	1.749	2.050	1.835
80%	0.357	0.273	0.364	2.211	1.540	2.366
95%	0.571	0.337	0.239	3.097	1.774	1.544
98%	0.453	0.331		4.606	1.185	
	a_1, C-Me Rotational Axis			**a_2, C-Me Rotational Axis**		
0%	0.461	0.462	0.471	0.539	0.538	0.529
60%	0.486	0.535	0.508	0.514	0.465	0.492
80%	0.522	0.475	0.615	0.478	0.525	0.385
95%	0.423	0.446	0.735	0.577	0.556	0.265
98%	0.607	0.579	0.579	0.393	0.421	0.421
	τ_1 (ps), C-Me Rotational Axis			**τ_2 (ps), C-Me Rotational Axis**		
0%	0.052	0.050	0.065	1.337	1.364	1.871
60%	0.057	0.074	0.057	1.475	1.763	1.962
80%	0.077	0.053	0.154	1.599	1.220	3.586
95%	0.035	0.045	0.320	0.895	1.093	2.927
98%	0.095	0.075	0.075	1.151	0.894	0.894

Table B.4: Second-order acetone RCF bi-exponential fitting parameters along both axes of rotation.

	a_1, C-O Rotational Axis			a_2, C-O Rotational Axis		
% CO_2	**Bulk**	**SRF**	**Cybo**	**Bulk**	**SRF**	**Cybo**
0%	0.642	0.620	0.597	0.358	0.380	0.403
60%	0.724	0.602	0.658	0.376	0.398	0.342
80%	0.644	0.787	0.913	0.356	0.213	0.087
95%	0.889	0.903	0.839	0.111	0.097	0.161
98%	0.976	0.950	0.749	0.024	0.050	0.251
	τ_1 (ps), C-O Rotational Axis			**τ_2 (ps), C-O Rotational Axis**		
0%	0.193	0.183	0.190	0.728	0.746	0.790
60%	0.198	0.175	0.156	0.931	0.713	0.895
80%	0.189	0.207	0.239	0.714	0.951	1.511
95%	0.221	0.217	0.204	1.259	1.394	0.701
98%	0.213	0.206	0.150	2.647	2.173	0.772
	a_1, C-Me Rotational Axis			**a_2, C-Me Rotational Axis**		
0%	0.748	0.798	0.682	0.252	0.202	0.318
60%	0.822	0.871	0.935	0.178	0.129	0.065
80%	0.783	0.798	0.756	0.217	0.211	0.244
95%	0.803	0.856	0.624	0.197	0.144	0.376
98%	0.758	0.560	-	0.242	0.440	EXP
	τ_1 (ps), C-Me Rotational Axis			**τ_2 (ps), C-Me Rotational Axis**		
0%	0.014	0.017	0.01	0.192	0.236	0.122
60%	0.019	0.022	0.028	0.302	0.535	2.442
80%	0.016	0.017	0.001	0.240	0.272	0.275
95%	0.017	0.022	0.002	0.222	0.282	0.348
98%	0.017	0.01	0.023	0.152	0.090	EXP

Table B.5: MeOH first-order RCF bi-exponential fitting parameters.

		a_1			a_2	
% CO_2	**Bulk**	**SRF**	**Cybo**	**Bulk**	**SRF**	**Cybo**
0%	0.232	0.232	0.195	0.768	0.768	0.805
60%	0.494	0.342	0.271	0.506	0.658	0.729
80%	0.323	0.303	0.269	0.677	0.697	0.731
95%	0.577	0.611	0.364	0.423	0.389	0.636
98%	0.565	0.553	0.898	0.435	0.447	0.102
		τ_1 (ps)			τ_2 (ps)	
0%	0.213	0.213	0.324	8.053	8.053	8.652
60%	0.490	0.386	0.244	6.317	7.333	10.195
80%	0.323	0.254	0.194	5.495	6.078	8.176
95%	0.294	0.397	0.236	3.403	4.659	4.032
98%	0.178	0.234	0.634	1.400	2.253	3.011

Table B.6: MeOH second-order RCF tri-exponential fitting parameters.

		a_1			τ_1 (ps)	
% CO_2	**Bulk**	**SRF**	**Cybo**	**Bulk**	**SRF**	**Cybo**
0%	0.169	0.211	0.185	0.212	0.049	0.036
60%	0.200	0.254	0.236	0.033	0.044	0.035
80%	0.296	0.352	0.268	0.048	0.065	0.044
95%	0.258	0.423	0.457	0.002	0.032	0.086
98%	0.351	0.331	0.267	0.001	0.001	0.001
		a_2			τ_2 (ps)	
0%	0.212	0.286	0.195	0.619	0.639	0.352
60%	0.253	0.383	0.239	0.332	0.819	0.422
80%	0.317	0.492	0.273	0.620	1.160	0.574
95%	0.434	0.387	0.038	0.282	0.410	13.750
98%	0.413	0.288	0.377	0.178	0.135	0.207
		a_3			τ_3 (ps)	
0%	0.619	0.503	0.620	3.457	3.885	3.895
60%	0.547	0.363	0.526	2.736	4.616	3.716
80%	0.387	0.155	0.459	3.271	9.074	3.633
95%	0.308	0.191	0.505	2.580	1.622	1.387
98%	0.236	0.381	0.356	0.805	0.764	2.425

APPENDIX C: DIFFUSION COEFFICIENTS OF HETEROCYCLIC SOLUTES IN CO_2-EXPANDED METHANOL

Introduction

Diffusion coefficients are important in the design and optimization of industrial-scale GXL processes. MD simulations are an alternative method for calculating diffusion coefficients and have previously been used to determine the binary diffusion coefficient of benzene in supercritical CO_2.[1] Likewise, simulated self-diffusion coefficients of MeOH in CO_2-expanded MeOH were determined by MD simulations and shown to increase with added CO_2 pressure.[2, 3] In this work, binary diffusion coefficients of the six heterocyclic compounds shown in Figure 5.1- benzene, pyridine, pyridazine, pyrimidine, and pyrazine- were determined in CO_2-expanded MeOH via MD simulations at 313 K and 150 bars.

This work was a follow-up to previous experimental work[4] performed by the Eckert-Liotta group where diffusion coefficients of these solutes were measured by Taylor-Aris (TA) dispersion techniques.[5-7] These solutes were chosen for their range of dipole moments and potential interactions with the solvent. The initial theory for this work was different effective solute sizes, consisting of the solute and first solvation shell, which would affect the diffusion. Diffusion coefficients from MD simulations agreed with the TA results in neat MeOH and reasonably well in neat sc-CO_2 but could not match the experiments under GXL conditions. Although the numbers did not match, MD simulations displayed faster diffusion with increased CO_2 that the experiments predicted. The effects of solute structure on diffusion were negligible in this study; however, it does

affect spectroscopy and the local solvent structure around the solute. This finding was the basis for the solvatochromic and solvent structure study presented in Chapter 5.

Computational Methods

Experimental Inputs for MD Simulations

In what follows, experimental conditions from the TA dispersion technique were used to conduct detailed and extensive MD simulations. It should be emphasized that this data describes the solvent component of a one-phase, high-pressure GXL. Consequently, we do not need to simulate the multi-phase equilibria as long as we only wish to address the microscopic properties of the solvent far away from the interface. Without the experiment, however, the multi-phase equilibrium simulation would be necessary in order to obtain the correct solvent density, for example. On the other hand, it is possible that the molecular model potentials contain errors that would lead to a partitioning in the multi-phase equilibria that differs from the experimental observations. The macroscopic properties of the metastable solvent phase in this model must therefore be validated as done below with respect to macroscopic variables such as diffusion coefficients.

Force Fields and Ensembles Used

Representative conditions from each of composition regime were selected from experiments and to conduct detailed and extensive MD simulations of the heterocyclic solutes in CO_2-expanded MeOH. The simulation system represents a single liquid phase with the compositions and pressure determined by these experiments and the density determined by the Patel-Teja equation of state.[8]

Carbon dioxide and MeOH were modeled as rigid collections of atomic sites with specified fixed charges interacting through pairwise-additive, site-site Lennard Jones and Coulomb forces. Equation C.1 presents the force field in the CO_2-MeOH systems.

$$u_{ij} = \sum_i \sum_{j>i} \left[4\varepsilon_{ij} \left\{ \left(\frac{\sigma_{ij}}{r_{ij}} \right)^{12} - \left(\frac{\sigma_{ij}}{r_{ij}} \right)^{6} \right\} + \frac{q_i q_j}{r_{ij}} \right] \qquad \text{Equation C.1}$$

Carbon dioxide pair interactions were modeled using the TrAPPE potential introduced in Chapters 3. The J2 potential (also used in Chapter 3 to 5) has been used for MeOH pair interactions. The potentials for pyridine, pyrimidine, pyridazine, pyrazine, and benzene are OPLS-derived.[9] 1,3,5-triazine was not used in the computational study because it lacked of a reliable force field. Each pairwise potential specifies a representation for the fixed point charges and these are assumed to remain fixed in the heterogeneous pairwise Coulomb interactions.

MD simulations were carried out using the DL_POLY Software package. Regardless of the relative composition, each simulated system box is populated by a total of 1001 molecules: one solute molecule and 1000 solvent/cosolvent molecules. Cubic PBCs were used throughout, but the length of the system box was scaled to preserve the specified density. Pair-wise terms in the potential were cut off at half the box length. Coulombic interactions were handled internally by DL_POLY with the Ewald summation method using the "automatic parameter optimization" option with a tolerance of 1E-5. The equations of motion were integrated using a time step of 2 fs with the Velocity verlet algorithm as implemented by DL_POLY. Initial configurations were generated by randomly distributing solvent molecules around a centralized solute and equilibrating using velocity rescaling for 200 ps in the canonical (NVT) ensemble. Temperature was

thermostated using a Nose-Hoover thermostat with 1ps relaxation time constant. Following equilibration, a long equilibrium simulation was run in the NVT ensemble. Trajectories were saved every 5ps and used as initial configurations for the transport and structural studies. Statistics of 100 trajectories were recorded over 500ps of MD simulation runs in the microcanonical (NVE) ensemble.

Results

Binary diffusion coefficients can be calculated from MD statistics using the Einstein relation:

$$D = \lim_{t\to\infty} \frac{1}{6t} \left\langle [\vec{r}(t) - \vec{r}(0)]^2 \right\rangle \qquad \text{Equation C.2}$$

Diffusion coefficients determined from MD simulation are presented in Figure C.1. The diffusivity of each solute increases as expected due to the nearly 75% decrease in viscosity between pure MeOH and 75mol% CO_2-expanded MeOH.[10] At first glance it appears that diffusion coefficients exhibit a slight structural dependency, particularly at 75% CO_2. Unfortunately there is substantial overlap of the error bars, which represent a 90% confidence interval for the data sets; and no statistical difference can be concluded from these data. Pyrazine diffusion at 25% CO_2 is slightly outside of the confidence intervals of the other solutes; however, the small margin of error introduces skepticism into a solid conclusion.

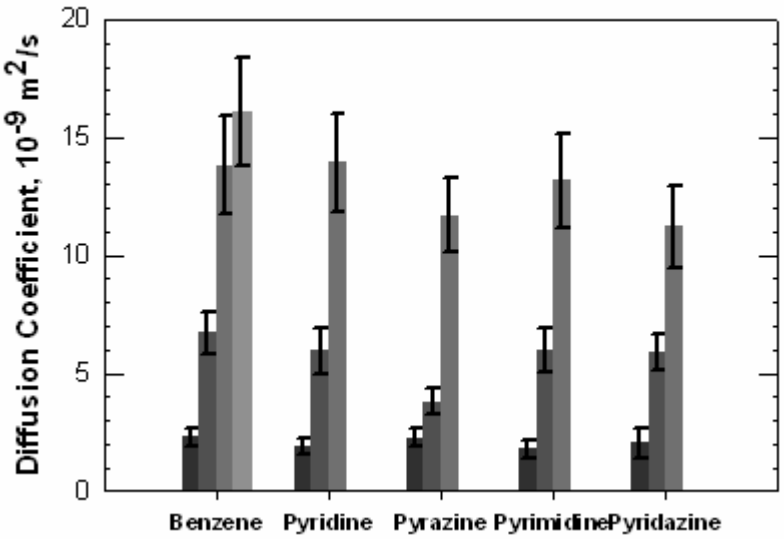

Figure C.1: Diffusion coefficients determined by MD simulation at 313K and 150 bars. Bars become progressively lighter with added CO_2 composition, starting in neat MeOH (darkest bars), 25% CO_2 75% CO_2, and pure CO_2 (lightest) for benzene only. Error bars represent a 90% confidence interval.

Comparison to Experiments

Experimental diffusion coefficients are presented in Figure C.2. The computational and experimental diffusion results agree in pure MeOH, but overestimate diffusion coefficients in GXLs. Benzene diffusion in pure CO_2 is slightly faster than the experimental prediction. Experimental diffusion coefficients in 25% CO_2 resemble diffusion in pure MeOH while the computational counterparts are intermediate between pure MeOH and 75% CO_2. Computational diffusion coefficients in 75% CO_2 resemble the experimental data in pure supercritical CO_2. The clear disagreement between experimental and computational techniques in GXLs and scCO_2 suggest a shortcoming in the CO_2 force field. This could be due to specific solvent-solute interactions like alkylcarbonic acids. These acids are formed in catalytic amounts in CO_2/alcohol mixtures

and are not accounted for in the MD simulations. They could influence diffusion by increasing the effective size of the solute molecules via strong interactions with nitrogen. This would explain the disparity seen in the GXLs, but not $scCO_2$ because benzene is incapable of forming these complexes. Most likely an assumption such as non-polarizable force fields or rigid CO_2 molecules caused the inaccurate diffusion coefficients. While the TA and MD simulation results do not agree, they indicate direction of changes, suggesting important molecular-scale phenomena exist and are concentration-dependent and influence diffusion.

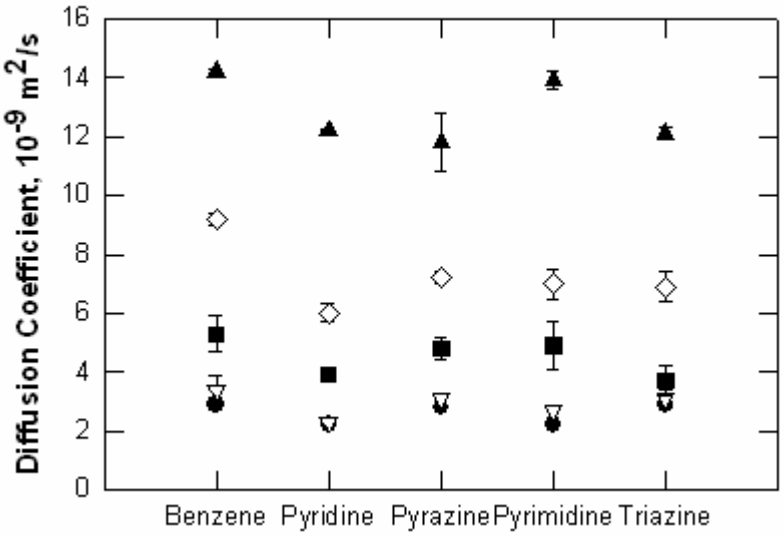

Figure C.2: Experimental diffusion coefficients measured by Taylor-Aris techniques at 313K and P=150bar. Neat MeOH (circles), 25% CO_2 (inverted triangles), 50% CO_2 (squares), 75% CO_2 (diamonds), 100% CO_2 (triangles).

Conclusions

Diffusion coefficients of heterocyclic compounds were determined in CO_2-expanded MeOH using TA dispersion techniques and MD simulations at 313 K and 150

bars. Binary diffusion coefficients of the solutes from both experiments and simulations increase with added CO_2, but are insensitive to solute polarity and structure. In other words, any local structure in the cybotactic region of the solute molecules (from different solute structure) does not significantly impact its diffusion. The simulated diffusion coefficients overpredict the experimental values in most cases except neat MeOH; however, simulations show the general trend of faster diffusion with CO_2 addition. It appears that while MeOH force field is well suited for transport studies, the CO_2 model exhibits faster diffusion than this work and literature sources predict. Although a discrepancy exists between computation and experiment, MD simulations predict the general trend of diffusion with bulk viscosity and could be improved with more appropriate CO_2 models to better describe transport phenomena.

References

1. Zhou, J.; Lu, X. H.; Wang, Y. R.; Shi, J., Molecular dynamics investigation on the infinite dilute diffusion coefficients of organic compounds in supercritical carbon dioxide. *Fluid Phase Equilib.* **2000,** 172, (2), 279-291.

2. Aida, T.; Inomata, H., MD simulation of the self-diffusion coefficient and dielectric properties of expanded liquids - I. Methanol and carbon dioxide mixtures. *Molecular Sim.* **2004,** 30, (6), 407-412.

3. Shukla, C. L.; Hallett, J. P.; Popov, A. V.; Hernandez, R.; Liotta, C. L.; Eckert, C. A., Molecular dynamics simulation of the cybotactic region in gas-expanded methanol- carbon dioxide and acetone-carbon dioxide mixtures. *J. Phys. Chem. B* **2006,** 110, (47), 24101-24111.

4. Maxey, N. B. Transport and Phase-Transfer Catalysis in Gas-Expanded Liquids. Georgia Institute of Technology, Atlanta, 2006.

5. Taylor, G., The dispersion of matter in turbulent flow through a pipe. *Proc. Roy. Soc. (London)* **1954,** A223, 446-468.

6. Aris, R., On the dispersion of a solute in a fluid flowing through a tube. *Proceedings of the Royal Society of London Series A-Mathematical and Physical Sciences* **1956,** 235, (1200), 67-77.

7. Aris, R., Dispersion of a solute by diffusion, convestion, and exchange between phases. *Proc. Roy. Soc. (London)* **1959,** A252, 538-550.

8. Patel, N. C.; Teja, A. S., A new cubic equation of state for fluids and fluid mixtures. *Chem. Eng. Sci.* **1982,** 37, (3), 463-473.

9. Jorgensen, W. L.; McDonald, N. A., Development of an all-atom force field for heterocycles. Properties of liquid pyridine and diazenes. *Theochem-J. Molec. Structure* **1998,** 424, (1-2), 145-155.

10. Sih, R.; Dehghani, F.; Foster, N. R., Viscosity measurements on gas expanded liquid systems - Methanol and carbon dioxide. *J. Supercrit. Fluids* **2007,** 41, (1), 148-157.

APPENDIX D: SOLVENT EFFECTS ON TAUTOMERIC EQUILIBRIUM IN GAS-EXPANDED LIQUIDS

The keto/enol tautomeric equilibrium of diketones is a solvent-dependent phenomenon. Benzoylacetone (BZA) was chosen as the diketone for this study because its tautomeric equilibrium constant is sensitive to local solvent polarity and gives a good distribution of both enol and diketone forms. The tautomeric equilibrium reaction for BZA is shown in Figure D.1.

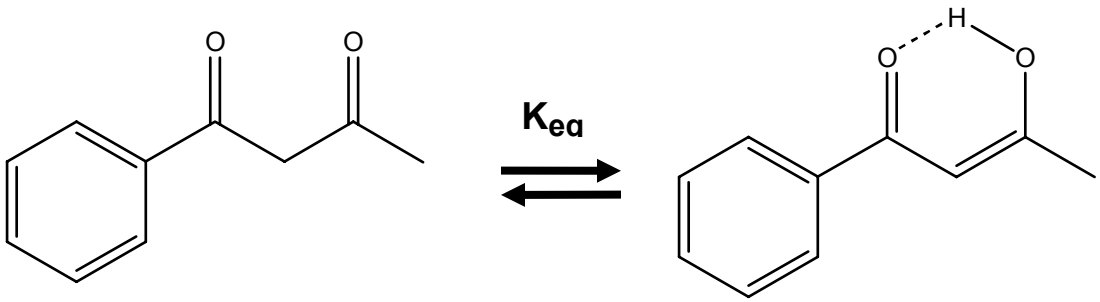

Figure D.1: Tautomeric equilibrium reaction of benzoylacetone.

Local solvent interactions have a profound effect on the equilibrium constant,[1-3] so the objective of this work was to use MD simulations to explore local solvent structure and use IR spectroscopy to measure the equilibrium constants in various GXLs. This would demonstrate the effects of the local composition on chemical equilibrium. Because the equilibrium is solvent dependent, the reaction coordinate was described by the total interaction energy of the solvent with BZA. The total interaction energy is the sum of electrostatic and dipolar or Lennard-Jones interactions.

Initial MD simulations showed that BZA was preferentially solvated by the organic component of the GXL. Thus very high CO_2 compositions were required to change the tautomeric equilibrium. The pressures needed to obtain such compositions at 25°C exceded the pressure rating of the attenuated total reflectance (ATR)-IR cell. Further attempts with a high-pressure UV/vis cell fitted with ZnSe windows (transparent to IR light) had a large path length that absorbed the entire incident IR beam. Consequently, experiments were halted, but we attempted to obtain thermodynamic data from reaction coordinate data. A similar study was done by Arroyo et al to obtain free energies of reaction in water/formaldehyde mixtures.[4] Free energy can be calculated from reaction coordinate statistics from Equation D.1:

$$\Delta G_s(\Delta E) = -k_b T \cdot \ln P_s(\Delta E) \qquad \text{Equation D.1}$$

where ΔG_s is the free energy of the solute, ΔE is the reactant coordinate or total solvent-solute interaction energy, k_b is Boltzmann's constant, T is temperature, and P_s is the probability of finding a solvent configuration with interaction energy ΔE. Probabilities were found by periodically sampling trajectories and calculating the Coulombic and Lennard-Jones potential (Equation 3.6) between every solvent and BZA atom. Frequencies were tabulated as integers in a histogram. Simulations of the enol and diketone forms were run to construct free energy diagrams of each form. An example of free energy curves and the relevant thermodynamic values are shown in Figure D.2:

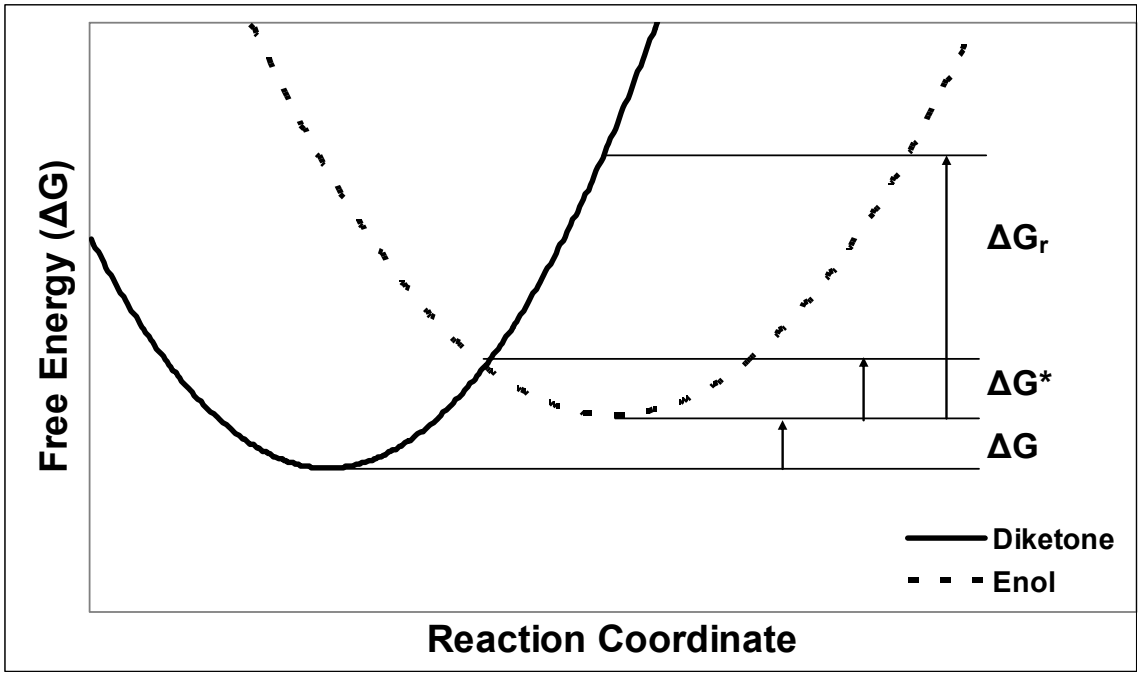

Figure D.2: Sample free energy curves of a keto/enol tautomerization reaction.

Several thermodynamic quantities can be estimated from Figure D.2: the tautomeric free energy (ΔG), free energy of activation (ΔG*), and the free energy of reorganization (ΔG_r) which is the energy required to rearrange the solvent and enable tautomerization. Simulations of a single BZA molecule in both the enol and diketone forms were run in CO_2-expanded MeOH, acetonitrile (ACN), and cyclohexane at three different organic compositions: 40%, 15%, and 5%.

Figure D.3 to Figure D.5 depict the free energy curves in three MeOH GXLs. In each case the diketone form is shown to be more thermodynamically stable which would be expected because MeOH is polar and can better stabilize the carbonyl groups with hydrogen bonds. The tautomeric free energies of each form are quite similar in all three GXLs, which indicates an equilibrium of nearly unity with minimal solvent reorganization requirements to revert back to the enol form.

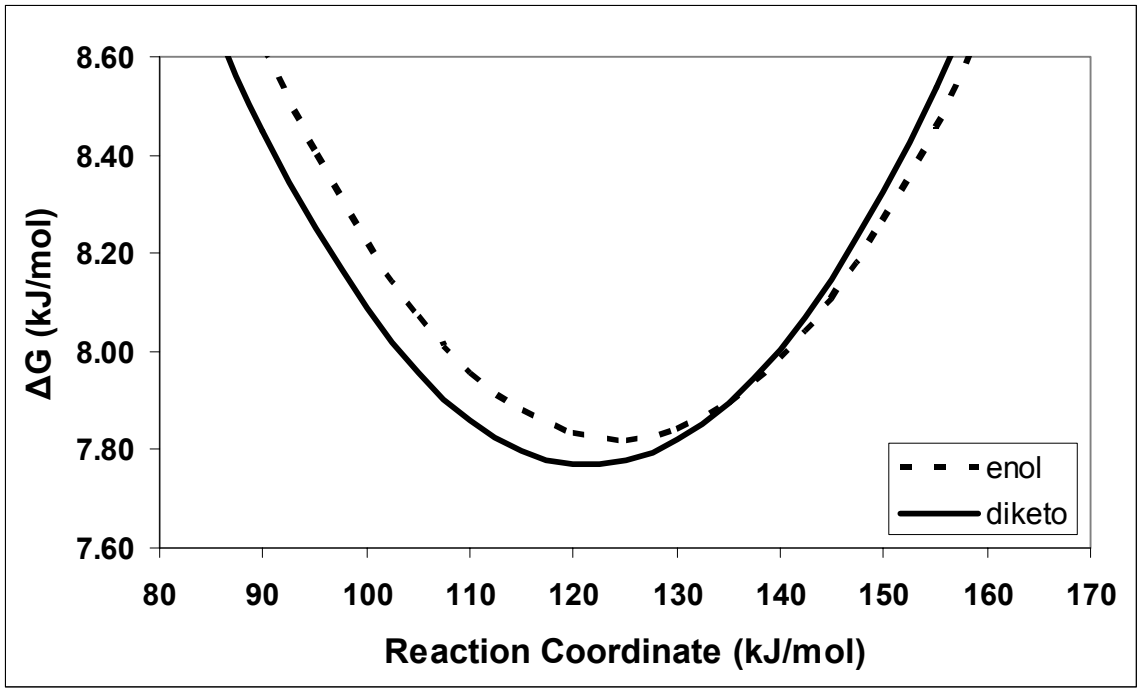

Figure D.3: Free energy curves of BZA in a 5% MeOH GXL.

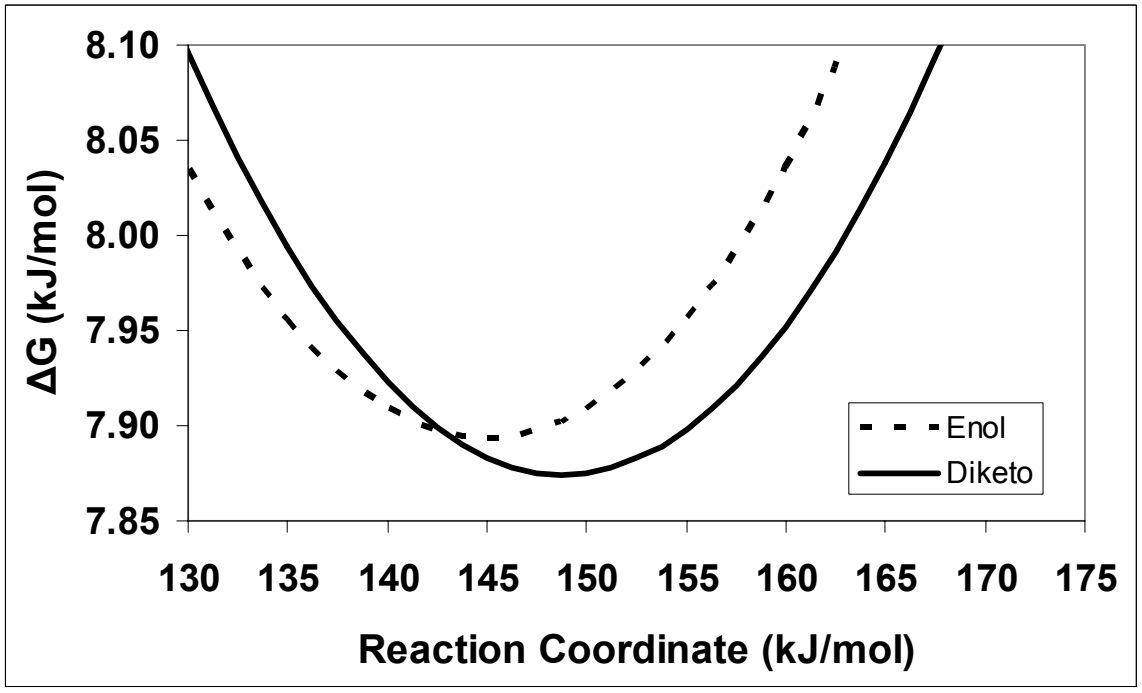

Figure D.4: Free energy curves of BZA in a 15% MeOH GXL.

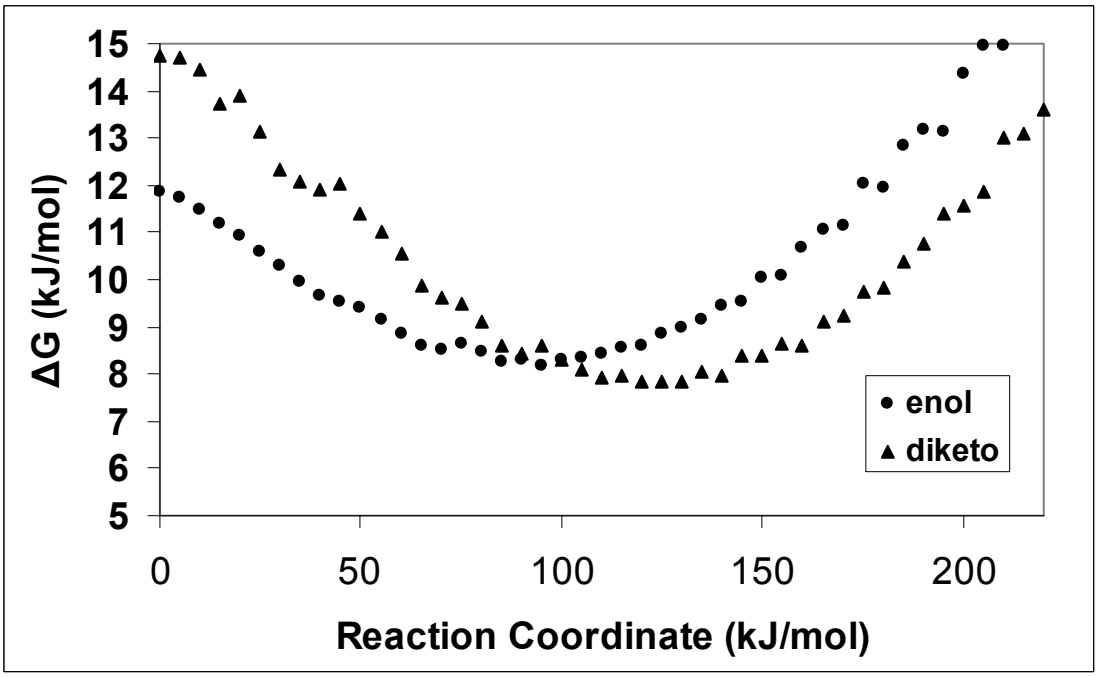

Figure D.5: Free energy curves of BZA in a 40% MeOH GXL.

Figure D.6 to Figure D.8 show that the enol form is most stable in all three ACN GXLs. ACN is a more polar than MeOH, but is aprotic. This result suggests that hydrogen bonding is an important factor in stabilizing the diketone form. Another important difference is the large free energy differences between the enol and diketone forms which seem to be equal in each solvent. This behavior is consistent with a similar solvation pattern in all three GXLs. ACN likely preferentially solvates BZA and therefore the reorganization free energy is similar in each case.

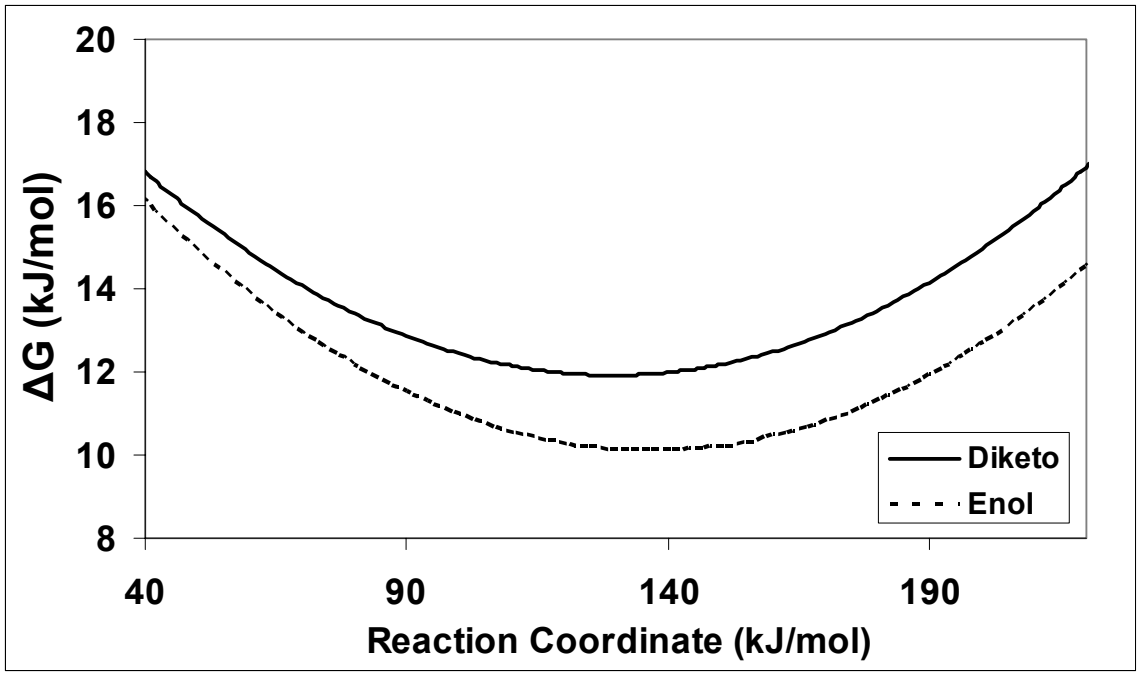

Figure D.6: Free energy curves of BZA in a 5% ACN GXL.

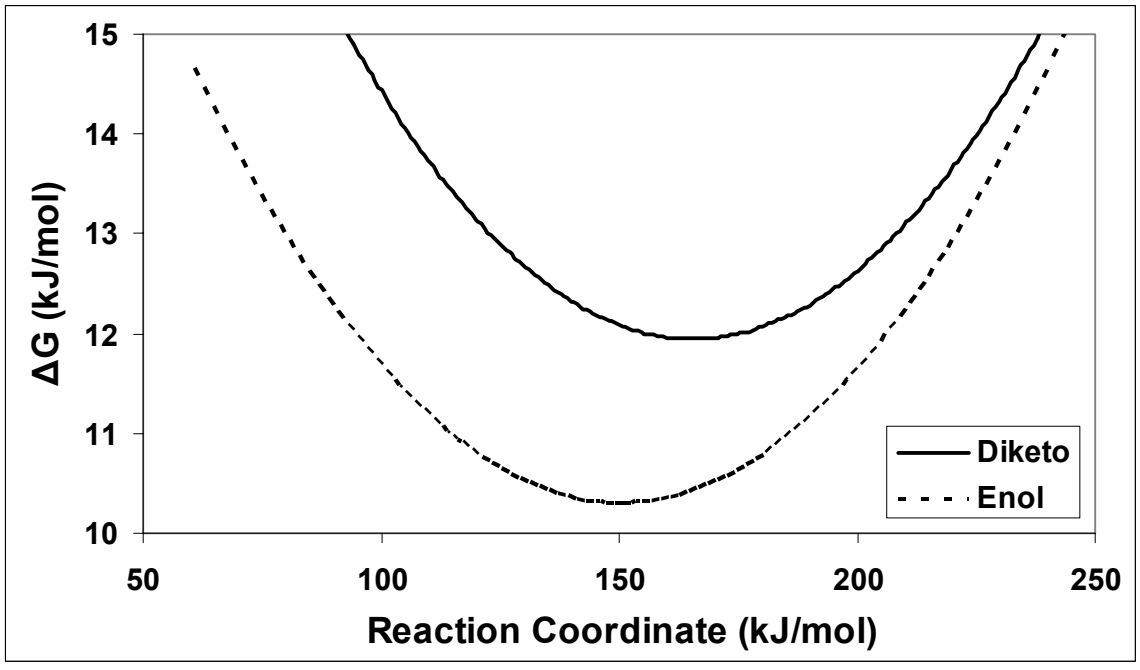

Figure D.7: Free energy curves of BZA in a 15% ACN GXL.

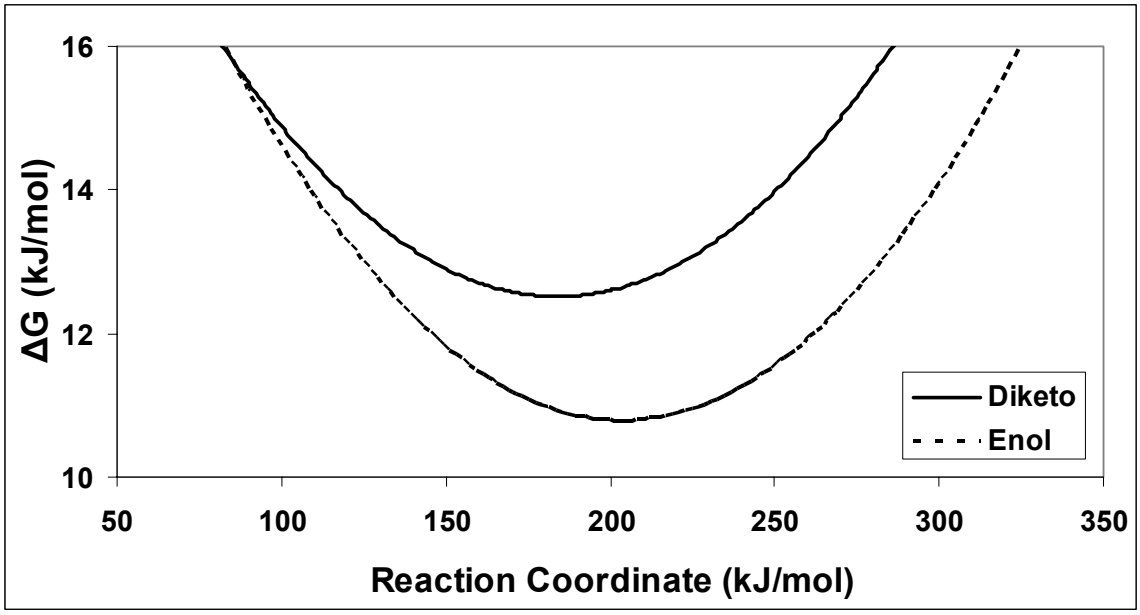

Figure D.8: Free energy curves of BZA in a 40% ACN GXL.

Free energy curves in cyclohexane GXLs are shown in Figure D.9 to Figure D.11. The free energy curves have strange behavior where the tautomeric free energy is nearly zero in all three GXLs although the enol form is more stable. Consequently reorganization free energies are very large. Both CO_2 and cyclohexane are non-polar and have much solvation patterns than the other two types of GXLs. The enol from would likely be the more dominant form since the diketone is only stable in polar environments.

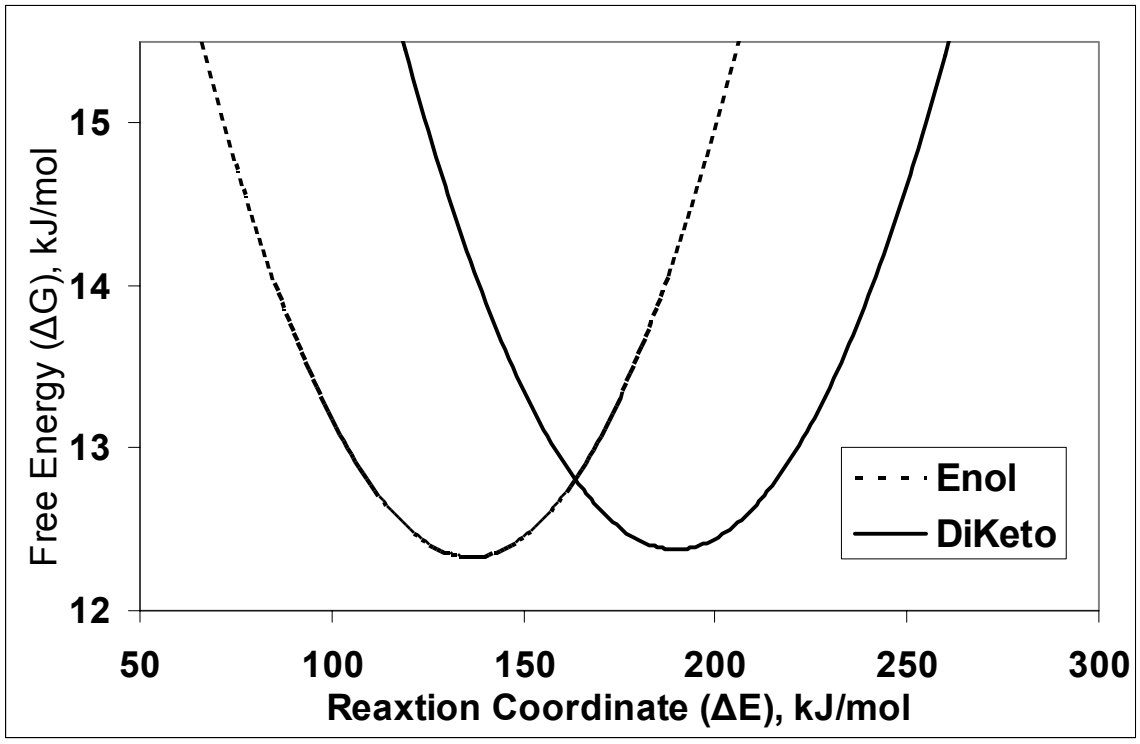

Figure D.9: Free energy curves of BZA in a 5% cyclohexane GXL.

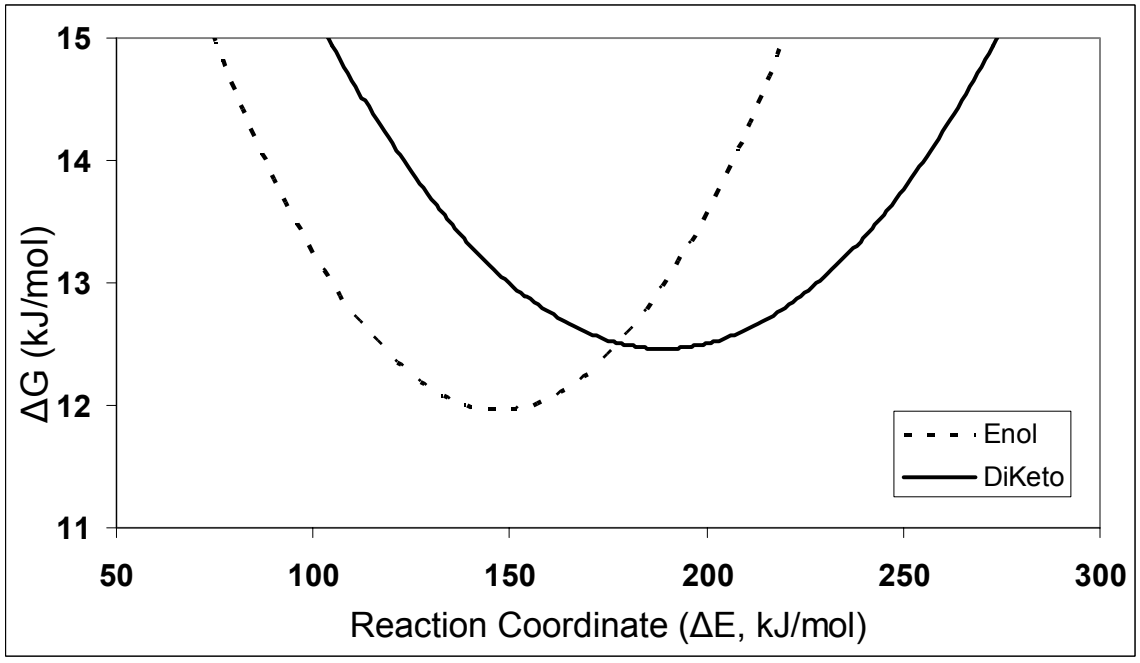

Figure D.10: Free energy curves of BZA in a 15% cyclohexane GXL.

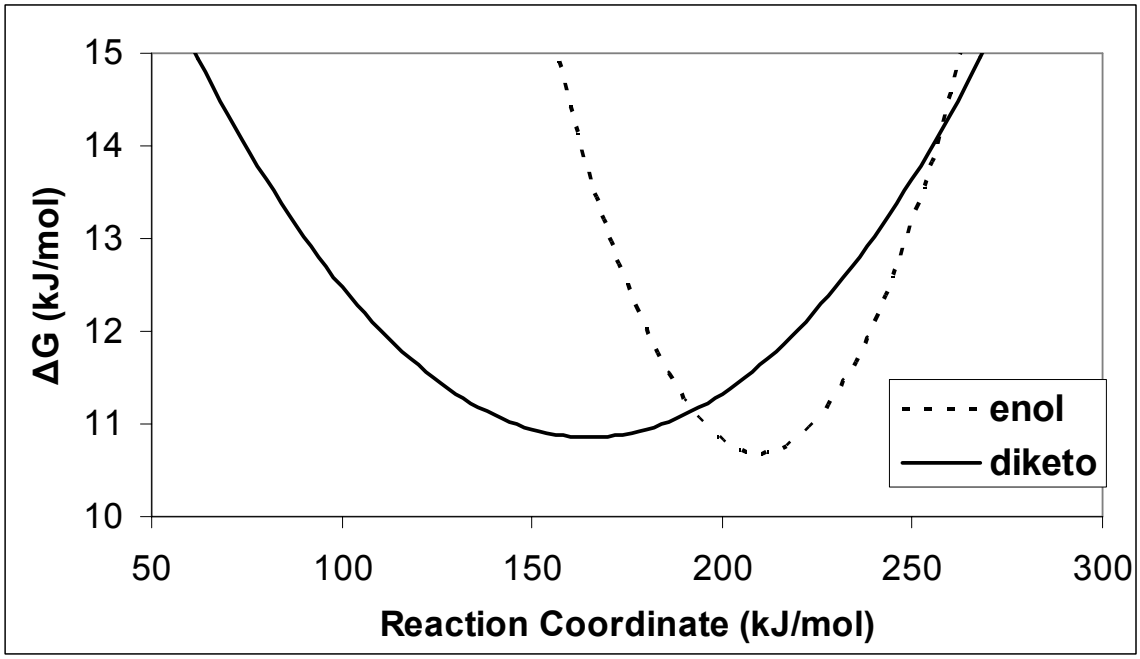

Figure D.11: Free energy curves of BZA in a 40% cyclohexane GXL.

These results demonstrate the ability of MD simulations to study equilibrium reactions and could be used to study solvolysis or other reactions with a reaction coordinate related to the solvent. The force fields and models used in this study were too simplistic to obtain accurate thermodynamic information. More complex models for BZA such as polarizable force fields and non-rigid bodies could better model solvation. The real system involves electron withdrawal and rotation around bonds, and hydrogen bond formation that are not accounted for at this time. This would impact the solvation shell and thus the tautomeric equilibrium and its related free energies. While the information presented in this project is simple, it is a starting place for future studies in GXLs and other novel solvents.

References

1. Abood, N. A.; Ajam, A. F., Infrared study of keto-enol equilibrium of acetylacetone, benzoylacetone and dibenzoylmethane in various organic solvents. *J. Chem. Soc. Pak.* **1985,** 7, (1), 1-6.

2. Sloop, J. C.; Bumgardner, C. L.; Washington, G.; Loehle, W. D.; Sankar, S. S.; Lewis, A. B., Keto-enol and enol-enol tautomerism in trifluoromethyl-beta-diketones. *J. Fluor. Chem.* **2006,** 127, (6), 780-786.

3. Henry, M. C.; Yonker, C. R., FT-IR studies of acetylacetonates in supercritical CO2 using a capillary cell at pressures up to 3.1 kbar. *Anal. Chem.* **2004,** 76, (16), 4684-4689.

4. Arroyo, S. T.; Martin, J. A. S.; Garcia, A. H., Molecular dynamics simulation of the reaction of hydration of formaldehyde using a potential based on solute-solvent interaction energy components. *J. Phys. Chem. A* **2007,** 111, (2), 339-344.

APPENDIX E: CIS/TRANS ISOMERIZATION REACTION KINETICS IN GAS-EXPANDED LIQUIDS

Introduction

4-(diethylamino)-4'-nitroazobenzene (DENAB), shown in Figure E.1, is stable in the *trans* form at ground-state conditions. Upon excitation, the molecule undergoes rapid isomerization the *cis* form. The *cis* isomer is less stable than the *trans* isomer and undergoes a reverse isomerization once the excitation beam is removed. The cis/trans isomerization has two mechanisms[1]: fast rotation of a charge-separated intermediate and slow inversion about the azo bond. The mechanism is influenced by the solvent and the reaction rate is highly coupled to the solvent environment. Polar solvents stabilize the charge-separated transition state which increases the isomerization rate. The rate in non-polar solvents is orders-of-magnitude slower because the transition state is short-lived and the inversion process is slower. Consequently the DENAB isomerization reaction probes local solvent polarity and has been used to probe a variety of media, including SCFs[2, 3] and organic solvents of varying polarity.[1, 4-6] DENAB has been incorporated into polymers and surfaces to add photo-responsive properties for optics applications photo-responsive polymers.[7, 8]

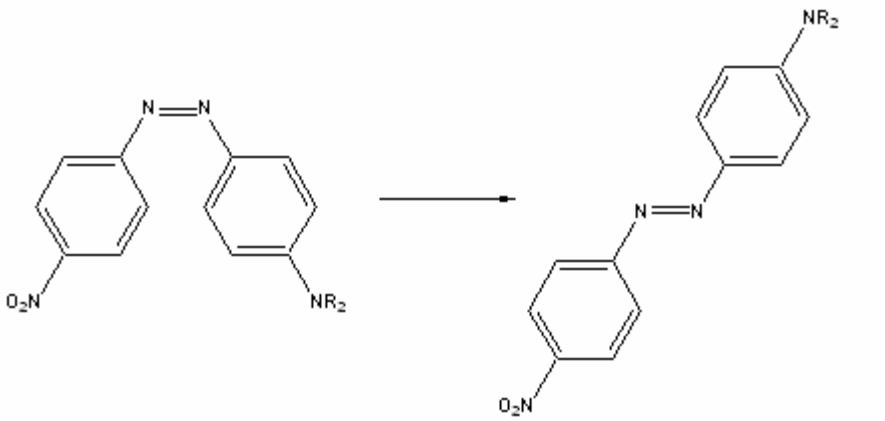

Figure E.1: *cis*/*trans* isomerization reaction of DENAB.

Experimental Methods

DENAB (>99% pure) was purchased from Aldrich and used as is. Anhydrous solvents were added to an evacuated pressure cell with a gas-tight syringe to avoid water contamination. The pressure cell was equipped with three sapphire windows positioned on three sides of the cell and a cooling jacket connected to an external ethylene glycol chiller. CO_2 was dried over molecular sieves prior to use and metered into the cell with an Isco syringe pump. Temperature was monitored with an Omega J-type thermocouple in contact with the liquid phase and pressure was monitored with a Druck pressure transducer.

The incident light was a Kratos LH151 N/2 short arc lamp with 1000-W power. The lamp was equipped with a monochrometer which was removed to provide more intensity. The DENAB isomerization reaction was probed by monitoring the reappearance of the *trans* isomer at ~450nm using a DH-2000-BAL UV/visible/near infrared light source from from Mikropack and HR4000 fiber optic detection system from Ocean Optics. The reaction followed first order kinetics.

Results

Several CO_2-expanded solvents were studied: 1,4 dioxane, cyclohexane, hexane, and acetone. The solvents were chosen to give a wide range of polarity that would have different sensitivity to CO_2 addition. First order rate constants are shown versus CO_2 mole fraction in Figure E.2. The rate in pure 1,4 dioxane agreed reasonable well with the literature value[6] (0.037 s^{-1}) and followed the appropriate trend, decreasing rate with added CO_2. The rate in cyclohexane and hexane was an order of magnitude faster than the literature values.[6] Hexane was unaffected by CO_2 addition while the rate in cyclohexane increased with added CO_2. These results were puzzling and were never reproducible within reasonable error. The reaction in neat acetone was too fast to measure with our equipment and would require a detection system with fs resolution to monitor the reaction progress. CO_2 did not slow down the reaction, even at 90% CO_2. This implies that DENAB is preferentially solvated by acetone which could stabilize the charge-separated transition state. Another explanation is CO_2 interaction with the amine group to further stabilize the transition state. The acetone results showed promise and could be a probe of local polarity and preferential solvation if the appropriate equipment became available. The project was halted because the non-polar solvent data was questionable and unavailability of equipment for polar solvents.

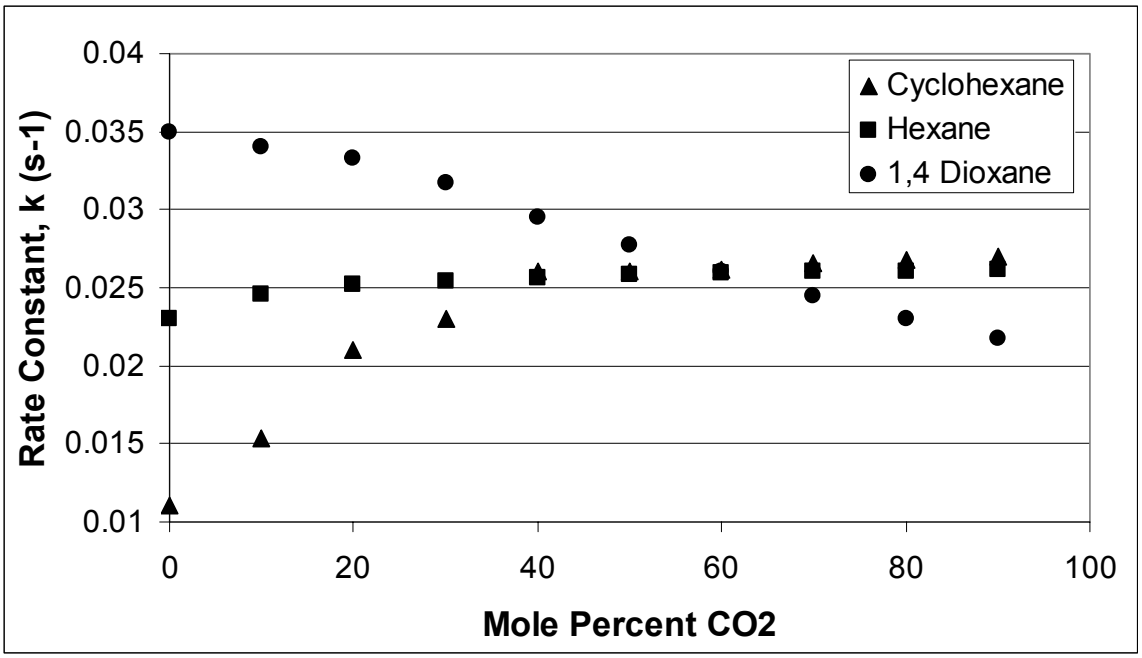

Figure E.2: First order rate constants in CO_2-expanded cyclohexane, hexane, and 1,4 dioxane.

References

1. Asano, T.; Okada, T., Further kinetic evidence for the competitive rotational and inversional z-e isomerization of substituted azobenzenes. *J. Org. Chem.* **1986,** 51, (23), 4454-4458.

2. Dillow, A. K.; Brown, J. S.; Liotta, C. L.; Eckert, C. A., Supercritical fluid tuning of reactions rates: The cis-trans isomerization of 4-4 '-disubstituted azobenzenes. *J. Phys. Chem. A* **1998,** 102, (39), 7609-7617.

3. Sigman, M. E.; Leffler, J. E., Supercritical carbon-dioxide - the cis to trans relaxation and π-π* transition of 4-(diethylamino)-4'-nitroazobenzene. *J. Org. Chem.* **1987,** 52, (14), 3123-3126.

4. Wildes, P. D.; Pacifici, J. G.; Irick, G.; Whitten, D. G., Solvent and substituent effects on thermal isomerization of substituted azobenzenes - flash spectroscopic study. *J. Am. Chem. Soc.* **1971,** 93, (8), 2004-&.

5. Schanze, K. S.; Mattox, T. F.; Whitten, D. G., Correlation of the rate of thermal cis-trans isomerization of para-nitro-para'-dialkylaminoazobenzenes with solvent-z value applied to study polarity in aqueous surfactant solutions. *J. Am. Chem. Soc.* **1982,** 104, (6), 1733-1735.

6. Schanze, K. S.; Mattox, T. F.; Whitten, D. G., Solvent effects upon the thermal cis-trans isomerization and charge-transfer absorption of "4-(diethylamino)-4'-nitroazobenzene. *J. Org. Chem.* **1983,** 48, (17), 2808-2813.

7. Brown, D.; Natansohn, A.; Rochon, P., Azo polymers for reversible optical storage .5. orientation and dipolar interactions of azobenzene side-groups in copolymers and blends containing methyl-methacrylate structural units. *Macromolecules* **1995,** 28, (18), 6116-6123.

8. Natansohn, A.; Rochon, P.; Barrett, C.; Hay, A., Stability of photoinduced orientation of an azo compound into a high-Tg polymer. *Chem. Mater.* **1995,** 7, (9), 1612-1615.

APPENDIX F: SOLVATOCHROMIC BEHAVIOR OF ELLIPTICINE IN GAS-EXPANDED LIQUIDS

Introduction

Ellipticine (Figure F.1) is an anti-caner drug, but is be used in UV/vis and fluorescence spectroscopy as a chromophore. Recent studies explored the solvatochromic behavior of ellipticine in various organic solvents. This would allow *in vivo* spectroscopic monitoring of ellipticine uptake into target cancer cell by linking solvatochromic behavior to different environments.[1, 2] Interesting dual fluorescence behavior was observed in protic solvents that could potentially be used to assay the acidity or proton concentration of the medium.

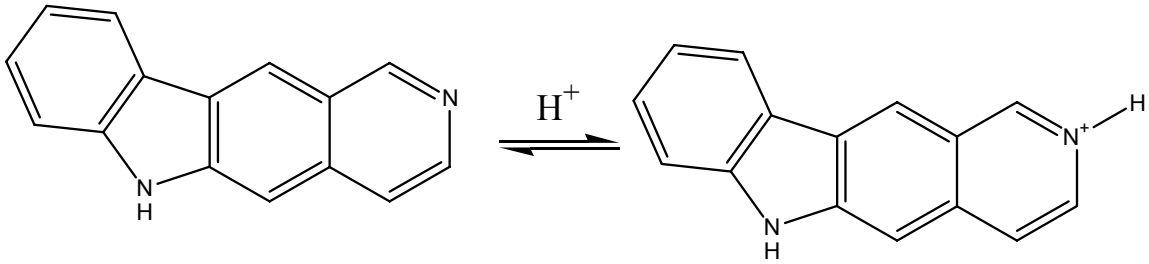

Figure F.1: Structure of ellipticine and the protonated form.

Results

Fluorescence spectra in several CO_2-MeOH mixtures are shown in Figure F.2. As expected dual fluorescence is seen in the neat solvent because MeOH is protic. As CO_2 is added the intensity of the un-protonated peak (450nm) decreases while the protonated peak (530nm) increases. This behavior is consistent with ACA formation and dissociation, but a concern is the inferred high pK_a of ellipticine. Very little CO_2 is

needed to instill a large change in the fluorescence spectra. There is a large response by adding just 0.4% CO_2 as the un-protonated peak nearly disappears. There is little change between this composition and 3.7% CO_2 indicating that most ellipticine has been protonated. Ellipticine is very basic and this result is not surprising, but suggests that ellipticine fluorescence is not a valid technique for MCA. Carbonic acid formation from water contamination is a concern and increases the amount of preparation to dry samples. Ellipticine fluorescence is a potential analysis technique for weaker ACAs like BCA, which is several orders of magnitude weaker than MCA and ECA.

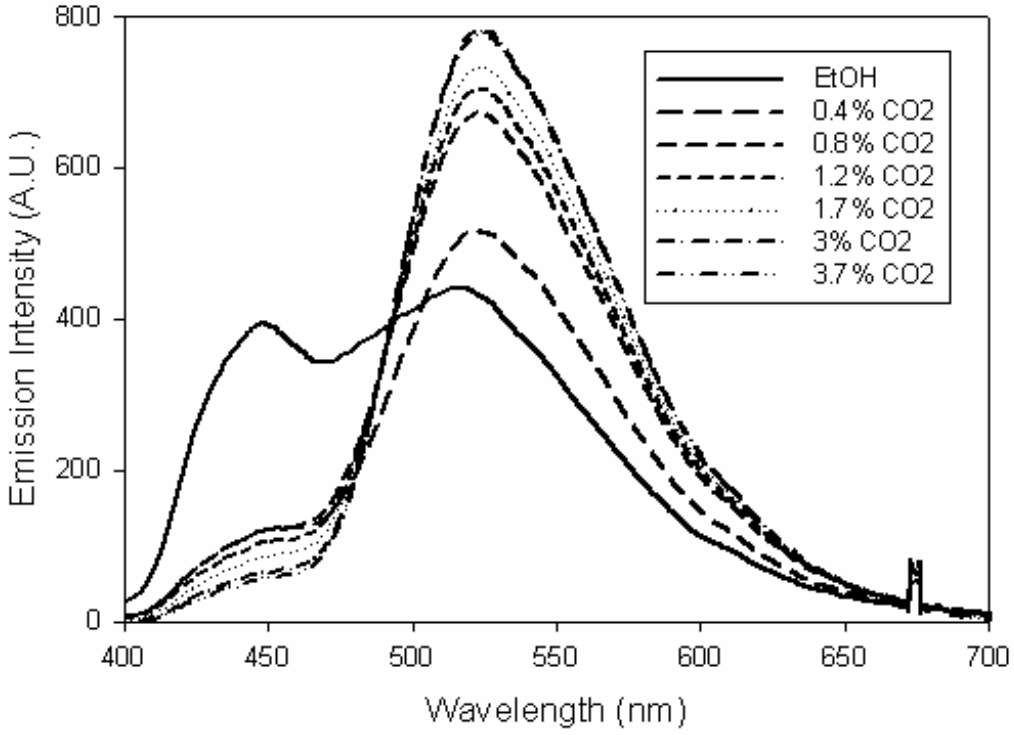

Figure F.2: Ellipticine emission spectra in CO_2-expanded MeOH.

Absorption spectra in CO_2-expanded MeOH and EtOH have an additional peak at ~310nm that is not present in the neat alcohols. Consequently the absorption spectra were

taken to check the sensitivity of this peak to CO_2 composition as an alternative to fluorescence spectroscopy. The absorption spectra in CO_2-expanded MeOH and EtOH are shown in

Figure F.3 and Figure F.4 respectively. Absorption in neat MeOH shows a single peak at ~315nm that splits into two peaks at 310nm and 330nm. This could be due to ACA protonation, but is insensitive to CO_2 composition after the initial split. There are some dilution effects from solvent expansion. Neat EtOH absorption does not have a peak at 310nm, but CO_2 addition causes the appearance of a peak at this wavelength. This magnitude decreases as more CO_2 is added due to dilution effects indicating that all ellipticine molecules are protonated. This behavior is consistent with the fluorescence results and consequently ellipticine was replaced by 2,6 dinitrophenol, which has a lower pK_a and thus greater sensitivity to ACAs.

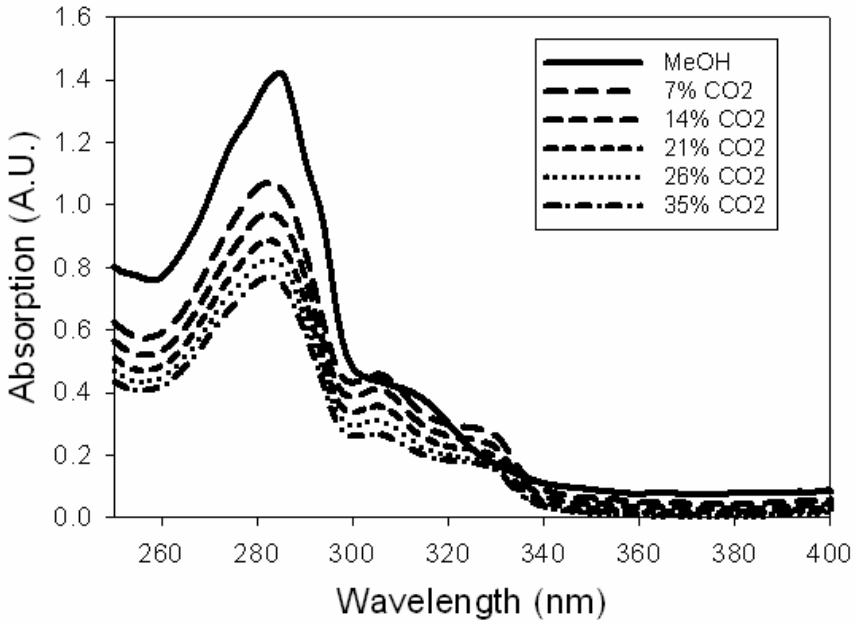

Figure F.3: Ellipticine absorption spectra in CO_2-expanded MeOH.

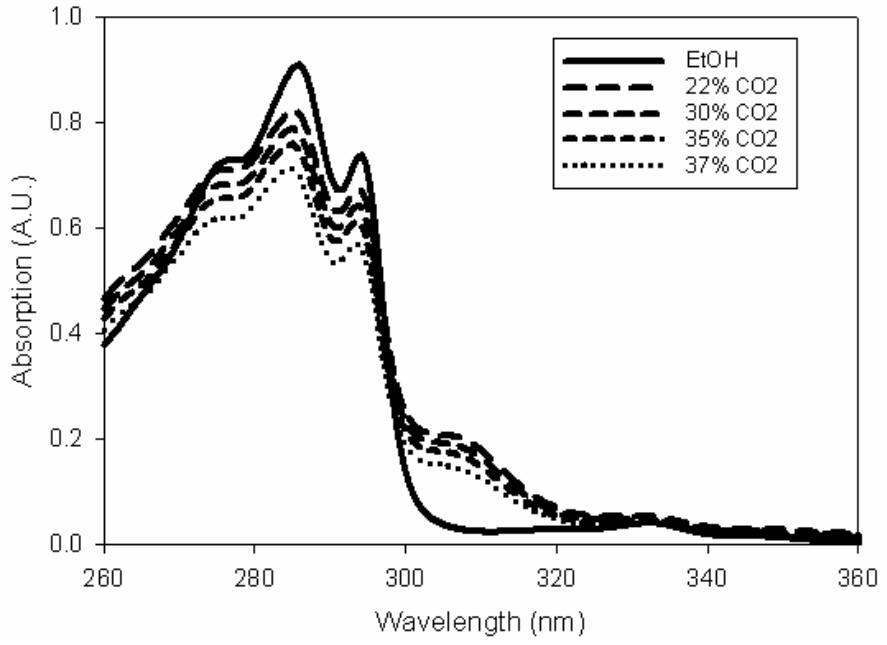

Figure F.4: Ellipticine absorption spectra in CO_2-expanded EeOH.

References

1. Fung, S. Y.; Duhamel, J.; Chen, P., Solvent effect on the photophysical properties of the anticancer agent ellipticine. *J. Phys. Chem. A* **2006,** 110, (40), 11446-11454.

2. Miskolczy, Z.; Biczok, L.; Jablonkai, I., Effect of hydroxylic compounds on the photophysical properties of ellipticine and its 6-methyl derivative: The origin of dual fluorescence. *Chem. Phys. Lett.* **2006,** 427, (1-3), 76-81.

APPENDIX G: NEUTRON DIFFRATION EXPERIMENTS IN CO_2-EXPANDED METHANOL AND CO_2-EXPANDED ACETONE

Our group was awarded neutron beam time at Los Alamos and Argonne National Laboratories in the fall semester of 2005. The objective was to experimentally determine radial distribution functions (RDFs), g(r), in CO_2-expanded MeOH and acetone. This would serve as a direct comparison to RDFs determined computationally by former group member and Ph. D. student, Charu Shukla.[1] This work could be used to tune force field parameters used in MD simulations to demonstrate the how a synergistic combination of simulation and experiments leads to more information similar to the work of Cipriani and co-workers.[2] Neutron diffraction studies have been performed in $scCO_2$[3] and scMeOH.[4]

Neutron diffraction experiments at the Los Alamos Neutron Science Center (LANSCE) were performed on the High-Intensity Pulsed Preferred Orientation (HIPPO) Diffractometer under the supervision of instrument scientist Sven Vogel. Due to limited beam time only CO_2-expanded MeOH was used. The MeOH was either fully deuterated (CD_3OD) or partially deuterated (CD_3OH) because neutrons scatter from nuclear interactions and the different isotopes scatter neutrons differently.[5] This technique enables the differentiation between the protic and methyl hydrogen atoms on the MeOH molecule; each type of hydrogen gives a different RDF. We considered three different compositions: 31%, 77%, and 90% CO_2 and two temperatures: 25°C and 40°C, or twelve separate runs considering the two MeOH species. Typical neutron cells are Titanium Zirconium, TiZr based because this material is invisible to neutrons. Other materials can

be used if a collimated light is used, which eliminates Bragg scattering from the cell. The cell (provided by LANSCE) was aluminum and collimated light was not available, consequently the scatter pattern had large Bragg peaks from the aluminum cell. Attempts to calculate RDFs with the software package PDFgetN,[6] a free software package developed by LANSCE scientists, resulted in erroneous results that were of no value.

Neutron diffraction experiments at Argonne National Laboratories where done in collaboration with Chris Benmore and Joan Sweeney on the Gases, Liquids, and Amorphous Diffractometer (GLAD) at the Intense Pulsed Neutron Source (IPNS) facility. The MeOH/CO_2 experiments were again the focus since the LANSCE experiments yielded erroneous results. CO_2-expanded acetone would have been considered if time permitted. These experiments started off promising, but the TiZr pressure cell failed and the experiments were terminated.

References

1. Shukla, C. L. Computationally Probing the Cybotactic Region in Gas-Expanded Liquids. Georgia Institute of Technology, Atlanta, 2006.

2. Cipriani, P.; Nardone, M.; Ricci, F. P.; Ricci, M. A., Orientational correlations in liquid and supercritical CO2: neutron diffraction experiments and molecular dynamics simulations. *Mol. Phys.* **2001,** 99, (4), 301-308.

3. Ishii, R.; Okazaki, S.; Okada, I.; Furusaka, M.; Watanabe, N.; Misawa, M.; Fukunaga, T., A neutron-scattering study of the structure of supercritical carbon-dioxide. *Chem. Phys. Lett.* **1995,** 240, (1-3), 84-88.

4. Yamaguchi, T.; Benmore, C. J.; Soper, A. K., The structure of subcritical and supercritical methanol by neutron diffraction, empirical potential structure refinement, and spherical harmonic analysis. *J. Chem. Phys.* **2000,** 112, (20), 8976-8987.

5. Benmore, C. J.; Tomberli, B. L., The structure of carbon dioxide around naphthalene investigated using H/D substitution in neutron diffraction. *Ind. Eng. Chem. Res.* **2000,** 39, (12), 4491-4495.

6. Peterson, P. F.; Gutmann, M.; T., P.; S.J.L., a. S. J. L. B., PDFgetN: A user-friendly program to extract the total scattering structure function and the pair distribution function from neutron powder diffraction data. *J. Appl. Crystallogr.* **2000,** 33, 1192-.

APPENDIX H: MOLECULAR DYNAMICS SIMULATIONS IN DEEP EUTECTIC SOLVENTS

Introduction

Deep eutectic solvents (DES) are formed when two high-melting point solids are heated to give a liquid mixture with a substantially lowered melting point. Fructose and urea (Figure H.1) independently melt at 103°C and 133°C respectively, but form a eutectic at 65°C when combined in a 60wt% fructose mixture.[1] DES can be beneficial as a reactant medium if either or both components are a reactant because solvent waste and downstream separations are eliminated; therefore, minimizing the environmental and economic impact of the system.

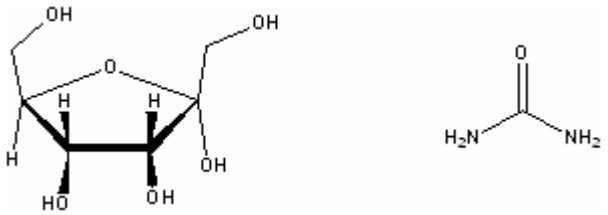

Figure H.1: Structure of fructose (left) and urea (right).

Computational Methods

The urea force field was OPLS-based with bond stretching and angle bending capabilities. All parameters were taken from Duffy et al.[2] The inner ring of fructose was kept rigid, but hydroxyl and methyl groups were allowed to stretch and bend. Fructose parameters were an all-atom, OPLS-based force field specifically designed for carbohydrates.[3] The initial system was set-up as a three-by-three unit cell of fructose

surrounding a two-by-two unit cell of urea. Fructose molecules that overlapped the urea crystal were removed by an external FORTRAN code. Unit cell files for fructose[4] and urea[5] were taken from the literature in a *.cif* format for crystalline structures and imported into the program Mercury version 1.4.2. Larger crystals (i.e. 3 by 3 unit cells) were constructed in Mercury and the resulting coordinates were saved in *.xyz* format and altered to match the DL_POLY input format.

The concentric crystals were initially run under NVT conditions at 200°C for 500ps to break apart the crystals and obtain a well-mixed liquid. The time step was 1fs with a relaxation time constant of 1ps, and the box dimensions were equal to the dimensions of the fructose crystal. Upon completion the final configuration was input into GopenMol, a free graphics package to visualize MD simulation trajectories, to ensure that the crystal had melted and the liquid was homogeneously distributed. A shorter 50ps, 200°C simulation was run and trajectories were saved every 10ps as input for a 75°C NVT simulation to obtain structural statistics. This temperature was higher than the melting point to ensure that temperature fluctuations exceeded the melting point. Configurations were sampled every 10fs over the course of a 200ps simulation to form RDFs. Separate NVE simulations were run from these trajectories to investigate dynamic aspects of DES.

Results

Radial Distribution Functions

RDFs show significant hydrogen bonding between the hydroxyl hydrogen atoms on fructose and the carbonyl oxygen on urea. A RDF function for this system is shown in

Figure H.2. Other hydrogen bonds, such as urea-nitrogen to hydroxyl hydrogen, could contribute to the deep eutectic, but the RDF for these two atoms (Figure H.3) shows that this interaction is not as significant as the other interaction.

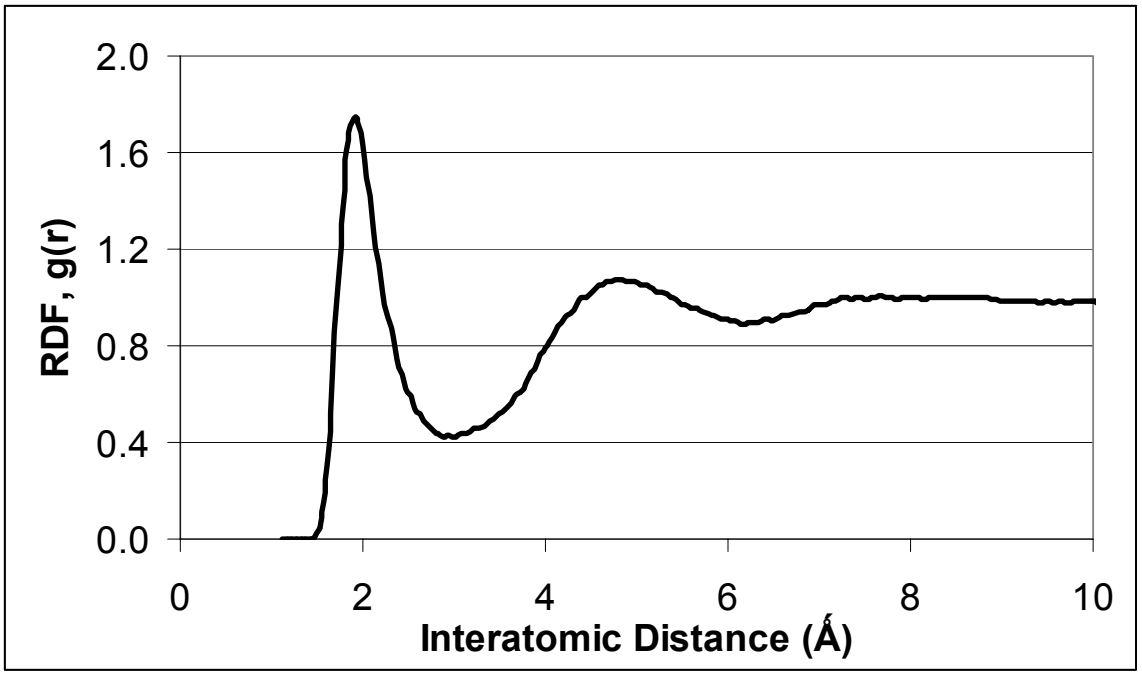

Figure H.2: RDF between carbonyl oxygen on urea and hydroxyl hydrogen on fructose.

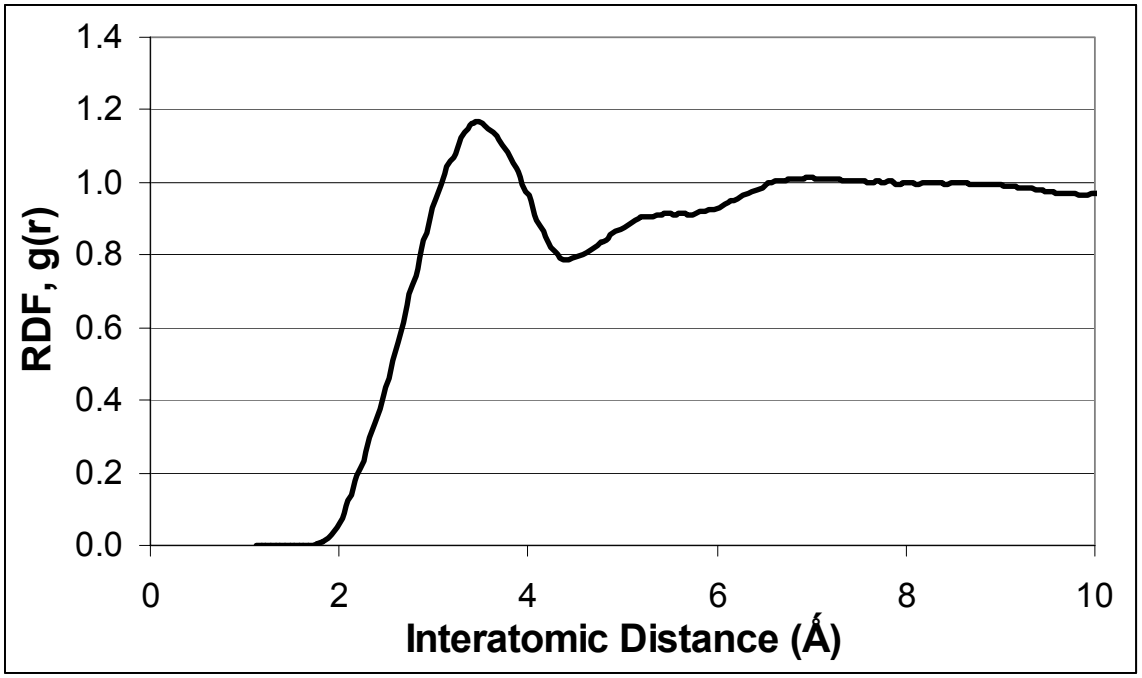

Figure H.3: RDF between a urea nitrogen and fructose hydroxyl hydrogen.

Solvent Dynamics

DES are quite viscous and could encounter mass transfer limitations or difficult processing. Consequently micro-fluidic dynamics could provide insight into these limitations. Dynamics were explored with local density autocorrelation functions (LDAF) which indicate timescales of solvent interactions, in this case the interaction time between urea's carbonyl oxygen and fructose's hydroxyl hydrogen. The functional form of the LDAF is given in Equation H.1:

$$LDAF(t) = \frac{\langle \delta\rho(0)\delta\rho(t) \rangle}{\langle \delta\rho(0)^2 \rangle}$$ Equation H.1

where ρ(t) is the local number density within at time t, and $\delta\rho$(t) = ρ(t) - $\bar{\rho}$. The $\bar{\rho}$ term is the average local number density. Equation H.1 can be discretized to a less rigorous and tractable expression given by Equation H.2:

$$LDAF(t) = \frac{\sum_{i=1}^{N}\left[N_i(R_{cut},t) - \overline{N}_i(R_{cut})\right]\left[N_i(R_{cut},0) - \overline{N}_i(R_{cut})\right]}{\sum_{i=1}^{N}\left[\left[N_i(R_{cut},0) - \overline{N}_i(R_{cut})\right]\left[N_i(R_{cut},0) - \overline{N}_i(R_{cut})\right]\right]} \qquad \text{Equation H.2}$$

where N_i(t) is the number of neighbor atoms within a cutoff radius (R_{cut}) at time, *t*, and $\overline{N}$ is the time-averaged number of atoms within the cutoff radius. The cutoff radius was determined from Figure H.2 and is the distance to the first well of the RDF or 3Å in this case.

The LDAF for 65% fructose + urea DES is shown in Figure H.4. There are several interesting features in this LDAF. There is a very fast initial decay that lasts 0.5ps and accounts for nearly 45% of the overall decay. This is followed by two slower timescales, one that lasts 25ps and another very long timescale that lasts over 300ps. These two timescales account for 35% and 20% respectively of the remaining decay. Not surprisingly the dynamics are very slow because of the high viscosity and strong intermolecular forces between the two components. The slow dynamics are a concern and a third component would need to be added to increase transport in the DES and possibly lower the melting point.

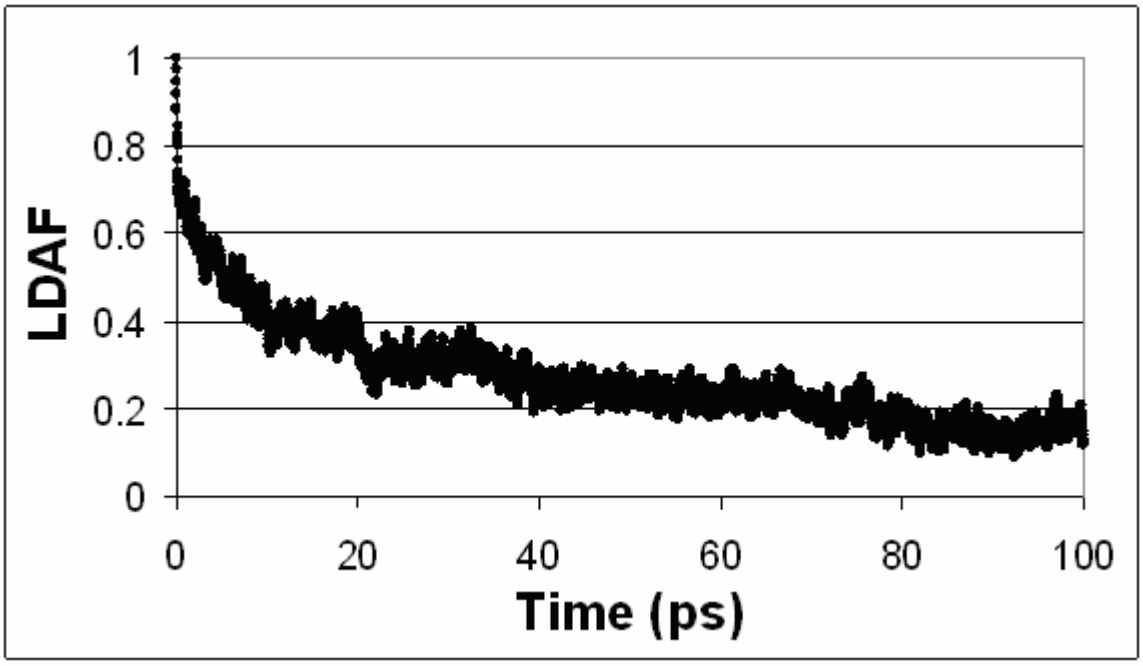

Figure H.4: LDAF for a 65% fructose + urea DES at 75°C.

Conclusion

These MD simulations provide insight to the intermolecular interactions that cause the melting-point depression. Hydrogen bonding between urea's carbonyl oxygen and the protic hydrogen atoms on fructose enables solvation and decreases the melting point. Surprisingly interactions between the nitrogen atoms and the protic hydrogen atoms are insignificant compared to the carbonyl-hydrogen interaction. The RDFs indicate an inter-atomic distance of 3.8Å which could be a secondary effect from the carbonyl hydrogen bond. Dynamics indicate that the hydrogen bond is favorable and remains locked in place for long timescales. This has implications on bulk transport properties and viscosity. This preliminary study highlights interesting intermolecular behavior and provides information that could be used to design solvent systems; however, DES have limited advantages over traditional solvents. Their applicability is an

open-ended problem that could be revived if the unique features of the solvent prove beneficial to a chemical process. For this reason, the computational work was halted, but could be resumed by future researchers if DES become an attractive processing medium.

References

1. Imperato, G.; Eibler, E.; Niedermaier, J.; Konig, B., Low-melting sugar-urea-salt mixtures as solvents for Diels-Alder reactions. *Chem. Comm.* **2005**, (9), 1170-1172.

2. Duffy, E. M.; Kowalczyk, P. J.; Jorgensen, W. L., Do denaturants interact with aromatic-hydrocarbons in water? *J. Am. Chem. Soc.* **1993,** 115, (20), 9271-9275.

3. Damm, W.; Frontera, A.; TiradoRives, J.; Jorgensen, W. L., OPLS all-atom force field for carbohydrates. *J. Comp. Chem.* **1997,** 18, (16), 1955-1970.

4. Kanters, J. A.; Roelofsen, G.; Alblas, B. P.; Meinders, I., Crystal and molecular-structure of beta-d-fructose, with emphasis on anomeric effect and hydrogen-bond interactions. *Acta Crystal. B* **1977,** 33, (MAR15), 665-672.

5. Swaminathan, S.; Craven, B. M.; McMullan, R. K., The crystal-structure and molecular thermal motion of urea at 12K, 60K and 123K from neutron-diffraction. *Acta Crystal. B* **1984,** 40, (JUN), 300-306.

VITA

John Linton Gohres III was born on October 29, 1981 to John and Mary Gohres in Metairie, LA. The eldest of three children, he attended Jesuit High School in New Orleans during which time he met his future wife Amy Margaret Attardo. After graduating from Jesuit in 1999, John attended Louisiana State University in Baton Rouge, Louisiana where he graduated in 2004 with a B.S. in Chemical Engineering. John enrolled at the Georgia Institute of Technology in the fall of 2004 to pursue a Ph. D. in Chemical Engineering. While attending Georgia Tech, John married Amy in the fall of 2006 and researched under the direction of Dr. Charles Eckert of Chemical and Biomolecular Engineering, Dr. Charles Liotta of Chemistry and Biochemistry, and Dr. Rigoberto Hernandez of Chemistry and Biochemistry. John will complete his Ph.D. in August of 2008.